TESI DI DOTTORATO DI RICERCA
IN
SCIENZA E INGEGNERIA DEI MATERIALI

Università degli Studi di Padova

Dipartimento di Scienze Chimiche

SCUOLA DI DOTTORATO DI RICERCA IN SCIENZA E INGEGNERIA DEI MATERIALI
INDIRIZZO COMUNE
CICLO XXVII

Au-Co Thin Films and Nanostructures for MagnetoPlasmonics

Direttore della Scuola: Ch.mo Prof. Gaetano GRANOZZI
Supervisore: Ch.mo Prof. Giovanni MATTEI

Dottoranda: Valentina MATTARELLO

Alla mia famiglia:
Riccardo, Samuele e Sara Maria

e alla famiglia
che mi ha cresciuta

Abstract

This thesis develops in the framework of the Material Science for MagnetoPlasmonic purposes. MagnetoPlasmonics is a recent and fast growing research field that aims at coupling the plasmonic properties typical of nanostructured noble metals (as, for instance, the local enhancement of electromagnetic field or the extraordinary optical transmission) with magnetic functionalities.

Promising applications, just to mention a few, span from sensing to the realization of active optical circuits at a nanoscale level.

MagnetoPlasmonic systems, so far mostly studied in the literature, are based on thin layers or nanostructures of noble metals coupled with ferromagnetic materials. Nevertheless, the requirement to increase the performances of such systems, and/or extend their functionalities, prompts the search for innovative compounds, which, displaying synergistic properties not otherwise achievable in phase segregated mixtures, can hold both plasmonic and magnetic features.

The aim of the present thesis is the realization and study of Au:Co alloyed thin films and nanostructures: gold is among the best performing materials in Plasmonics, while cobalt is known for its ferromagnetic properties. Unfortunately, the two metals are immiscible as bulk phases.

Au:Co thin films have been prepared by magnetron sputtering deposition technique in co-focusing geometry. Three different compositions have been investigated, i.e., Au2Co1, Au1Co1 and Au1Co2, combined with three different values of thickness, i.e., $\approx$ 15 nm, $\approx$ 30 nm and $\approx$ 100 nm.

A full structural investigation has been carried out by X-Ray Diffraction integrated with X-Ray Absorption Spectroscopy and Transmission Electron Microscopy. The results demonstrate that the major fraction of the film is composed of an Au:Co alloy, typically richer in gold with respect to the nominal Au:Co atomic ratios.

The alloy fraction, its stoichiometry and the local order depend on the initial Au:Co ratio. In the case of Au2Co1 sample, the alloy is, indeed, amorphous, while in the case of alloy richer in cobalt, there are some FCC crystalline seeds, elongated along the direction of the film growth. These grains are highly textured, with the (111) planes parallel to the substrate, and show a lattice constant that shortens as the Co content increases.

Besides this alloyed phase, there are segregated clusters of Cobalt, extremely nanostructured.

The presence of two magnetic phases is confirmed by SQUID measurements, which, furthermore, allowed to characterize the hysteresis loops of the Au:Co films and to estimate the values of saturation magnetization.

The optical properties of the films have been characterized by transmittance UV-Vis measurements and Ellipsometry.

A thermal stability study demonstrated that the alloy is stable up to 200° C; then, as the temperature increases, a de-alloying process occurs leading to two segregated phases of

gold and cobalt.

The as-prepared Au-Co materials have been employed as metallic component in nanostructured periodic arrays, i.e., Semi Nano-Shell Array and Nano Hole Array. The morphological as well as the optical characterizations of the arrays demonstrate that these systems are promising candidates for future magneto-plasmonic studies and applications.

Estratto

Il presente lavoro si inserisce nell'ambito della scienza e ingegneria dei materiali per la MagnetoPlasmonica. Questa ultima è una recente, ma allo stesso tempo crescente, area di ricerca che mira a combinare le proprietà plasmoniche tipiche dei metalli nobili nanostrutturati (quali, ad esempio, l'intensificazione del campo elettromagnetico locale o la trasmissione ottica straordinaria) con funzionalità di tipo magnetico.

Promettenti applicazioni spaziano dalla sensoristica alla realizzazione di nanocircuiti totalmente ottici, solo per citarne alcuni.

Tradizionalmente i sistemi per MagnetoPlasmonica più considerati in letteratura prevedono l'accoppiamento di un film sottile o arrangiamento nanostrutturato di metalli nobili con materiale ferromagnetico. Tuttavia, al fine di migliorare le prestazioni di suddetti sistemi e/o esplorare nuove funzionalità è necessario ricercare nuovi composti in cui già il materiale innovativo presenta proprietà plasmoniche e magnetiche.

Scopo della presente tesi è la realizzazione e lo studio di film sottili e nanostrutture a base di lega Au-Co: l'oro è, infatti, un metallo nobile tra i migliori per applicazioni in plasmonica e il cobalto è un materiale ferromagnetico. I due metalli allo stato *bulk* sono notoriamente immiscibili.

Con la tecnica di deposizione magnetron sputtering sono stati depositati (in geometria di codeposizione) film sottili Au:Co, caratterizzati da tre diverse composizioni, ovvero Au2Co1, Au1Co1 e Au1Co2 e tre diversi spessori, rispettivamente $\approx$ 15 nm, $\approx$ 30 nm e $\approx$ 100 nm.

Una ricerca estesa è stata condotta con l'obiettivo di studiare attentamente le proprietà strutturali dei film, combinando diffrazione a raggi X, con misure di Assorbimento X svolte al Sincrotrone e Microscopia elettronica. I risultati dimostrano che la parte predominante del film è costituita da una lega Au-Co che è tipicamente più ricca in oro rispetto ai rapporti atomici nominali di Au e Co.

La frazione di lega, la sua stechiometria e l'ordine locale dipendono dal rapporto Au/Co inizialmente presente. Inoltre, mentre nel campione Au2Co1 la lega è prevalentemente amorfa, nel caso delle leghe più ricche in cobalto vi è la presenza di grani FCC cristallini, allungati lungo la direzione di crescita del film, fortemente tessiturati (in cui i piani (111) sono prevalentemente paralleli al substrato) e caratterizzati da un parametro reticolare che diminuisce all'aumentare del contenuto di cobalto.

Oltre alla fase di lega, sono presenti dei clusters di cobalto, caratterizzati da un basso ordine strutturale.

L'interfaccia tra due fasi magnetiche è stata confermata da misure SQUID che hanno inoltre permesso di caratterizzare i cicli di isteresi dei film Au:Co e di stimarne i valori di magnetizzazione di saturazione.

Le proprietà ottiche dei film sono state caratterizzate con misure di trasmittanza (nel range UV-Vis) ed Ellissometria.

Da un punto di vista termico, la lega Au-Co si dimostra stabile fino a 200° C; al crescere

della temperatura ha lungo una de-alligazione che porta alla formazione di fasi metalliche separate di oro e cobalto.

I materiali Au-Co così preparati e caratterizzati sono stati poi impiegati come componente metallica in *array* periodici nanostrutturati, i.e., *Semi Nano-Shell Array* e *Nano Hole Array*. Gli array sono stati caratterizzati da un punto di vista morfologico e ottico dimostrandosi promettenti piattaforme per future caratterizzazioni MagnetoPlasmoniche.

Contents

List of Acronyms

SPs   Surface Plasmons

LSPs   Localized Surface Plasmons

ESPs   Extended Surface Plasmons

SPPs   Surface Plasmon Polaritons

LSPR   Localized Surface Plasmon Resonance

MO   Magneto-Optical

TM   Transverse-Magnetic

TE   Transverse-Electric

XRD   X-Ray Diffraction

RBS   Rutherford Backscattering Spectrometry

XRD   X-Ray Diffraction

GI-XRD   Grazing Incidence X-Ray Diffraction geometry

FCC   Face Centered Cubic

HCP   Hexagonal Close Packing

FWHM   Full Width Half Maximum

TEM   Transmission Electron Microscopy

BF-TEM   Bright-Field Transmission Electron Microscopy

HR-TEM   High-Resolution Transmission Electron Microscopy

STEM   Scanning Transmission Electron Microscopy

HAADF-STEM   High-Angle Annular Dark-Field and Scanning-TEM

SAED   Selected-Area Electron Diffraction

FFT	Fast Fourier Transform
EXAFS	Extended X ray Absorption Fine Structure
DW	Debye-Waller
XMCD	X-ray Magnetic Circular Dichroism
SQUID	Superconducting Quantum Interference Device
M_S	Saturation Magnetization
M	Magnetization
H_c	Coercitivity
M_r	Remanent Magnetization
ZFC	Zero-Field-Cooling
FC	Field-Cooling
SEM	Scanning Electron Microscopy
EDS	Energy Dispersive Spectroscopy
SNSA	Semi-NanoShell Array
NHA	Nano Hole Array
NSL	Nanosphere Lithography
SAM	Self Assembled Monolayer
PS	Polystyrene
SLG	Soda Lime Glass
AFM	Atomic Force Microscopy
SEM	Scanning Electron Microscopy
FE-SEM	Field Emission Scanning Electron Microscopy
RIE	Reactive Ion Etching
EOT	Extraordinary Optical Transmission

List of Figures

List of Tables

Introduction

Nowadays, an unavoidable driving force for technology advancement is the search for innovative nanomaterials in which new functionalities, linked to the small dimensions of the system, can lead to new properties and applications unattainable with bulk materials. This is particularly true in the optical field, where nano-optics is a well-established and fast growing research area. A subfield of nano-optics is *Plasmonics*, which aims at understanding and controlling light within sub-wavelength volumes using the surface plasmons sustained by metallic nanostructures [1]. The surface plasmons are essentially electromagnetic waves coupled to the collective oscillations of the surface free electrons at an interface between two media with permittivites of opposite sign (typically a dielectric and a metal) and are able to confine the light beyond the diffraction limit. The resulting properties, e.g., the local field enhancement, the extraordinary transmission through nano-holed films and the high sensitivity to the dielectric environment embedding the nanostructures, are of paramount importance to develop new or improved devices for sensing and information transmission technology [10].

Unfortunately, these peculiar features are inevitability accompanied by optical losses and the inability to modulate the optical signal using noble metals alone. New strategies are, indeed, required to counteract these drawbacks and to push Plasmonics into technological applications [11]. A promising approach is to exploit the various forces playing at the nanoscale and, among them, the magneto-optical effects allows a dynamic control over light with sub-wavelength resolution. The coupling of the field of Plasmonics with that of *Magnetism* has lead to the so-called *Magneto-Plasmonics*, a quite recent research area which has been gathering increasing attention among scientific groups spanning from nano-optics and nano-electronics to biosensing. Here the plasmonic features can be, on one hand, tuned upon the application of a magnetic field while, on the other hand, the Magneto Optical activity can be largely enhanced by plasmonic resonance excitations [2]. In this framework, the search for systems, interactions and, among all, materials that may complement the

strength of plasmonics, prompted for the development of materials exhibiting both plasmonic and magnetic functionalities, with low losses and, at the same time, realistically transferable to the production phase.

As noble metals are the best performing materials in Plasmonics, major efforts have so far being dedicated to magnetoplasmonic systems where a thin layer or nanostructured noble metal was combined with a thin ferromagnetic material. A step forward in the materials' optimization would be the search for bimetallic compounds, which can support both the functionalities. Accessing alloying composites is important because such phases offer interesting synergistic properties not otherwise achievable in phase segregated mixtures. Bimetallic compounds have attracted considerable attention because they show multiple functionalities and excellent properties among which catalytic, magnetic and photonic features [12]. Nevertheless, a comprehensive investigation on their synthesis feasibility and characterization is urgent but still lacking.

This thesis develops in the framework of Material Science and Engineering for Magneto-Plasmonic purposes. The aim of this work is the realization and study of Au:Co bimetallic nanostructured systems, where the strong plasmonic properties of Gold are intermixed with the Co ferromagnetic ones. Gold is, indeed a noble metal among the best performing materials in Plasmonics [13] and, moreover, is characterized by chemical stability and resistance to oxidation; Cobalt is well known and employed for its magnetic features [14]. The alloying of the two components (immiscible in the bulk phase) is analyzed both in thin film as well as in 3D periodic nanostructures supporting localized and/or extended plasmonic modes.

To investigate the 'alloying' behavior of Au and Co at a nanoscale level three sets of coatings have been deposited through a magnetron sputtering technique in co-deposition geometry. Each set consists of an Au:Co 'balanced film' i.e., with an almost equal content of Au and Co, an Au-Rich film and a Co-rich film, while the sets distinguished only for their thickness, being prepared in similar process conditions (value of thickness respectively $\approx$15 nm, $\approx$30 nm and $\approx$100 nm). Firstly, a full structural investigation is carried out through X-Ray Diffraction techniques coupled to X-Ray Absorption measurements and to Transmission Electron Microscopy imaging. The optical properties of the alloyed thin films have been characterized by Ellipsometric and UV-Vis measurements. The magnetic behavior was studied by means of SQUID measurements; furthermore the magnetic moment acquired by gold in the alloy was estimated by XMCD experiment.

Then, the nano-structuring of Au:Co nanocomposites into the three dimensions is achieved by means of deposition technique combined with a self-assembly process (through Nano Sphere Lithography). Arrays of Semi Nano Shells (SNSA) and of Nano Hole Arrays (NHA) have been prepared still containing the alloyed Au:Co compounds. The morphological as well as the optical characterizations demonstrate that these systems are promising candidates for future magneto-plasmonic studies and applications.

In particular, the thesis is organized as follows:

Chapter 1 will summarize some basic concepts of Plasmonics (see section 1.2.1) as well as Magneto-Plasmonics (see section 1.2.2), with a summary of the main applications 1.2.3. Furthermore a review of the literature works dedicated to Au-Co system is presented, with particular emphasis on the structural features (section 1.3).

Chapter 2 will describe the deposition technique adopted to prepare the thin films and their compositional characteristics (see 2.2). Great attention will be paid to the full structural investigation, both in the 'long range' by X-Ray Diffraction (section 2.3.1), as well as in the 'short range' by X-Ray Absorption technique (section 2.3.3).

Chapter 3 will deal with the optical characterization of the films (through Ellipsometry and Uv-Vis spectroscopy, see section 3.1) and their magnetic features (see 3.2). Then, results about the thermal stability of the Au-Co alloy and the evolution of the coatings, as a function of the temperature, will be presented (section 3.3).

Chapter 4 will describe the periodic nanostructured systems, Nano Hole Array (NHA, see 4.4) as well as Semi-NanoShell Array (SNSA, see 4.3) in terms of synthesis procedures, morphological characterization and optical properties.

1 The background

This Chapter describes some basic concepts of MagnetoPlasmonics and a review on the Au:Co systems investigated in the literature with a particular focus on the structural results.

1.1 Motivations

The emerging and fast growing field of *MagnetoPlasmonics* aims at coupling the features of *Plasmonics* with the *Magneto-Optical* properties to develop, for instance, innovative devices in the sensing area and nanophotonics.

This prompts to find novel materials, which combine both functionalities, with low losses and which, possibly, are easily processable.

The two candidate materials for mixing are gold, which is among the best performing plasmonic metals and moreover, shows good chemical stability, and cobalt, known for its ferromagnetic properties. As these metals are immiscible in bulk phases, a strategy is needed to force the alloying behavior at the nanoscale and great attention should be devoted to the structural characterization of the prepared compound, in order to describe the alloy. These features need, then, to be linked to the functional properties of the material, in particular to the optical and magnetic characteristics.

The search for *innovative materials* is, indeed, a forefront sub-field of *MagnetoPlasmonics*, and it is the area from which this thesis originates.

1.2 A short Introduction to MagnetoPlasmonics

In the following sections the key ideas at the bottom of *MagnetoPlasmonic* field will be presented.

The aim is not to give a comprehensive view of the physics and technology developed in

the framework of *Plasmonics* neither a detailed description of Magneto-Optical features but just to introduce some basic concepts, definitions and equations useful for further discussions. For a detailed description the reader can refer to [1] and [2] and references therein.

1.2.1 Plasmonics

Plasmonics, a sub-field of *Nano-Photonics*, aims at studying and manipulating the high local field amplification which occurs on a scale length much smaller than the wavelength, when an electromagnetic field interacts with nanostructured metals. This field enhancements takes place through the Surface Plasmons (SPs) which are essentially electromagnetic waves coupled to the collective oscillations of the surface free electrons in an interface between typically a dielectric and a metal.

Surface plasmon modes are strongly localized at the interface between these two media and can be supported by a huge variety of metallic structures, spanning from bi-dimensional single surface, thin films, nanoparticles, three-dimensional nanostructures and so on. They can be classified into two main categories: Localized Surface Plasmons (LSPs) which arise from the interaction of the electromagnetic radiation with nanostructures where the characteristic length is in the order of or smaller than the incident field wavelength in the Vis-NIR range, and Extended Surface Plasmons (ESPs) (also known as Surface Plasmon Polaritons (SPPs)) supported by planar interfaces.

A key concept in the explanation of SPs modes is the description of the optical properties of metals over a wide frequency (ω) range in term of the dielectric function $\varepsilon(\omega)$. These dispersive properties are responsible for the different behavior that characterizes metal materials in the wavelength (λ) range from UV to infrared. Within the simple Drude model, for low frequencies (λ up to visible range) the electromagnetic field is strongly reflected and there is no propagation inside the metals. For higher frequencies (Near UV-visible) the penetration of the radiation and, as a consequence, the dissipation increases. In the UV range metals show a dielectric behavior and the radiation propagates into them. The electronic band structure of different metals is responsible for the dielectric behavior leading to different properties; as an example alkali metals show an ultraviolet transparency while noble metals show a high absorption of radiation in UV frequencies. This absorption, which characterizes for example gold and silver, is due to transitions between electronic

bands.

Starting with the Maxwell's equation of macroscopic electromagnetism and limiting to a linear, isotropic and nonmagnetic media, the constitutive relations can be defined:

$$\mathbf{D} = \varepsilon\varepsilon_0\mathbf{E} \tag{1.1a}$$

$$\mathbf{B} = \mu\mu_0\mathbf{H} \tag{1.1b}$$

$$\mathbf{J} = \sigma\mathbf{E} \tag{1.1c}$$

where, $\mathbf{D}$ is the dielectric displacement, $\mathbf{B}$ is the magnetic induction, $\mathbf{H}$ the magnetic field, $\mathbf{E}$ is the electric field, $\mathbf{J}$ is the internal current density; ε is the relative dielectric function, σ is the conductivity and μ is the relative permeability (ε_0 is the electric permittivity in vacuum, $\varepsilon_0 \approx 8.854 \times 10^{-12}$ F/m, while μ_0 is the magnetic permeability in vacuum, $\mu_0 \approx 1.257 \times 10^{-6}$ H/m; $\mu = 1$ for non magnetic media);

It is clear that the electromagnetic phenomena taking place in metals can be described using either ε or σ, being these quantities closely related through equations 1.1.

As phenomenologically described before, the optical response of metals clearly depends on frequency so that the non-locality in time and space should be taken into account. Decomposing the impinging fields into individual plane-wave components of wave vector $\mathbf{K}$ and angular frequency ω, the constitutive relations 1.1a, 1.1b, 1.1c can be expressed in the Fourier domain. Then, recognizing that $\partial/\partial t \longrightarrow -i\omega$, the fundamental relation between the *dielectric function* and the *conductivity* becomes:

$$\varepsilon(\mathbf{K},\omega) = 1 + \frac{i\sigma(\mathbf{K},\omega)}{\varepsilon_0\omega}. \tag{1.2}$$

$\varepsilon(\mathbf{K},\omega)$ can be simplified into $\varepsilon(\mathbf{K}{=}0,\omega)$, i.e., $\varepsilon(\omega)$ in the approximation of spatially local response. This is correct when λ in the medium is higher with respect to the size of unit cell or the electrons mean free path as typically occurs in the Vis-NIR region. The main property which describes how a material interacts with an electromagnetic field is the dielectric function $\varepsilon(\omega)$, usually defined as:

$$\varepsilon(\omega) = \varepsilon_1(\omega) + i\varepsilon_2(\omega) \tag{1.3}$$

The dielectric function is related to complex refractive index $\tilde{n}$, where $\tilde{n} = n + ik$ by the following equations:

$$\tilde{n} = \sqrt{\varepsilon} \tag{1.4}$$

$$\varepsilon_1 = n^2 - k^2 \tag{1.5}$$

$$\varepsilon_2 = 2nk \tag{1.6}$$

$$n^2 = \frac{\varepsilon_1}{2} + \frac{1}{2}\sqrt{(\varepsilon_1)^2 + (\varepsilon_2)^2} \tag{1.7}$$

$$k = \frac{\varepsilon_2}{2n} \tag{1.8}$$

where k is the extinction coefficient which describes the absorption of the incident field by the medium and is related to the absorption coefficient α through the Beer's Law. The imaginary part of ε (ε_2) determines the amount of absorption inside the medium.

The dielectric function for a metal can be derived in the framework of the Drude model [15] as in a wide range of frequencies the optical properties of metallic material can be described through the *plasma model*. In this model, a gas of free electrons of number density n moves against a fixed background of positive ion cores, in the presence of an oscillating electromagnetic field. While the electron-ion collisions are assumed to occur at frequency $\gamma = 1/\tau$ (where τ is the relaxation time, $\approx 10^{-13}$-10^{-14} s at room T), the electron-electron interactions are neglected: the features of the band structure are incorporated into an effective optical mass m of each electron. Given these assumptions, the motion of an electron of the plasma sea can be described with a damped harmonic oscillator model. If we assume a harmonic time dependance of the driving field **E**, the expressions for the *dielectric function* ε for the free electron gas and its real and imaginary parts become:

$$\varepsilon(\omega) = 1 - \frac{(\omega_p)^2}{\omega^2 + i\gamma\omega} \tag{1.9}$$

$$\varepsilon_1(\omega) = 1 - \frac{(\omega_p)^2\tau^2}{1 + \omega^2\tau^2} \tag{1.10}$$

$$\varepsilon_2(\omega) = \frac{(\omega_p)^2\tau}{\omega(1 + \omega^2\tau^2)} \tag{1.11}$$

where ω_p is the so called *plasma frequency* of free electron gas, $(\omega_p)^2 = ne^2/\varepsilon_0 m$. In the high frequency limit ($\omega \gg \gamma$) the dielectric function is essentially real ($\varepsilon(\omega) = 1 - \omega_p^2/\omega^2$). It is worth noting that the behavior of noble metal in this frequency region is completely

altered by inter-band transitions due to the excitation of electrons from the filled band. This phenomenon leads to an increase of the imaginary part of the dielectric function and occurs also in the case of gold for which a correction to the Drude model is needed [16]. For $\omega \ll \tau^{-1}$, i.e., in the regime of low frequencies, $|\varepsilon_2|$ exceeds $|\varepsilon_1|$ and metals are mainly absorbing. The application of Beer's law of absorption implies that, for this 'low frequencies regime', the fields fall off inside the metal as $e^{-\frac{z}{\delta}}$, δ being the so called *skin depth,* whose value is tens of nanometers for a typical metal.

The *plasma frequency,* ω_p, which correspond to the lower frequency limit of propagation of transverse electromagnetic waves, can be recognized as the natural frequency of a free oscillation of the electron gas: the quanta of these charge oscillations are called *volume plasmons,* to be distinguished from the *surface* and *localized* plasmons described below.

Let's consider now a flat interface between a conductor and a dielectric (see Fig. 1.1-a) for the axis definition). The application of the Maxwell's equations to this planar
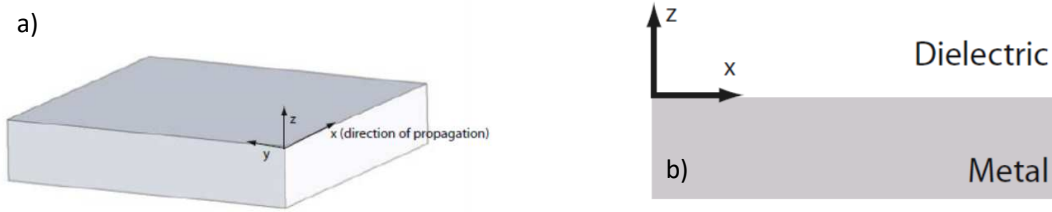
Figure 1.1: a) The geometry for the description of the planar waveguide: the waves propagate along the x-direction in a Cartesian coordinate system. b) Geometry for Surface Plasmon propagating at a single interface between a metal and a dielectric.

waveguide geometry, with the assumption that the dielectric function is constant on a optical wavelength scale and that the electric field has an harmonic time dependance, leads to the *Helmholtz equation*

$$\nabla^2 \mathbf{E} + k_0^2 \varepsilon \mathbf{E} = 0, \tag{1.12}$$

where $\mathrm{k}_0 = \omega/\mathrm{c}$ is the wave vector of the propagating wave in vacuum.

This equation has to be solved separately in region of constant ε and the obtained solutions have to been matched with the appropriate boundary conditions. Considering now the one-dimensional problem, -see 1.1-b)- with the assumptions:

- there is a planar interface between two media, a metal (ε_1) and an insulator (ε_2);
- the insulator is a non-absorbing medium with Re[ε_2]> 0;
- the metallic character of the other media is described by Re[$\varepsilon_1(\omega)$]< 0 (condition fulfilled

for ω below ω_p);

- z direction defines the perpendicular direction to the interface;
- x,y are the coordinates of the interface plane;
- the direction of the traveling wave is x;
- ε changes only in the z direction ($\varepsilon = \varepsilon(z)$).

we want to look for propagating wave solutions confined to the interface, i.e., with evanescent decay in the perpendicular *z-direction*, taking into account the continuity of the electric and magnetic field at the interface. Describing the electric field of the traveling wave in x direction as $\mathbf{E}(x, y, z) = \mathbf{E}(z) e^{i\beta x}$, where β is the so called *propagation constant* of the waves and corresponds to the component of the wave vector in the propagation direction x ($\beta = k_x$), the solution of the equation 1.12, leads to:

$$\beta = k_0 \sqrt{\frac{\varepsilon_1 \varepsilon_2}{\varepsilon_1 + \varepsilon_2}} \tag{1.13}$$

The 1.13 is the dispersion relations of the ESPs propagating at the interface between the two half spaces. The confinement of the wave is quantified in terms of the evanescent decay length of the field perpendicular to the interface defined as:

$$\hat{z} = 1/|k_z| \tag{1.14}$$

being k_z the component of the wave vector perpendicular to the interface.

It is worth noting that the radiation confinement to the interface requires $\mathrm{Re}[\varepsilon_1] < 0$ if $\mathrm{Re}[\varepsilon_2] > 0$: the surface waves exist only at interface between materials with opposite sign of the real part of their permittivities, e.g., between a conductor and an insulator. The 1.13 is also valid for conducting media with complex dielectric function, so that also the ESPs propagation lenght β is complex.

The travelling ESPs are damped with an energy attenuation length (also called *propagation length*) $L = (2Im[\beta])^{-1}$, typically between 10 and 100 μm in the visible range. Moreover, there is a characteristic trade-off between localization and loss, typical for Plasmonics, for which a better confinement corresponds to a lower propagation length.

As it can be seen in Fig. 1.2-a), the ESPs dispersion curve lies to the right of the light line in air: a direct excitation is hindered while alternative phase-matching conditions are required to excite ESPs. This condition can be achieved by means of charged particle impact, prism

coupling, grating coupling, highly focused optical beams or near-field excitation.

An example of phase-matching through prisma coupling is reported in Fig. 1.2-b); here a thin metal film is sandwiched between two insulator of different dielectric constant, the insulator of higher ε being in form of a prism: ESPs with propagation constant β between the light lines of air and the higher-index dielectric can be excited. The occurrence of a ESPs excitation affect the far field properties of the system, as, for example, a sharp dip in the reflection spectrum.
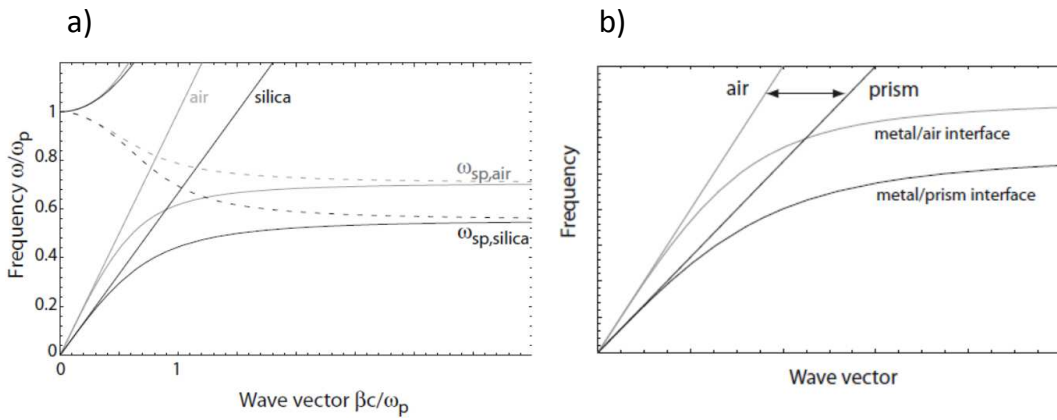
Figure 1.2: a) Dispersion relations of ESPs of a Drude metal/air or silica interface. b) Dispersion relations of ESPs adopting the prism coupling. [1]

The matching condition can be fulfilled also by means of periodic structures -with period a-, which provide the extra-momentum needed to satisfy both energy and momentum conservation with the relation:

$$\beta = ksin\theta \pm \Delta k_x \tag{1.15}$$

$$\beta = ksin\theta \pm \nu 2\pi/a \tag{1.16}$$

where $ksin\theta$ is the momentum k_x of photons impinging under an angle θ with respect to the surface normal, ν is an integer ($\pm 1, \pm 2, \pm 3...$) and $2\pi/a$ is the reciprocal vector of the periodic structure. Examples of these periodic structures are the 1D or 2D gratings like Nano Hole Arrays (NHA), i.e., periodic array of holes in an opaque metal film which will be discussed in section 4.4.

Summarizing, ESPs are electromagnetic excitations propagating at the interface between a dielectric and a conductor, evanescently confined in the perpendicular direction, and originating when the impinging electromagnetic field couples to the conductor's electron

plasma. Beside these extended plasmons, LSPs can be excited at the interface between a sub-wavelength metal particle and a dielectric medium, when interacting with an incident electromagnetic field.

The archetypic example used in the explanation of this phenomenon is a metallic spherical nanoparticle embedded in a dielectric medium. The incident field causes an oscillation of the free electrons while the curved surface of the particle is responsible of a restoring force acting on the electrons. When particular conditions are satisfied, this phenomenon results in a resonance which amplifies the field inside and in the near-field zone outside the nanoparticle: this resonance is named Localized Surface Plasmon Resonance (LSPR).

Differently to the case of the Extended Plasmons, Localized Plasmons can be excited directly through direct illumination. Moreover, the characteristic λ of a LSPR depends on the morphological and compositional properties of the nanoparticles involved and on the dielectric function of the medium at the interface. The occurrence of Localized Surface Plasmons can be fully explained in the framework of the Mie Theory [17] for spherical isolated particles in a non absorbing medium.

When the geometry is more complicated or interaction effects between particles occur, numerical simulations based on the Maxwell's equations can be used to study the system. Let's describe the isolated particle, as an homogeneous and isotropic sphere of diameter d and radius a, with a dielectric function $\varepsilon(\omega)$; the surrounding medium, in which the particle is embedded, is non-absorbing with dielectric constant ε_m (see Fig. 1.3).

If the wavelength of the incident beam is much larger than d ($d \ll \lambda$), we can use the
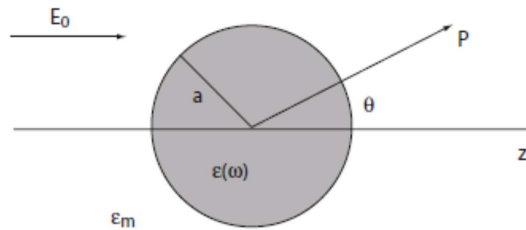
Figure 1.3: Homogeneous sphere in an electric media and illuminated with an electrostatic field with lines parallel to z axis.

quasi-static approximation, i.e., the phase of the oscillating field can be considered constant over the volume of the particle (this is generally adequate for nanoparticles below 20 nm in the visible and near-IR range). The electric field can be expressed as $\mathbf{E}_0 = E_0\hat{\mathbf{z}}$. With the assumptions above, the sphere can be considered an ideal dipole under the effect of this

static field. $\mathbf{E}$ induces a dipole moment $\mathbf{p}$ inside the sphere proportional to $|\mathbf{E}_0|$, expressed by this equation:

$$\mathbf{p} = 4\pi\varepsilon_0\varepsilon_m a^3 \frac{\varepsilon - \varepsilon_m}{\varepsilon + 2\varepsilon_m}\mathbf{E}_0 \tag{1.17}$$

Using the relation between $\mathbf{p}$ and the *polarizability* α ($\mathbf{p}$=$\varepsilon_0\varepsilon_m\alpha\mathbf{E}_0$) we obtain:

$$\alpha = 4\pi\varepsilon_0\varepsilon_m a^3 \frac{\varepsilon - \varepsilon_m}{\varepsilon + 2\varepsilon_m} \tag{1.18}$$

for which a resonant enhancement occurs when $|\varepsilon + 2\varepsilon_m|$ is minimum. If $\mathrm{Im}[\varepsilon]$ of the metal sphere is negligible, this minimum is expressed by the so called *Frölich condition*:

$$Re\left[\varepsilon(\omega)\right] = -2\varepsilon_m \tag{1.19}$$

The Frölich condition shows the dependence of the LSPR from the dielectric function of the medium which surrounds the nanoparticle: in particular for an increase of ε_m the resonance red-shifts (this optical feature of nanoparticles is exploited in many refractive-index sensors' applications). Also the Electric field inside ($\mathbf{E_{in}}$) and outside ($\mathbf{E_{out}}$) the particle is enhanced by this resonance, according to the following expressions:

$$\mathbf{E}_{in} = \frac{3\varepsilon_m}{\varepsilon + 2\varepsilon_m}\mathbf{E_0} \tag{1.20a}$$

$$\mathbf{E}_{out} = \mathbf{E_0} + \frac{3\mathbf{n}\left(\mathbf{n}\cdot\mathbf{p}\right) - \mathbf{p}}{4\pi r^3\varepsilon_0\varepsilon_m}, \tag{1.20b}$$

where $\mathbf{n}$ is the unit vector in the direction of observation.

It is interesting to note that a consequence of the resonantly enhanced polarization α is a concomitant enhancement in the efficiency with which a metal particle scatters and absorbs light. The corresponding cross section for scattering - σ_{sca} - and absorption - σ_{abs} - are [18]:

$$\sigma_{sca} = \frac{k^4}{6\pi}|\alpha|^2 = \frac{8\pi}{3}k^4R^6\left|\frac{\varepsilon - \varepsilon_m}{\varepsilon + 2\varepsilon_m}\right|^2 \tag{1.21a}$$

$$\sigma_{abs} = kIm\left[\alpha\right] = 4\pi kR^3 Im\left[\frac{\varepsilon - \varepsilon_m}{\varepsilon + 2\varepsilon_m}\right]. \tag{1.21b}$$

from which the *extinction cross section* $\sigma_{ext} = \sigma_{abs} + \sigma_{sca}$ can be calculated.

It is clear that the interaction of light with nanoparticles involves both absorption and scattering mechanism and there is a typical size tradeoff for which a mechanism prevails

on the other. Analytical expressions for the *polarizability* can be derived also in the case of ellipsoids particles, where α depends on the particular axes considered and, and for core/shell particles, taking into account a 'inner' and 'outer' radius [18]. For larger particles, for which the 'static' approximation is no longer valid, a rigorous *electrodynamic approach* (still in the framework of Mie's theory) is required leading to additional terms with respect to 1.18. As an example, the effect of the retardation of the exciting field over the volume of the sphere should be taken into account, together with the *depolarization field* inside the particle and a term related to *radiation damping* (i.e., the localized plasmons decay into photons).

The fingerprint of a LSPs excitation is an absorption peak or an intense scattering of the light. Several parameters, such as kind of material, size, morphology, and environment can affect this far field optical response.

The best materials for plasmonic applications are the noble metals: their values of n and k allow minimizing the losses while maintaining the high enhancement of the field typical of ESPs and LSPs. Among them, gold allows to couple performing plasmonic features to chemical stability.

Sensing is one of the main and better established application field of Plasmonics [19,20], due to the fact that, as seen before, the Surface Plasmons are extremely sensitive to the optical properties -i.e., refractive index- of the dielectric media surrounding the metal. A further and/or new development of plasmonics can be the realization of fundamental components in nano-photonics, as modulators or switches, for which the control of plasmon properties through an external agent can be obtained. A promising candidate is the magnetic field, as it allows a modification of the optical properties which depends not only on its magnitude but also on its direction. Moreover, differently to other competitive physical agent as, for example, temperature or voltage, magnetism is an ultrafast property [21].

The merging of *Plasmonic* and *Magnetism* gave rise to the new field of *MagnetoPlasmonics*, which, from the appearance of the first articles (around 2007-2008) has been becoming a fast-growing research area. Before introducing some example of elementary mechanisms suitable to couple plasmonic properties and magnetic features, the main basic concepts on magneto-optics will be introduced in the next section.

1.2.2 The Magneto-Optical effects and their interaction with Plasmonic features

As described in the previous section, the optical properties of an isotropic material are fully describe through the *dielectric function* -$\varepsilon(\omega)$-; under the presence of a magnetic field the ε function becomes a tensor where off-diagonal terms, ε_{mo}, appear [22]:

$$\varepsilon = \begin{pmatrix} \varepsilon & a\Pi_z & a\Pi_y \\ -a\Pi_z & \varepsilon & -a\Pi_x \\ -a\Pi_y & a\Pi_x & \varepsilon \end{pmatrix}. \tag{1.22}$$

Here the Magneto-Optical (MO) constants of the material, i.e., ε_{mo}, are written as $a\Pi_i$ being Π_i the components of the *applied magnetic field* (**B**) for paramagnetic and diamagnetic medium, and the *Magnetization* (**M**) for ferromagnetic materials.

Magnetic field induced modifications of the optical properties of materials were first observed by M. Faraday [23] and J.Kerr [24, 25]. They studied the change in the polarization state of the transmitted (*Faraday effect*) or reflected light (*Kerr effect*) when a magnetic field was applied to a glass or to a ferromagnetic material.

Generally speaking, the effect that an external magnetic field has on the light transmitted through or reflected by a materials depends on the relative orientation of the magnetic field and the plane of incidence. The different geometries leading to the MO effects are summarized in Fig. 1.4. For example, in the so called *polar Kerr configuration*, where **B** or **M** is aligned perpendicular to the sample surface (XY), Equation 1.22 takes the form:

$$\varepsilon = \begin{pmatrix} \varepsilon & a\Pi & 0 \\ -a\Pi & \varepsilon & 0 \\ 0 & 0 & \varepsilon \end{pmatrix} \tag{1.23}$$

highlighting the coupling between the X and Y components of the electromagnetic field. This induces a change in the polarization state of the light and consequently, the non-diagonal Fresnel coefficients, accounting for polarization conversion, r_{ps} and r_{sp}, depend linearly on Π. The physical magnitudes, experimentally quantified, are the magnetic field induced rotation θ and the ellipticity φ, experienced by the incident light (mathematically summarized by the complex number Φ, where $\Phi = \theta + i\varphi$).

The figure and table showing Kerr effect and Faraday effect.

Figure 1.4: The MO effects, both in reflection (Kerr effect) and in transmission (Farady effect) are sketched. In the table, the configuration geometry, the corresponding dielectric tensor, the associated reflectivity tensor and the relevant measurable quantities are detailed in the case of the Kerr effect [2].

Conversely, if **B** or **M** is aligned parallel to the sample plane (XY), but perpendicular to the plane of incidence of the light (XZ), Equation 1.22 becomes:

$$\varepsilon = \begin{pmatrix} \varepsilon & 0 & a\Pi \\ 0 & \varepsilon & 0 \\ a\Pi & 0 & \varepsilon \end{pmatrix} \tag{1.24}$$

In this configuration, known as *transversal Kerr*, only the $p-$component of the light will be affected by the applied magnetic field so that the incident light experiences a change in the reflected intensity, without changing the polarization state.

Corresponding effects occur when then transmission of the light is involved (*Faraday ef-*

fects).

As a matter of fact, all the materials exhibit Magneto-Optical activity, but the intensity of this response depends mainly on their magnetic nature.

The magnetic features of some representative materials, together with the optical properties of a noble metal, e.g., gold, and a ferromagnetic metal, e.g., cobalt, are displayed in Fig. 1.5. The magnetic nature can be classified according to the magnitude and sign of
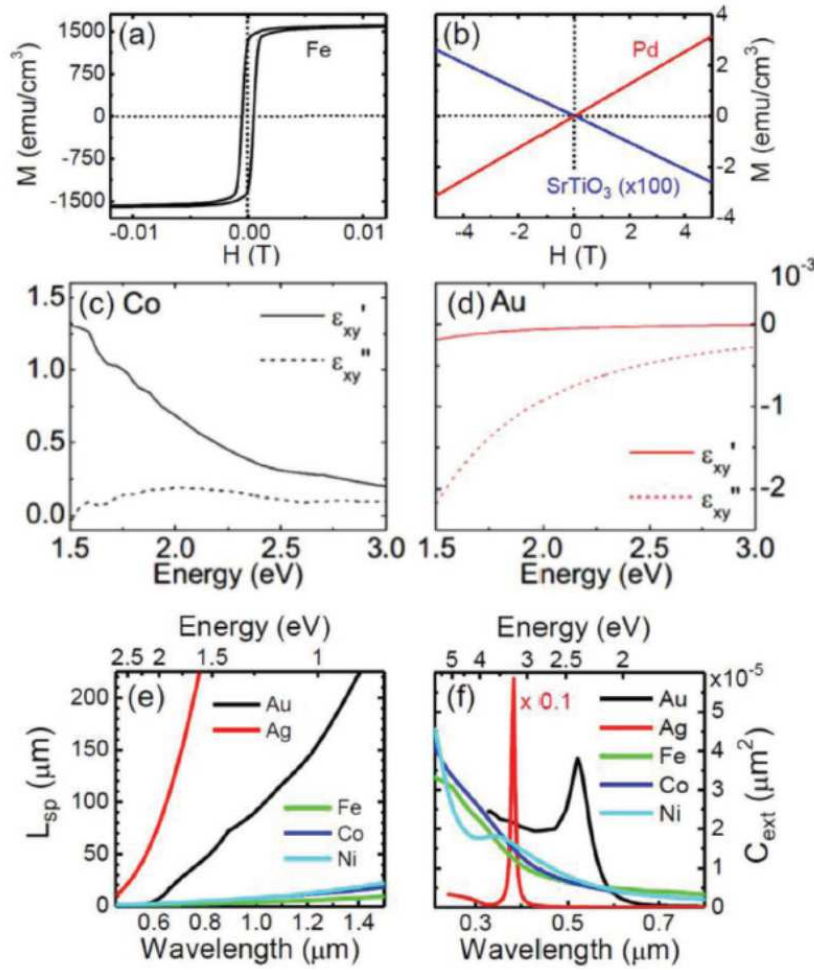
Figure 1.5: Magnetic response for (a) a ferromagnetic material i.e. *Fe* and (b) a diamagnetic, i.e. $SrTiO_3$, and a paramagnetic, i.e., *Pd*, material. Real and imaginary parts of the MO constants of (c) *Co* and (d) *Au*. Calculated SPPs propagation length, L_{sp}, for noble and ferromagnetic metals (e). Calculated extinction cross-section for 10-nm-diameter spheres of noble and ferromagnetic metals in water. All data from [2].

the *magnetic susceptibility* χ, which relates the *Magnetization* **M** to the *applied field* (**H**) through the equation:

$$\mathbf{M} = \chi\mathbf{H}. \tag{1.25}$$

χ is small and positive in the case of *paramagnetic material*s, small and negative for *diamagnetic materials* and large and positive in the case of the *ferromagnets*. In these last ones, differentially to the formers materials, the Magnetization reaches a saturation state at small magnetic field values (see Fig. (a) and (b)). It is clear that the MO constants of ferromagnets are order of magnitude larger than those of paramagnetic and diamagnetic materials.

The physical origin and magnitude of the MO response of noble metals (which, as seen, are the most used in plasmonics) can be described, similarly to the optical properties, in the framework of Drude model (see section 1.2.1), leading to the expression for the MO constants:

$$\varepsilon_{mo} = i \frac{\omega_c (\omega_p \tau)^2}{\omega \left[(1 - i\omega\tau)^2 + (\omega_c \tau)^2 \right]} \tag{1.26}$$

where τ is the electron relaxation time, ω_p is the plasma frequency ($\omega_p = \sqrt{Ne^2/\varepsilon_0 m^*}$) ω_c is the cyclotron frequency ($\omega_c = eH/m^*$), being e the electron charge, N the electron density, H the applied magnetic field and m^* the electron effective mass.

Typically, for feasible magnetic fields, the ω_c value of noble metals is much smaller than ω_p, and therefore the resulting MO constants are small [26]. On the contrary, the MO activity of ferromagnetic materials is much larger with respect to noble metals, due to spin-orbit coupling, exchange interaction and the specific band structure. As depicted in Fig. 1.5 (c) and (d), the MO values for Co are approximately three orders of magnitude than those for Au, in the whole frequency range.

To push *plasmonics* toward novel technological developments, especially in the field of telecommunication where all-optical arrangements are required, it is mandatory to add new functionalities to the plasmonic system. A key role in this process can be under-taken by *Magneto-Plasmonics*, where a bi-directional connection between plasmonic and magneto-optical phenomena occurs. On one hand, indeed, the application of a magnetic field allows tuning the plasmonic features and, on the other hand, the MO effects can be largely increased by plasmon resonance excitations.

An optimum combination of both magneto-optic and plasmonic characteristics is typically achieved mixing ferromagnets and noble metals: sizable MO properties are maintained while the losses that unavoidably accompany the electromagnetic field amplification, are minimized. Great part of the magneto-plasmonic literature is dedicated to systems where a thin layer of ferromagnetic metal is coupled to a thin layer of noble metal, the arrangement

being a continuous film or a nanostructured array.

To introduce the plasmon resonance effect on the MO activity, let's first consider an Au/-Co/Au tri-layered film illuminated by a Kretschmann (i.e., Attenuated Total internal Reflection -ATR-) configuration [27], where a minimum in the reflectivity is a signature of the plasmon (in this case extended) excitation. This affects the value of r_{pp} (pure optical contribution), which assumes a minimum. Considering now, that the complex Kerr rotation Φ, in polar configuration is:

$$\Phi = \theta + i\varphi = r_{ps}/r_{pp} \qquad (1.27)$$

(where r_{ps} is the polarization conversion due to the pure MO contribution), it is evident that a MO enhancement occurs in correspondence to this minimum of the pure optical contribution. On the other hand, regarding the pure MO contribution, the polarization conversion r_{ps} cas be expressed as [28]:

$$|r_{ps}| = \langle E_p E_s \rangle \, d \, |\varepsilon_{mo}| \qquad (1.28)$$

where d is the thickness of the ferromagnetic material characterized by a MO constant ε_{mo} and $\langle E_p E_s \rangle$ is the mean value of the product of the field component inside the magneto-active layer. The field enhancement achieved through the plasmon resonance excitation, leads to an increase of the r_{ps} coefficient and, consequently to a MO amplification.

As already cited in the section 1.2.1, ESPs can be excited directly through periodic arrays. Their effect on the MO activity has been reported in hexagonal arrays of sub-wavelength holes in optically thin cobalt [29], iron [30] and nickel membranes [31]. For instance, in [32], a correlation between the reflectivity minima and the maxima in the polar Kerr rotation at normal incidence is demonstrated. Large enhancement of the MO effect at the peculiar transmission peaks (i.e., the Extraordinary Optical Transmission peaks explained in section4.4) of a perforated Au layer, were predicted in [33,34] for noble metal/garnet system. Experimental evidence of these effects are described in [35] for similar material arrangements.

Since the pioneering work of Hui and Stroud [36], the consequence of the Localized Surface Plasmons on the MO activity has been investigated in many nanostructured ferromagnetic materials. As an example, the occurrence of a LSPR, in an hexagonal array of Ni nanowires, produces an enhancement of the Kerr rotation [37]; the main contribution arises from the increase of the r_{ps} coefficient -respect to that of the corresponding continuous layer- rather

than from a pure optical contribution (i.e., r_{pp} coefficient). Also Ni nanodisks exibit LSPR, whose spectral position depends on the disk diameter; it has been demonstrated that, not only the intensity but also the sign of the longitudinal Kerr rotation is affected by the plasmon excitations [38]. This is explained through a change in the sign of the real part of the particle polarizability (across the resonance position) which is transferred to the MO response.

The insertion of a dielectric layer allows engineering the electromagnetic field distribution within a metallic nanostructure; this is exploited, for instance, in an arrangement of Au/Co/Au nanodisks, where a fine-tuning of the position of a silica inter-layer leads to a reduction of the optical losses in correspondence to the MO enhancement [39].

The effects of an external magnetic field on plasmon resonances have been mainly investigated in systems supporting ESPs. When the magnetic field is applied either perpendicular to the surface or parallel to the propagating plasmon wavevector (i.e. polar and logitudinal configuration), it induces a Transverse-Electric (TE) component in the initially pure Transverse-Magnetic (TM) surface waves; moreover a dependance on Π^2 (where Π is the magnetic term, see 1.22) is introduced in the ESPs dispersion relation. Oppositely, a magnetic field applied in the interface plane and perpendicular to the ESPs wavevector (transversal or Voigt configuration) induces a term linear with Π in the ESPs dispersion relation. The possible configurations leading to a magnetic field effect on the plasmonic properties are schematized in Fig. 1.6. It is worth noting that in the Voigt configuration, which preserves the TM character of the plasmon, the Surface Plasmon is modified and a magnetic-field induced non-reciprocity effect appears i.e. $\omega(\mathbf{k}) \neq \omega(\mathbf{-k})$.

The wavevector modulation has been investigated in Au/Co/Au structures by means of a plasmonic interferometer [40], demonstrating that it depends on the Co layer thickness and position. The main contribution to the modulation comes from the spectral dependance of the SPPs electromagnetic field inside the ferromagnetic layer rather then the wavelength evolution of the MO constants. Moreover, in this case, a dielectric layer on top of the metal layer can be used to tune the field redistribution inside the Co layer [41].

The magnetic field modulation of reflected light recently demonstrated in magnetoplasmonic crystal -made of a Au grating deposited on a garnet layer- [42], opens the way for the development of active-plasmonic devices in the high frequency regime essential for telecommunications.

The effect of the magnetic field on the LSPs has been investigated in solvent-dispersed
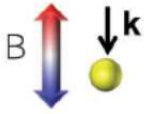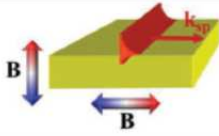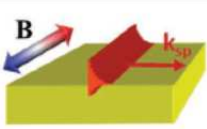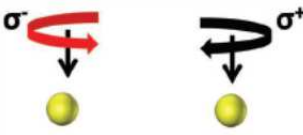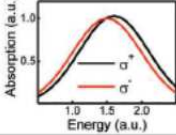
Figure 1.6: On the left, the effect of an external magnetic field (B) on a Localized Surface Plasmon resonance. Considering a spherical particle, when B is applied parallel to the propagation direction of the light, the spectral position of the absorption peak is different for left-handed or right handed circularly polarized light. On the right, the effects of an external magnetic field on the Surface Plasmon Polaritons are summarized [2].

Au nanoparticles by means of a Magnetic Circular Dichroism technique. A dichroic signal appears when a magnetic field is applied parallel to the circular polarized incident light direction arising from the difference between two absorption spectra collected with light of opposite helicity. It presents a steep slope in correspondence to the localized plasmon excitation that depends on the refractive index of the surrounding medium [43].

An interesting phenomenon has been demonstrated in arrays of ferromagnetic nano-disks, where the influence of the phase of the LSPR on the MO activity was explored. The localized plasmon excitation transverse to the electric field of the incident light, induced through a spin-orbit coupling mechanism, defines the MO response which is experimentally described in terms of Kerr reflectivity measurements [44].

The magnetoplasmonic systems, so far described, were typically composed of a ferromagnetic layer coupled to a noble-metal layer: in this way the two functionalities were put into contact only at the interface (or part of the interface in the case of nano-structured systems). A step forward in the development of magnetoplasmonic arrangements is expected to come from the alloying of a magnetic material with the best performing plasmonic

metals. It is, indeed, possible to extend to a homogenous medium the hybrid magneto-plasmonic modes encountered in layered nanodisks [2], *core@shell* nanoparticles [45], as well as in nanoparticles/matrix systems [46]. Hybridization of plasmonic modes, arising both from the noble metal and the ferromagnetic counterpart, possibly lead to a strong MO activity at the plasmon resonance peak, as the hybrid excitation can be influenced by the application of a magnetic field. Only a few works are dedicated in the literature to alloyed systems, while a comprehensive investigation on their synthesis feasibility and characterization is still lacking.

As an example, the enhancement of magneto-optical effects has been demonstrated in Au-Co nanocomposites thin films [47]. Besides a correlation of the optical properties with the microstructure, it is shown that the higher MO response is obtained for the films exhibiting a higher Co concentration.

1.2.3 Applications

The applications that have attracted the attention of the magnetoplasmonic community are mainly biosensing or forefront photonics and telecommunication devices.

In the pioneering work of Sepulveda et al. [48], a Magneto-Optical Surface Plasmon Resonance transducer based on a Kretschmann configuration allowed to reach an increased limit of detection of adsorbed biomolecules, with respect to standard biosensors.

A different configuration has been proposed to detect chemical and biological molecules in a fluid medium [49]. Here, a strong transverse MO Kerr effect variation is achieved near the SPPs wavelength through an Au/Fe/Au surface plasmon grating.

An improved bulk figure of merit, two order of magnitude greater than any other type of plasmonic sensor, has been theoretically predicted in Au-Co-Au NanoHole array where the sensing signal comes also in this case from the transverse MO Kerr effect [50]. Sensing by means of films perforated with a periodic array of sub-wavelength holes is interesting, but at the same time challenging, due to the typical broad resonance line width. This can be overcome by the combination of suitable ferromagnetic and noble metal components so that it is possible to make use of the MO properties, and consequently of the Kerr effect, rather than the 'usual' measurements of the transmission at normal incidence.

Magnetoplasmonic sensing capabilities in system supporting Localized Plasmons has been tested in array of Au-Co-Au nanodisks [51]. In this case the sharp step of the ellipsometric

phase, occurring at the resonance wavelength, is exploited as detection signal and can lead to a sensitivity four times higher than the features conventionally found in propagating surface plasmon sensors.

Since the modulation of plasmonic properties by an external magnetic field as well as the enhanced MO effects can be exploited to control the light at a sub-micron scale, magneto-plasmonic systems represent a valuable way to develop miniaturized all-optical circuits. The introduction of plasmonic functionalities in the already employed garnet films has been proposed as an innovative design in integrated optical insulators [2].

In particular the non-reciprocity effect of SPPs allow to get optical isolation at nanoscale in plasmonic waveguides with low loss [52]. The same effect has been exploited in novel garnet-based waveguide phase shifter [53], which, working at high speed under the influence of an applied field, open the way to the development of optical phase modulators, isolators and optical clocks for optical information nano-network.

Moving from the telecommunication field, an emerging concept is represented by the so called 'plamonic rulers': the near-field coupling of dimer nanoantennas is combined with magnetic functionalities in order to obtain structural information at the nanoscale.

Finally, it is worth mentioning a fast growing field which takes advantage of both optical and magnetic properties of nanostructures, i.e., the *theranostic* approach, where the optical imaging capabilities and bio-compatibilities of, typically, noble-metal nanoparticles are combined with a therapeutic action (in malignant tissues, for instance). The magnetic counterpart can be exploited as contrast agent [54], as transport agent or to enhance the *hyperthermia* effects [55].

1.3 *Au-Co* System in the literature

As seen in the previous sections, the preparation of alloyed compounds where a noble metal is intermixed with a ferromagnetic material, is very promising to develop systems supporting both plasmonic as well as magnetic functionalities. The present thesis is focused on gold and cobalt, which are among the best performing material respectively in the plasmonic field and magnetic applications (see Fig. 1.5). Very few papers are dedicated in the literature to the alloyed Au-Co system for magnetoplasmonic applications, and moreover a comprehensive investigation on this system, spanning from the structural peculiarity to

the characterization of 'functional' properties as magnetism and plasmonic features, is still lacking.

In this section, an overview of the literature articles dedicated to Au-Co compounds, is presented with particular emphasis on the structural characteristics.

A review of the results concerning the Au-Co system, achieved until 1985 was carried out by Okamoto and coworkers [3]. They collected, in particular, data about crystal structures, metastable phases, thermodynamics and magnetism (i.e., Curie temperatures). The proposed phase diagram for gold and cobalt is reproduced here in Fig. 1.7; this is the equilibrium diagram obtained when the bulk starting metals are treated in thermodynamic conditions. It is clear that at low temperature Au and Co are immiscible. Increasing the
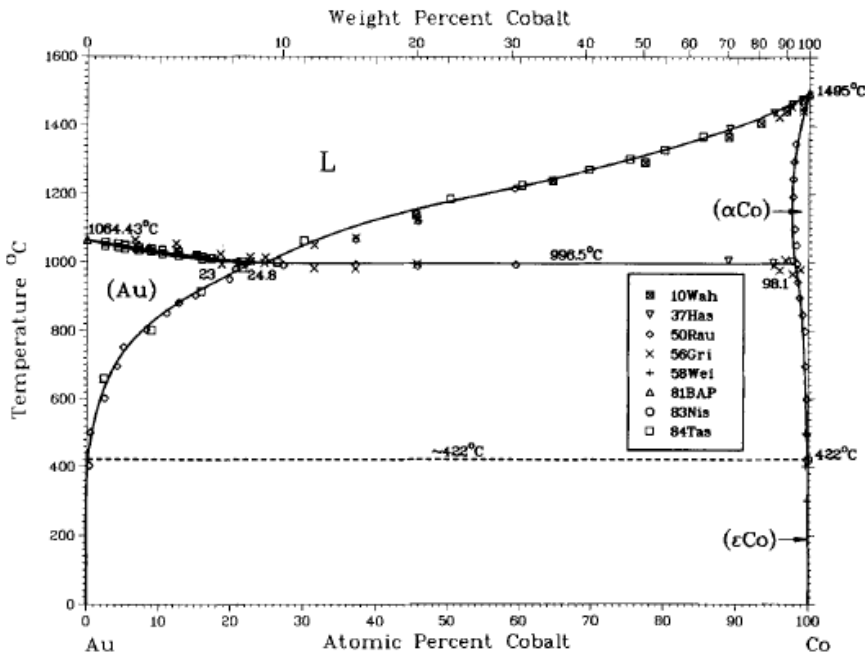
H. Okamoto, T. B. Massalski, M. Hasebe, and T. Nishizawa, 1985.

Figure 1.7: The assessed Au-Co Phase Diagram with selected Experimental Data (for bulk phases). Reprinted from [3]

temperature up to $\approx 1000°C$, alloying takes place with the appearance of a Face Centered Cubic (FCC) phase containing a maximum 25% of cobalt atoms.

Moreover, playing with preparation techniques that allow the materials to growth in 'far-from-equilibrium conditions', it is possible to obtain metastable FCC phases or amorphous alloy phases.

For example, Mader et al. [56] have extensively studied the alloying and related phenom-

ena (stability, phase transformations, microstructure and so on) of thin films (30-100 nm) prepared by a vapor quenching process. The starting close packed metallic components, characterized by a difference of the atomic radii in the range of 22%-2%, were simultaneously evaporated onto a sufficiently cold substrate. That investigation is part of a larger scale research, developed in the 60'-80's on glassy metals and ferromagnetic materials (see also [57]). The authors report the appearance of metastable amorphous phases in a Co film containing 30% Au that undergoes a transformations toward a FCC alloy (around 430°K) which finally evolves into a two phase system ($\approx$ 500°K) where a FCC Au phase is in equilibrium with a HCP Co phase.

Klement [4] studied the Au-Co alloys prepared by splat-cooling from the melt onto a substrate held at RT. Single-phase metastable solid solutions were obtained only in the composition range of 100-58% Au. As the Co concentration increases, the alloy separates into an Au-rich phase, a Co-rich phase and a solid solution. Metastable Au-Co phases have been obtained by Tsaur and co. [6] through an ion-beam mixing process on a multi-layered film (overall thickness around 65 nm) held both at RT and at liquid N_2 temperature. The final microstructure depends on the alloy composition as well as the sample temperature during implantation. Concerning the samples prepared at RT, a single FCC phase is obtained in every case, with a lattice parameter of 3.96 $\pm$ 0.01 Å 3.84 $\pm$ 0.01 Å and 3.70 $\pm$ 0.01 Å for a Co content of respectively 25%, 50%, 75%. The films show a strong texturing with a (111) preferential orientation. When the samples are prepared at LN_2 temperature, the texture becomes weaker so that the $Au_{25}Co_{75}$ film is completely amorphous. In the cases of the other two concentrations, a FCC phase has been obtained with same lattice parameters as in the corresponding RT films.

The results by Mader, Klement and Tsaur are summarized in Fig. 1.8.

All the experimentally achieved lattice constants (FCC stable and metastable phases) have been collected by Okamoto in the aforementioned work and are here re-drawn in Fig. 1.9. The data are slightly outside the straight line of the Vegard's law and show that the lattice parameter decreases as the Co content increases (reaching a value of about 3.6 Å) for an almost pure Co film). It is worth remembering that the Vegard's law states a linear relationship (at fixed temperature) between the crystal lattice constant of solid solution and the concentrations of the constituent elements [58].

More recently, the Au-based systems have been investigated in the context of the research being made on giant magnetoresistance materials [59]. In particular, rapidly solidified rib-

Method	Decreasing Au concentration				
Splat-cooling	100–58% Au single-phase f.c.c. solid solution	58–50% Au two f.c.c. phases : (solid solution + Au-rich phase)	50–31% Au Au-rich f.c.c. phase	31–4% Au three f.c.c. phases : (solid solution + Au-rich phase + Co-rich phase)	0% Au (pure Co) single-phase f.c.c.
Vapour deposition	100–65% Au single-phase f.c.c.	65–25% Au amorphous		25–0% Au single-phase f.c.c.	
Ion-beam mixing	75% Au single-phase f.c.c. (RT and LN$_2$)	50% Au single-phase f.c.c. (RT and LN$_2$)	25% Au single-phase f.c.c. (RT) amorphous (LN$_2$)	5% Au single-phase f.c.c. (RT and LN$_2$)	0% Au single-phase h.c.p. (250°C, RT, LN$_2$)

Figure 1.8: Phases obtained by rapid quenching and ion-beam mixing techniques in the Au-Co system: 'Splat cooling' data from [4], 'Vapour Deposition' data from [5], 'Ion-Beam Mixing data from [6]
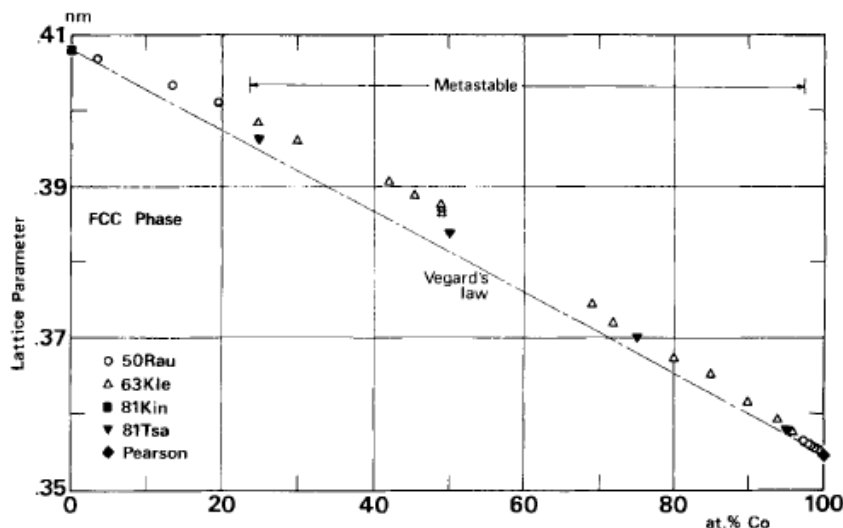
H. Okamoto, T. B. Massalski, M. Hasebe, and T. Nishizawa, 1985.

Figure 1.9: Composition dependance of lattice parameter for the Au-Co FCC phase (including the metastable range). Data from [3, 4, 6, 7]

bons have been obtained by melt spinning or planar flow casting, from a master alloy of Au containing 20% Co (prepared by arc melting of pure metals). XRD analysis reveals (at high angular range) a diffraction pattern composed by two superimposed FCC solid solutions: a minority phase with lattice parameter of about 4.015 Å and a composition corresponding to the master alloy and a main phase of lattice constant $\approx$ 4.052 Å, significantly enriched in gold (the lattice parameter of bulk Au is about 4.08 Å. Given the matter balance, the authors hypothesize the presence of a Co rich phase not detected by XRD measurements

due to the significantly lower scattering factor.

Few works in the literature are dedicated to the Au-Co system at a nanoscale level. Among them, most of the attention is focused on nanoparticles obtained through physical as well as chemical methods [60–62]. Concerning the structural features, Nabika and co. [63] show results (TEM and SAED) on Au-Co nanoparticles prepared through co-deposition onto a PolyAcryloNitrile matrix. They attribute the lattice planes observed in the as-deposited particles (size of the order of 2 nm) to a FCC phase with lattice constant of about 4.02 Å close to that of Au bulk. When the particles are heated up to 870° K the mean size increases up to 8 nm and a phase transformation occurs, leading to the observation of more diffraction lines (corresponding to a Face Centered Tetragonal phase) and a higher inter-planar spacing. The authors claim to have obtained an ordered Au-Co structure starting from a metastable disordered phase.

Sub-micron spheres ($\approx$230 nm) of Au-Co alloy have been obtained through pulsed laser irradiation of colloidal (Au and Co-oxide) nanoparticles [61]. X-ray diffaction patterns reveal a crystal phase whose reflections are in intermediate positions with respect to those of pure gold and pure Co-oxide. In particular, the lattice parameters was in the range of 3.99 Å - 3.96 Å which corresponds, according to Okamoto's data [3], to an atomic percentage of cobalt in the range of 20-30 %. Form SQUID measurements, the alloyed spheres seem to be weakly ferromagnetic without evidence of super-paramagnetic behavior.

Nanocomposites Au-Co thin films ($\approx$50 nm) have been prepared by Yang and coworkers [47] mainly for the purpose of their research on optical and magnetic properties (see 1.2.2). The Co concentration was varied from 5% to 60% through magnetron sputtering co-deposition. The structural characterization was carried out by means of STEM Z-contrast images associated to EELS spectra as a function of the temperature during sample preparation. According to the authors' observations, an amorphous phase has been obtained for the RT coating, that segregates as the deposition temperature increases leading to the formation of Au and Co grains.

2 Au:Co
The material

This Chapter focuses on the structural features of the Au:Co films prepared by magnetron sputtering co-deposition technique. X-Ray Absorption Spectroscopy coupled to X-Ray Diffraction and Transmission Electron Microscopy measurements demonstrate the alloy formation leading, at the same time, to a comprehensive investigation of the Au:Co compounds in terms of stoichiometry and atom arrangement order.
Furthermore, the effect of the composition and of the layer thickness has been systematically investigated.

2.1 Introduction

To investigate the alloying behavior of gold and cobalt at nanoscale level, focusing on the structural features of the obtained nano-composites, as well as on their optical and magnetic properties, three sets of thin films have been deposited through a magnetron sputtering technique. Each set consists of an Au:Co 'balanced film', i.e., with an almost equal content of Au and Co, an Au-rich film and a Co-rich film in which the Au/Co content is 2 : 1 and 1 : 2, respectively. For each composition, different film thicknesses were used: the source power was tuned and the deposition time scaled in order to obtain the desired film thickness and stoichiometry. The considered values of thickness were respectively 15 nm, 30 nm and 100 nm.

The investigation of the alloying behavior of the two metallic elements has been carried out through a full structural analysis by means of X-Ray Diffraction measurements (responsive to the 'long-range' structural order), Extended X ray Absorption Fine Structure (sensitive, on the contrary, to the 'short-range' order) and Transmission Electron Microscopy.

Ellipsometry and UV-Vis measurements were carried out for the characterization of the

optical properties, whose results will be detailed in section 3.1 of the next chapter.

The magnetic properties have been characterized by Superconducting Quantum Interference Device (SQUID), while the magnetic moment acquired by gold in the alloy was detected through X Ray Magnetic Circular Dichroism (XMCD) measurements (see section 3.2).

The thin films were used to obtain nanostructured ordered arrays: the 30 nm thick films were used to coat the Polystyrene Mask in the synthesis procedure of the Semi Nano Shell (SNS) Array (see 4.3), while thicker samples (thickness around 100 nm) were used for the Nano Hole Array (NHA) (see 4.4).

The details concerning the process parameters and the films' stoichiometry are reported in the following section.

2.2 Sample deposition and compositional characterization

Au:Co films were prepared with a custom-built magnetron sputtering deposition apparatus, which allows for the co-deposition of up to three different materials.

The working gas was Argon at a pressure of 5×10^{-2} mbar. Au was deposited with a 2 inch. radio-frequency driven source, setting the power in the range of 28-55 W. In the case of Co (purity 99.95%), a DC magnetron sputtering 2 inch. source was used, providing powers in the range of 48-96 W. The typical deposition rate was around 1-2 Å/s. The sources were tilted of an angle $\approx 30°$ with respect to the axis normal to sample surface allowing a simultaneous deposition of the two metals (see Fig. 2.1 for the deposition geometry).

A rotating sample-holder, grounded to the deposition chamber, allowed for a uniform covering of the substrates and was not intentionally warmed or cooled ('RT' deposition). The source-target distance was about 18 cm (see Fig.2.1).

The substrates were typically silica (HSQ 300 from Heraeus), silicon and, in the case of the thinnest samples dedicated to TEM characterization, carbon coated Cu grids.

The thickness and the composition of the films were properly tuned through an optimized combination of the electrical power to the source and the opening time of the shutters placed in front of the targets.

The films' composition was measured by Rutherford Backscattering Spectrometry (RBS)
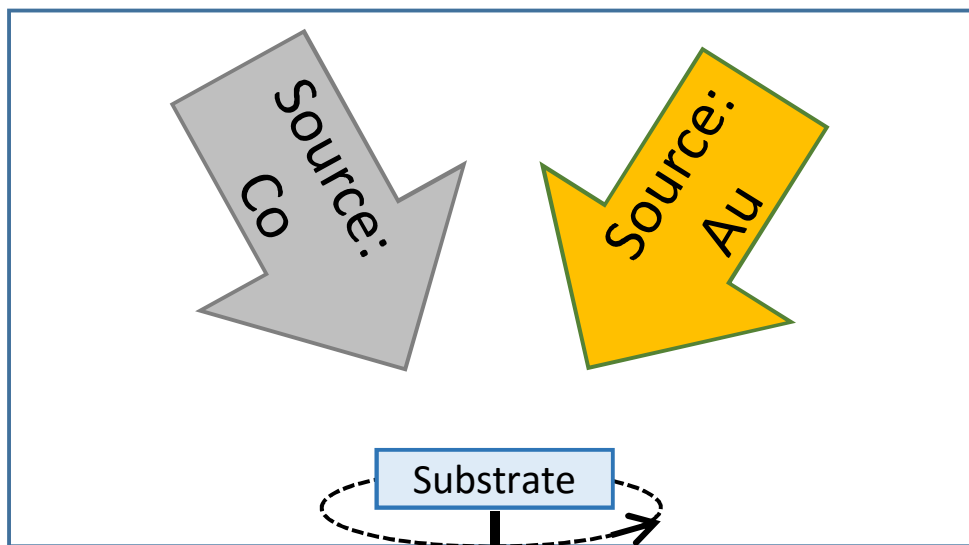
Figure 2.1: The magnetron sputtering geometry for the deposition of Au:Co nanocomposites

performed with a HVEC 2.5 MeV Van de Graaff accelerator at Legnaro National Laboratory (LNL)-INFN, using 2 MeV α-particles at normal incidence and a scattering angle of 20°. The results for the three sets of samples are summarized in Tables 2.1, 2.2, 2.3. The content of Oxygen is under the detection limit of this technique (7% at.)

An example of RBS analysis is reported in Fig. 2.2, where the experimental data related to the 'thick' balance coating, is superimposed to the simulation.

For simplicity, throughout the present work, the 'balanced stoichiometry' will be labeled Au1Co1, while the Au-rich and Co-rich coatings will be named Au2Co1 and Au1Co2 respectively.

30-nm thick film	Au-rich	Balanced	Co-rich
Au content (% at.)	67±1	50±1	33±1
Co content (% at.)	33±1	50±1	67±1

Table 2.1: RBS results for the estimation of Au and Co content (% at.) in the 30 nm-thick films

15-nm thick film	Au-rich	Balanced	Co-rich
Au content (% at.)	75±1	59±1	36±1
Co content (% at.)	25±1	41±1	64±1

Table 2.2: RBS results for the estimation of Au and Co content (% at.) in the 15 nm-thick films

100-nm thick film	Au-rich	Balanced	Co-rich
Au content (% at.)	68±1	53±1	32±1
Co content (% at.)	32±1	47±1	68±1

Table 2.3: RBS results for the estimation of Au and Co content (% at.) in the 100 nm-thick films
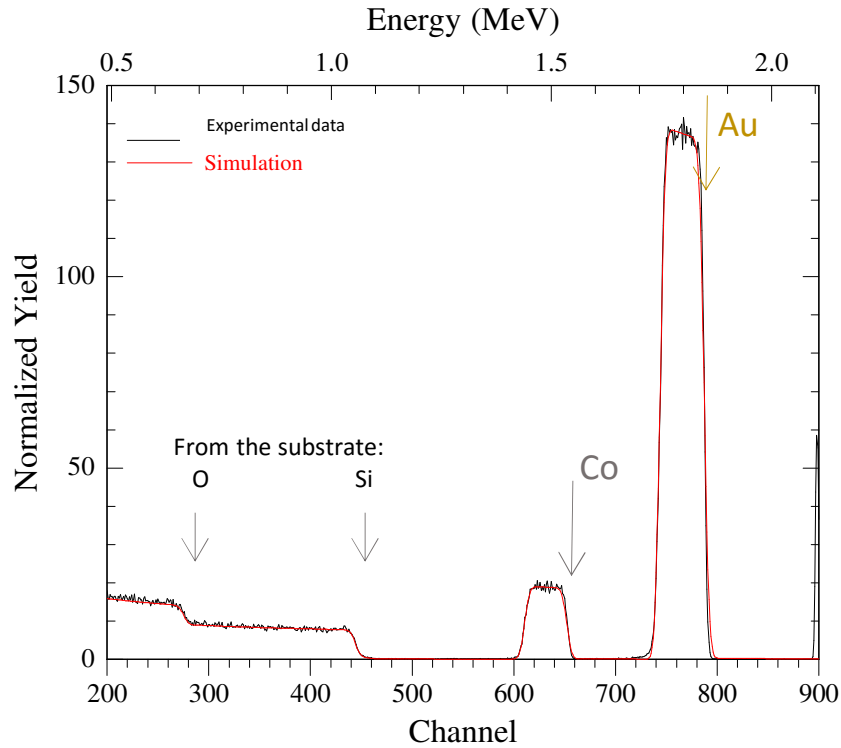
Figure 2.2: A representative example of RBS analysis. In black the experimental data, in red the simulation. The arrows indicate the surface signals from the two metals composing the coatings and the signal from the silica substrate.

2.3 Structural characterization

2.3.1 Structural characterization by XRD

X-Ray Diffraction measurements were performed with a Philips X'Pert PRO MRD triple axis diffractometer (angular resolution 0.01°, accuracy 0.001°) on samples deposited on silica. The working wavelength was the typical Cuk_α emission, arising from the equal contribution of both Cu$k_{\alpha1}$ and Cu$k_{\alpha2}$, i.e., λ=1.5487 Å. Two classes of measurements were employed to investigate the crystalline phases and the texture in the nanocomposite films. A series of scans were performed in Grazing Incidence X-Ray Diffraction geometry (GI-XRD) geometry (see 2.3-a)) with the incidence angle fixed at a 'glancing' angle (typically 0.6°÷0.8°) and the detector spanning an angular range of 25°-85°. The incoming angle was optimized in order to maximize the signal from the coating but, at the same time, to guarantee that the film was completely probed by the radiation. GI-XRD patterns give an overview of the crystalline phases inside the sample. To complement the analysis, also $\omega - 2\theta$ scans, i.e., 'symmetric scan', were performed. In this geometry (see 2.3-b)) the source and the detector are placed at the same angle with respect to the sample surface: in this way the scattering vector ($\bar{s}$) is always perpendicular to the film and the planes contributing to the reflection are only those lying parallel to the surface.
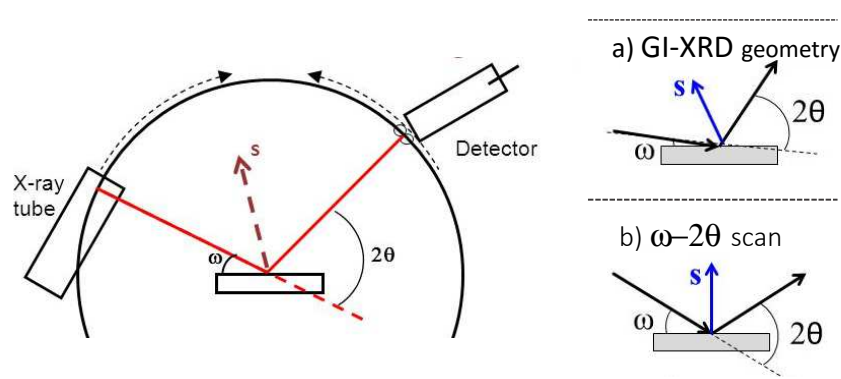
Figure 2.3: On the left, the definition of the ω and θ angle. In a) the geometry to acquire GI-XRD patterns, with a fixed glancing ω angle of the incoming beam and the moving 2θ angle. In b) the geometry adopted to collect $\omega - 2\theta$ scans: here ω and θ moves symmetrically around the axis normal to the sample which is always parallel to the scattering vector (s).

The first analysis to be presented is the one concerning the results obtained for the 30 nm set, which is the intermediate thickness and can be also considered as a reference for many

nanostructures prepared in the second part of the present work (see Chapter 4). Fig. 2.4 reports the GI-XRD pattern for the Au2Co1 sample (acquired with the incoming beam at a fixed angle of 0.8°, with respect to the sample surface), compared to the data obtained in the case of a pure Au film and a pure Co film magnetron sputtered in similar process conditions and with similar thickness.

The sputtered gold grows according to a Face Centered Cubic (FCC) phase with lattice
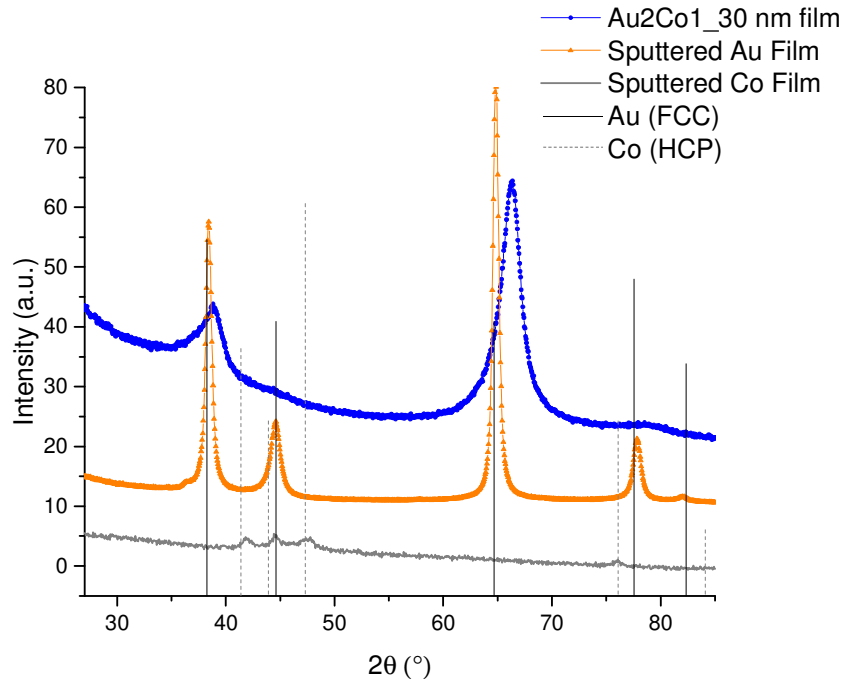
Figure 2.4: GI-XRD patterns of a Au-rich film -in blue-, compared to that of a pure Au sputtered film -in orange- as well as of a pure Co film -gray color-. The data are scaled for readability.

parameter $a_{Au} = 4.06 \pm 0.01$ Å. This value is slightly lower with respect to that reported in literature and also the texturing is different from that of the bulk Au phase [64]. The Co shows an Hexagonal Close Packed (HCP) structure, in agreement with what is reported for the corresponding bulk phase [65]. The pattern related to the A2Co1 sample reveals two broad peaks centered respectively around 38.9° and 66.3°. The experimental pattern can be ascribed to a FCC phase with the first peak corresponding to the (111) reflection and the other peak (higher angle) corresponding to the (220) reflection. Nevertheless, the relative peak intensities indicate a strong preferential orientation of the crystallites. Moreover, the $\omega - 2\theta$ scan, depicted in Fig. 2.5 reveals a strong [111] texturing along the growth direction of the coating, as only one peak, located at 39°, is present. It is interesting to note that

also the polycrystalline sputtered film of pure gold exhibits a preferential orientation as highlighted by the high (111) reflection intensity.
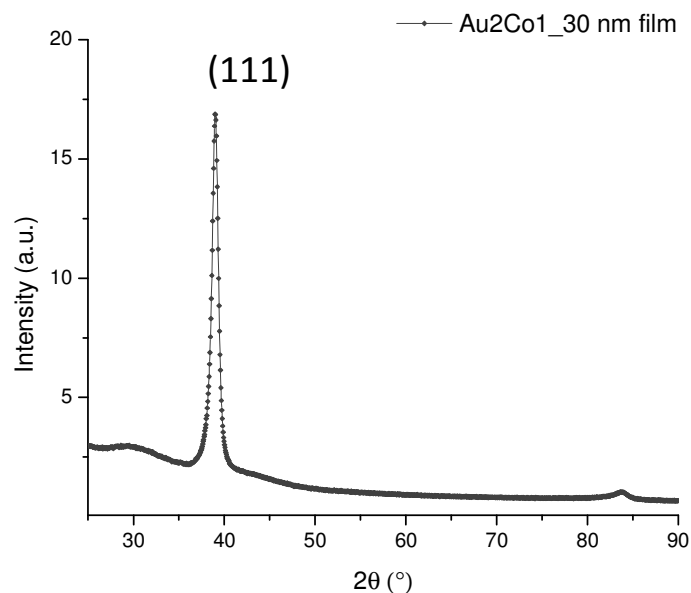
Figure 2.5: A representative symmetric scan on a Au:Co film. Only the (111) reflection of a FCC lattice is detected.

The appearance of a FCC phase is in agreement with the evidence from literature as detailed in section 1.3. Due to the strong texture of our samples, the (200) peak needs to be detected with a symmetric scan around this specific reflection. Firstly, the sample should be properly tilted along the ψ direction (see Fig. 2.6-a) for the angle labelling): we set the ψ angle at a value near the nominal angle between the (111) planes and the (200) planes, i.e., 54.74°, then we tuned this angle in order to maximize the signal and finally we acquired a $\omega - 2\theta$ scan in this 'tilted' configuration. The results are reported in Fig. 2.6 b). This indicates that the mixture of gold with cobalt acquires, during growth, a highly particular texturing, which should be taken into account in further discussions.

The GI-XRD patterns for all the Au:Co compositions are depicted in Fig. 2.7 -left-, together with the reflections due to the phase of pure gold and cobalt. The peaks become broader bands and experience a little shift toward higher angles, as the Co content increases. It is worth noting that, at the wavelength adopted in these experiments, besides a lower scattering factor of cobalt with respect to that of gold, a fluorescence background arises from Co atoms. This leads to a decreasing of the signals as the Co/Au ratio increases and, therefore, the interpretation of the spectra concerning the Co-rich coating, i.e., peaks
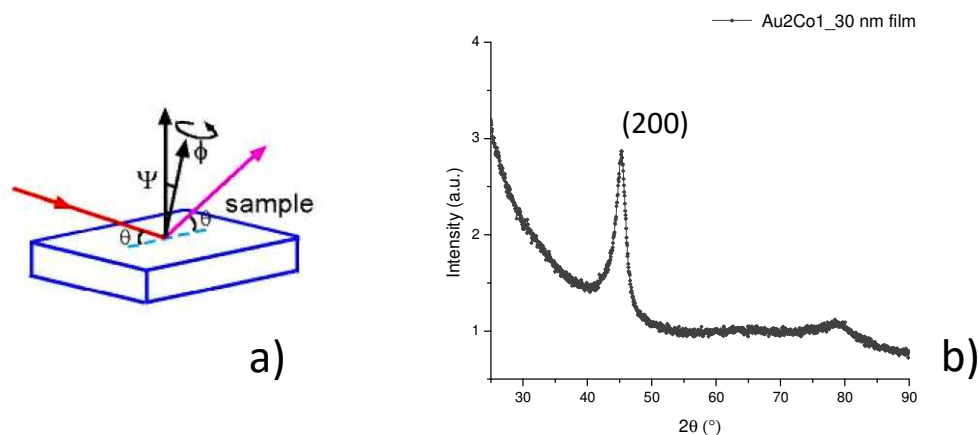
Figure 2.6: a) The tilting geometry adopted to detect the (200) reflection of the FCC lattice. The so acquired pattern is reported in b)

position, Full Width Half Maximum (FWHM) and so on, is quite difficult. Nevertheless, in all the cases, the detected reflections can be attributed to a FCC phase, whose lattice parameter is not that of the sputtered pure gold neither that of the cobalt phase. The corresponding $\omega - 2\theta$ scans are summarized in Fig.2.7 -right-: the peaks centered around $40°$ become predominant, in agreement with the appearance of a strong [111] texturing along the growth direction of the film.
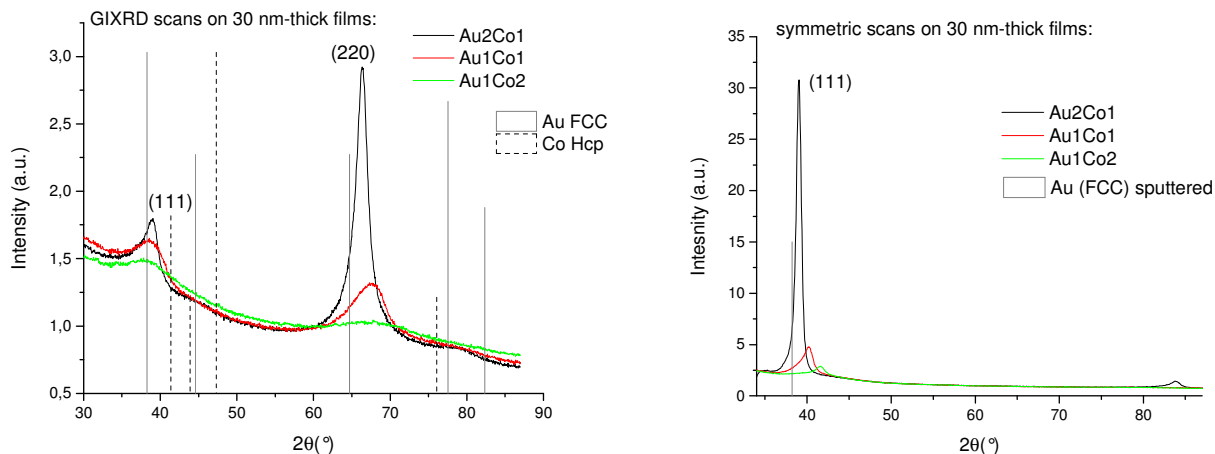
Figure 2.7: On the left, the XRD patterns (grazing incidence geometry) for the 30-nm thick films of different stoichiometry. The data have been normalized to the intensity a $55°$, to take into account possible differences in the illuminated area. The corresponding symmetric scans (i.e. $\omega - 2\theta$) are reported on the right.

Generally, the XRD data indicate the presence of FCC crystalline grains with the (111) planes preferentially parallel to the sample surface and with the lattice parameter getting

shorter as the Co content increases. A more detailed analysis of the (111) reflection in the symmetric scan, reveals that the crystalline phase highly texturized along the growth film direction is actually a mixture of phases. A tail is, indeed, evident towards lower angles, as highlighted in Fig. 2.8. Each of the (111) peak, in the $\omega - 2\theta$ scans, has been fitted with a convolution of two pseudo-Voigt functions: an example of the results of this procedure is depicted in Fig. 2.8, regarding the Au1Co1 film. This detailed analysis reveals that the crystalline portion of the Au:Co films is composed of (at least) two phases. Accordingly to the difference in the peak intensity, their contribution is different: typically, the predominant phases has a maximum at higher angles. The 'secondary' contribution to the peak intensity could alike arises from a mixture of crystallites whose features gradually differ from that of the predominant phase.
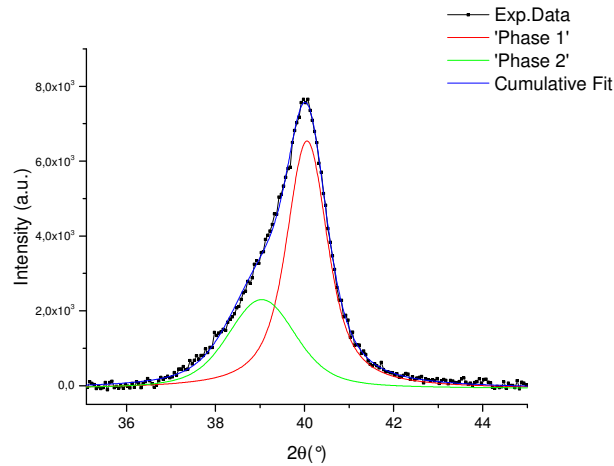
Figure 2.8: An example of peak fitting with a superimposition of two pseudo-Voigt functions.

The lattice constant a can be inferred from the angular position of the maximum, i.e. 2θ, through the expression:

$$a = \sqrt{h^2 + k^2 + l^2}\frac{\lambda}{2sin(\theta)} \tag{2.1}$$

with h, k, l the Miller indices of the planes which produce that reflection and λ is the wavelength. The estimation of the particle size (nm) has been carried out through the Debye-Sherrer formula (see [66]) from the peak FWHM values, taking into account the instrumental broadening. The scenario coming out from the analysis of the symmetric scans is that of two classes of textured grains: a 'predominant' one, with bigger crystalline particles contributing for most of the $\omega - 2\theta$ peak intensity, and a 'secondary' one formed by fine-grained particles with a larger lattice parameter with respect to that characterizing

the previous class. The quantitative results are summarized in Fig. 2.9 as a function of the Co content in the as-deposited film; the literature data from [3] are also reported.
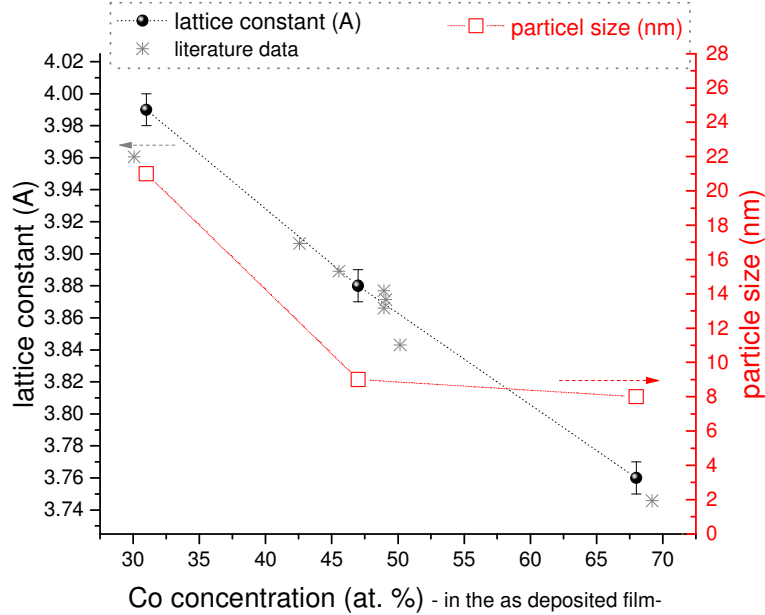
Figure 2.9: Experimental lattice constants of the phase which mainly contribute to the (111) peak intensity in the $\omega - 2\theta$ scans of the 30 nm-thick Au:Co films (dark circle, see axis on the left. The data of the corresponding particle size, along the growth direction, are depicted as red squares (see right axis). For comparison are also reported the literature [3] data of the lattice parameter as a function of the Co content (gray asterisks).

Assuming the Vegard's law (see section 1.3) and taking the experimental lattice parameter of the pure Co and Au thin film –prepared by magnetron sputtering- as limit values, it is possible to infer the composition of the compound constituting these crystalline grains; the Co-rich sample should contains an alloy of composition $Au_{0.35}Co_{0.65}$, while the stoichiometry of the bimetallic compound should be $Au_{0.65}Co_{0.35}$ in the balanced coating and $Au_{0.85}Co_{0.15}$ in the Au-rich sample.

These inferred lattice parameters have then been adopted as 'constraints' values in the analysis of the GIXRD scans. Here, the peak at higher scattering angle arises from the diffraction of (220) planes belonging to the textured crystallites seen before. The signal centered at lower angle is due to the scattering from (111) planes of 'randomly' oriented grains, the only ones that can fulfill the diffraction conditions at that value of 2ϑ in 'glancing' geometry. The peaks have been fitted with the same procedure seen before (two pseudo-Voigt functions) taking into account that the maximum lattice parameter allowed is that of the sputtered gold film (i.e., the experimental value: $a_{Au} = 4.06 \pm 0.01$ Å). The

results are summarized in Fig. 2.10 for all the film compositions where the lattice constant data (see vertical axis on the left) are reported as a function of the particular reflection adopted for the calculation. This allows identifying the textured grains, which give diffraction both through the (111) planes, in the symmetric scans, as well as the (220) planes, in the GIXRD patterns; on the contrary, the randomly-oriented crystallites can contribute only to the (111) peak in the GIXRD scans. The right axis refers to the corresponding R_{M-M} distance, i.e., the first neighbor distance in the lattice, as these values will be useful in further discussions.

Summarizing, XRD measurements detect columnar FCC grains with the main dimension (whose values depend on the initial stoichiometry) perpendicular to the sample surface and aligned with [111] crystallographic direction. In the direction parallel to the substrate, the crystalline ordering is less pronounced, as highlighted by the peak broadening in the GIXRD scans, and the 'long range' order is lost within few nanometers. The lattice constant of these grains is lower than that of sputtered Au moving from 3.76 Å to 3.99 Å as the Co concentration increases; assuming a Vegard-like dependence of the lattice parameter on the alloy composition, this phase should contain an atomic Co percentage of 25 % to 40 %. The remaining fraction of cobalt, is supposed to segregate but is not detected by any XRD scans. This suggests that a consistent percentage of cobalt separates in an amorphous, or at least extremely nanostructured, phase. Moreover, as already noted, the lower X-Ray scattering factor of Co, with respect to Au, further limits the detectability of this phase. Preliminary X-Ray Diffraction (XRD) measurements carried out with a Co k_α X-Ray source do not evidence other phases than those highlighted by the Cu-source diffractometer.

Besides the columnar grains, there are some smaller columns with a lattice parameter relaxed with respect to the previous ones and a fine-grained phase, which is consistent with sputtered gold. The appearance of a textured FCC phase is in agreement with what was presented by Tasur and co. [6] (see section 1.3), who claimed to have obtained a single FCC alloy, highly (111) textured in the case of RT samples. This is not surprising as the sputtering process has some analogies with the ion beam mixing. In both processes, although the energy regimes can be quite different, energetic 'projectile' particles impinge on the Au/Co mixture. In the ion beam mixing, 300keV Xe ions are accelerated toward an Au-Co multiple layer promoting a collision cascade and a motion of the target atoms so that they can be accommodated in a uniformly mixed structure; moreover these atomic

processes are estimated, by the authors, to last for a maximum of 10^{-9} s, thus allowing for a non-equilibrium mixture to be preserved. Also in the magnetron sputtering process, the atoms (or ions) leaving the target and impinging on the growing film own a kinetic energy that can reach a value of tens of eV [67] and can promote adatoms mobility toward an ordered structure; on the other hand the process is quite fast (nearly a monolayer can be deposited per second) allowing for the formation of 'far-from-equilibrium' structures. In both processes, this energy 'surplus' (that reaches a substrate that was not intentionally cooled), allows for more ordered phases to arise, with respect to faster quenching processes performed on LN_2 cooled substrates where an amorphous alloying takes place instead (see for example LN_2 ion beam mixing by Tsaur and the 'vapor quenching' technique by Mader [5, 6]).

Moreover, Mader describes the obtained initial phase as an amorphous metastable alloy that evolves, as a function of the temperature, towards a two phases-system through a metastable FCC alloy (see section 1.3).
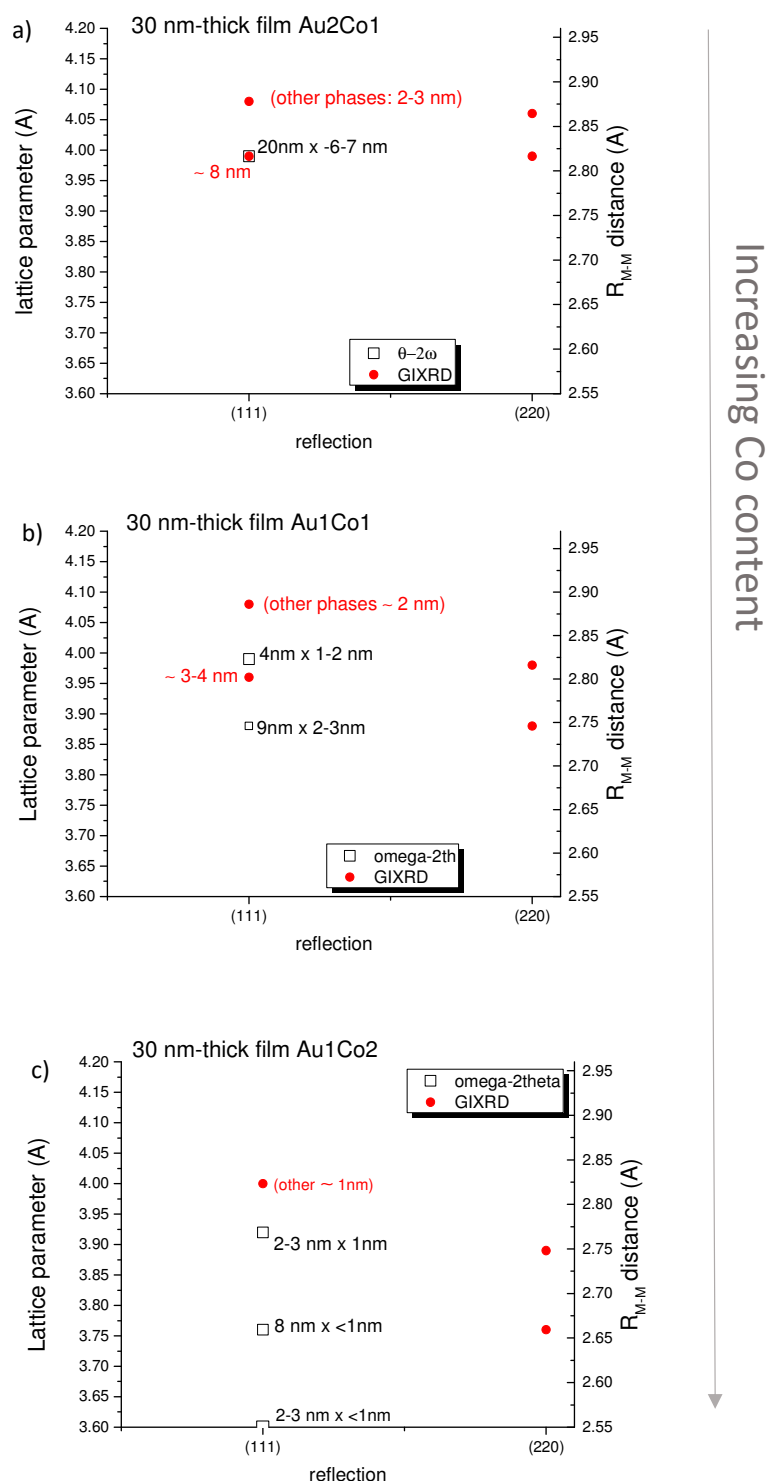
Figure 2.10: A summary of the XRD data (lattice parameter and particle size) as a function of the reflection peak adopted for the estimation. Results concerning the Au2Co1, Au1Co1 and Au1Co2 samples are detailed respectively in a), b) and c). The main dimension of the grains is along the direction perpendicular to the substrate.

2.3.2 Structural characterization by TEM

In order to clarify if the nano-composite films are mostly composed by crystalline structures and to refine the phase identification, thinner samples were prepared as described in section 2.2 and dedicated to Transmission Electron Microscopy (TEM) characterization. Thin films on a copper mesh grid (coated with carbon) were prepared together with a sample on silica, in the same batches. These latest samples were first characterized by GIXRD measurements and the obtained patterns are reported in Fig. 2.11 a) - c), for the composition Au2Co1, Au1Co1 and Au1Co2, respectively, together with data of the corresponding 30 nm-films.
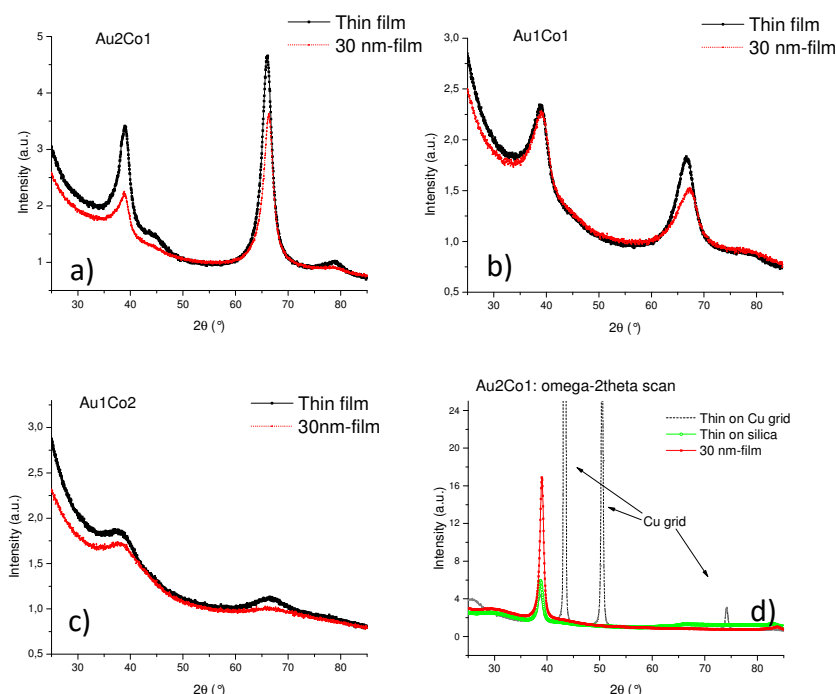
Figure 2.11: GI-XRD patterns of thinner Au:Co films (i.e., 13 $\pm$2 nm) compared to those of the corresponding 30 nm-thick films (a) - c)). An example of $\omega - 2\theta$ scan is depicted in Fig. 2.11 -d), where the data of a Au-rich thin films deposited on a TEM grid are compared to those of the corresponding thin film and a 30 nm-thick film, both prepared on silica

From the comparison, we can see that the position of the peaks are the same within an error of $\approx$1%. These results are also confirmed by $\omega - 2\theta$ scans of which an example is reported in Fig. 2.11 d) related to the Au2Co1 stoichiometry (obviously, for the thin film deposited on the grid, the high intensity peaks due to FCC Cu also appear). Therefore, it is reasonable to think that the thinnest samples and in particular the Au-Co films deposited on the grid for TEM are representative of the crystalline structures inside the thicker coatings. The thin films have been characterized by Bright-Field TEM (BF-TEM),

High-Angle Annular Dark-Field and Scanning-TEM (HAADF-STEM), High-Resolution TEM (HR-TEM) and Selected-Area Electron Diffraction (SAED) patterns. The analysis were performed with a field emission FEI TECNAI F20 Super Twin FEG (S) Transmission Electron Microscope operating at 200kV.

The BF-TEM (see Fig.2.12) reveals white spots, to be ascribed to areas with 0 Z-contrast in the nano-composite, for example Co-rich 'phases', and black spots, which are in turn attributed to Au-rich portions. The dimensions of these black spots are in the range of 3-5 nm for the Au2Co1 thin film and decrease as the Co/Au atomic ratio increases. This picture is in agreement with HAADF-STEM analysis, where a high contrast is related to the presence of heavy atoms. As an example, Fig. 2.13 reports the image obtained on the Au2Co1 sample showing white regions and small black spots.

In order to obtain a more quantitative description of the phases and structures in the films, HR-TEM measurements were performed on all the compositions. The pictures are reported in Fig. 2.14, together with the corresponding Fast Fourier Transform (FFT) images. Given both the observation of lattice planes as well as the appearance of continuous rings on the FTT images, some poly-crystalline grains seem to be present throughout the films. The white spots, particularly visible in the rings of Au2Co1 film, indicate the occurrence of a phase texturing, in agreement with XRD scans. Nevertheless, the white 'halo' in the FTT images is likely related to an amorphous phase which, besides the crystalline fraction, constitutes the as prepared nanocomposites. Also according to HR-TEM the grains appear smaller as the Co concentration increases. The measurements of the inter-planar spacing are compatible with a FCC phase or a mixture of phases; the results are summarized in Table 2.4 together with the attribution of the Miller indices.

The data concerning the Au2Co1 coating show a FCC phase of lattice constant 4.04±0.04 Å together with another FCC phase whose lattice parameter is 3.97±0.05 Å. Also for the balanced Au:Co film, a FCC phase of lattice constant 4.04±0.04 Å seems to be mixed with a FCC phase with a shorter lattice parameter 3.93±0.05 Å. The inter-planar spacing measured in the Au1Co2 coating are compatible with two FCC phases of respectively 4.04±0.04 Å and 3.91±0.05 Å.

These results are congruent with those from XRD analysis: small grains of an Au bulk-like phase are mixed with crystallites characterized by a shorter lattice parameter, belonging to the before called 'secondary' phases. It is worth noting, indeed, that the TEM transmission geometry (with a tilting angle of maximum 30°) does not allow to detect the

crystalline planes arranged parallel to the sample surface, and as highlighted in Fig. 2.10, small randomly-oriented grains of this 'secondary' phase can be detected through the (111) reflection in the GI-XRD patterns. As a consequence, TEM analysis can not give evidence of the 'predominant' phase, mostly contributing to the peak intensity in symmetric scans. In all the samples, no pure or oxidized crystalline cobalt phases have been detected: also TEM measurements, likewise suggestions from XRD scans, indicate that these phases, if present, are in an amorphous state or form very small grains.

Also the SAED analysis, performed on a circular region of radius $\approx$ 100 nm, reveals a polycrystalline structure. The patterns related to the balanced and Au-rich films are reported, as an example, in Fig. 2.15 where a slight texturing is distinguishable in the case of Au2Co1 coating. According to the previous analysis, the rings can be ascribed to a FCC phase with lattice constant of 3.98 $\pm$ 0.04 Å for the Au2Co1 thin film and of 3.94 $\pm$ 0.03 Å for the Au1Co1 concentration. No pure Co or Co-rich phases are detected.
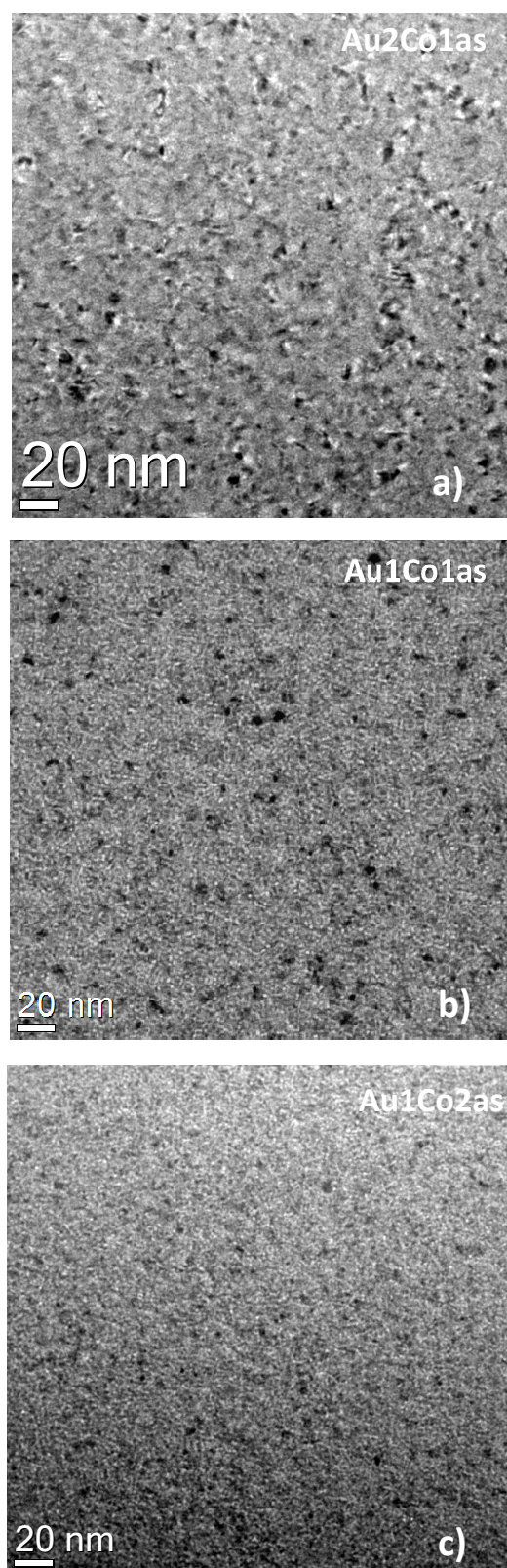
Figure 2.12: Bright-Field TEM images acquired on the thinnest Au:Co samples, respectively for the composition a) Au2Co1, b) Au1Co1 and c) Au1Co2.
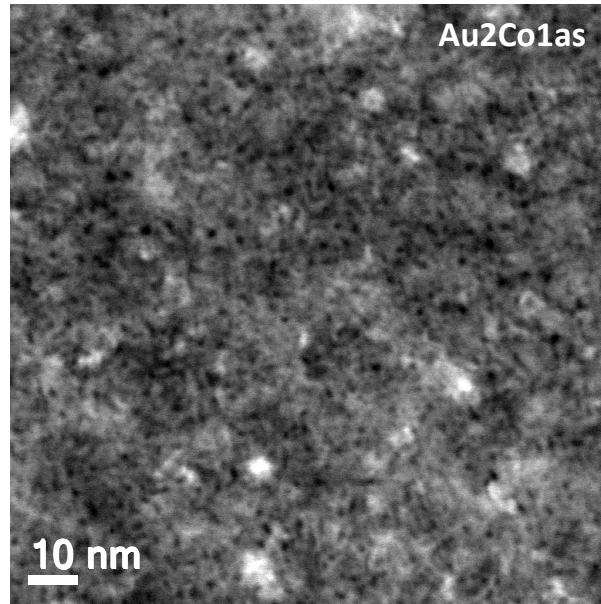
Figure 2.13: A representative HAADF-STEM measurement. The image is related to the Au-rich sample. Similar results have been obtained for the other compositions, confirming the BF-TEM results.

Miller indices (hkl)	Experimental inter-planar distances (Å)		
/	Au2Co1	Au1Co1	Au1Co2
(111)	2.34	2.33	2.33
(111)	2.27	2.27	2.26
(200)	2.00	2.02	absent
(220)	1.44	1.44	absent
(220)	1.44	1.41	absent

Table 2.4: The experimental interplanar distances (Å) inferred from HR-TEM analysis on 15 nm-thick Au:Co samples
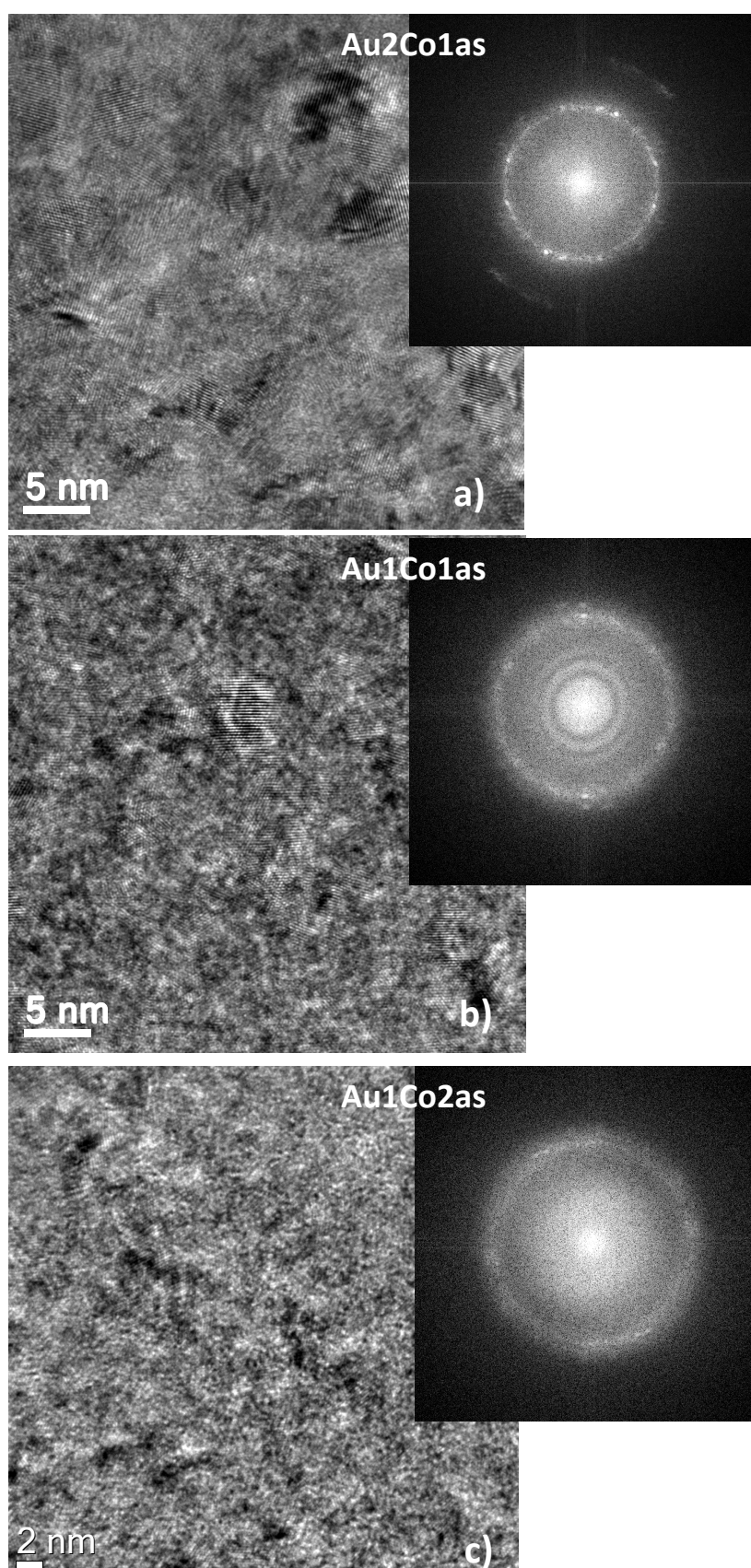
Figure 2.14: High-Resolution TEM images acquired on the thinnest Au:Co samples, respectively for the composition a) Au2Co1, b) Au1Co1 and c) Au1Co2, with the corresponding FFT images
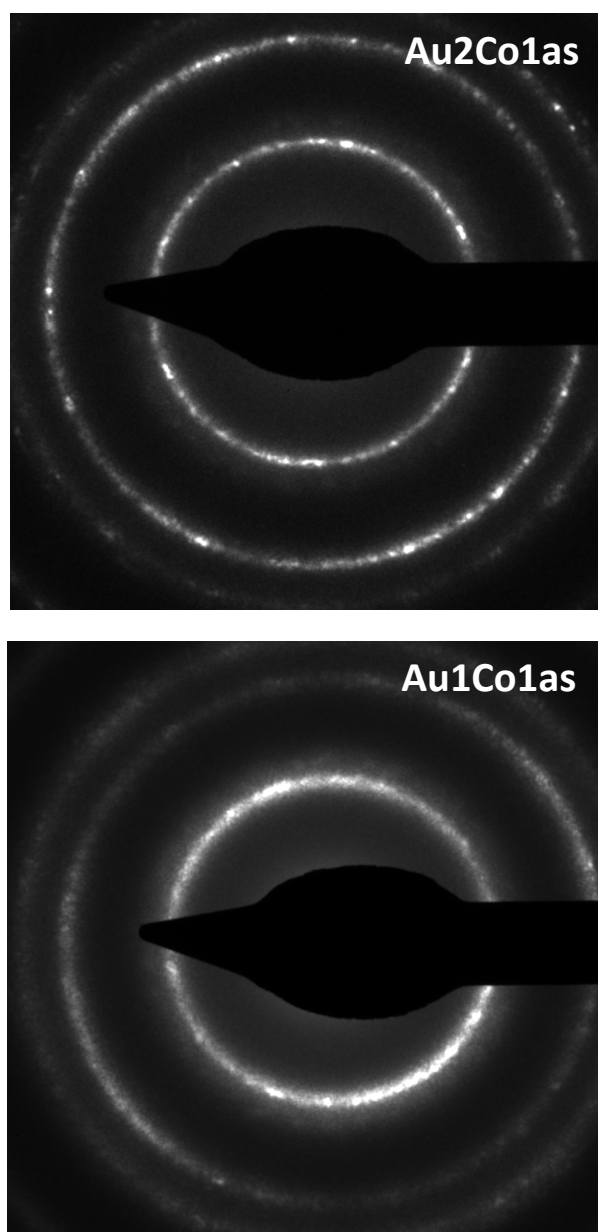
Figure 2.15: The detection and characterization of the crystalline phases by means of SAED analysis. Images of Au-rich and balanced thin films are reported as an example.

2.3.3 Structural characterization by EXAFS

So far, we have seen the structural features that, characterized by a long range order, could be revealed with X-ray diffraction techniques. Nevertheless, the detection of crystalline phases, especially those containing high percentage of gold atoms, could mask the presence of less ordered phases, or due to the low X-Ray scattering factor of cobalt at the Copper $K\alpha$ wavelength (typically adopted in laboratory diffractometers), the presence of Co-rich phases.

For the sake of completeness, it is worth to complement the long-range order analysis presented in section 2.3.1 with a short-range structural characterization that is sensitive, also to possible amorphous structures.

To this purpose, X-ray absorption experiments were performed at the BM08 Italian Beamline of the European Synchrotron –ESRF (Grenoble)- on the 30 nm-thick samples. Both Extended X ray Absorption Fine Structure (EXAFS) and X-Ray Absorption Near-Edge Structure-XANES spectroscopies were carried out at the Au L_3- and Co K- edges in fluorescence mode.

The equipment included a couple of Pd-coated mirrors for harmonics rejection, a (311) Si double crystal monochromator working in dynamical focusing mode and a 13-element HP Ge detector. During the measurements, the samples were cooled at 80 K to reduce thermal vibrations. X-ray absorption spectra of Au and Co metallic foils and of CoO powder pellet, have been acquired in transmission mode as standard reference. Moreover, a Au/Co bilayer , i.e., a 8 nm-thick pure Co layer coated with a 12 nm-thick layer of pure gold, was deposited on silica substrate and measured as well as a reference film.

The spectra analysis was performed by the FEFF8-FEFFIT 2.98 package [68], fitting both the Au-edge and Co-edge spectra for each sample at the same time. The Au-Au and Au-Co single scattering contributions were included in the first shell multiparametric fit in the R-space; similarly, the contributions from Co-Co and Au-Co scattering were taken into account in the analysis at the Co-edge. The constraints imposed to the fit were that the interatomic distance and Debye-Waller (DW) factor of the Au–Co coordination were the same for both edge spectra. Moreover, to reduce the number of the fitting parameters, for each coordination the same DW factor was adopted for all the films. This did not alter significantly the reported results but allowed a better fit stability. To account for possible partial segregation, the EXAFS analysis considered the presence in each film of a Au_xCo_{1-x}

solid solution nanostructured alloy (contributing to the Au–Au, Au–Co and Co–Co coordinations) and of nanostructured Co (contributing to the Co–Co coordination only). The presence of nanostructured Au was considered in a first step, but then excluded, since it did not improve the quality of the fit. Globally, the coordination numbers for the different intermetallic coordinations were bounded to preserve the film stoichiometry measured by RBS.

Looking first at the XANES and EXAFS spectra of the Au/Co bilayer, whose data are superimposed in Fig. 2.16 to those of the metallic Co sheet and CoO powders, the oxidization of the cobalt can be excluded as the onset of the photoelectric absorption occurs at the same energy than for metallic Co and no Co-O (nor Au-O) signal was detected. The
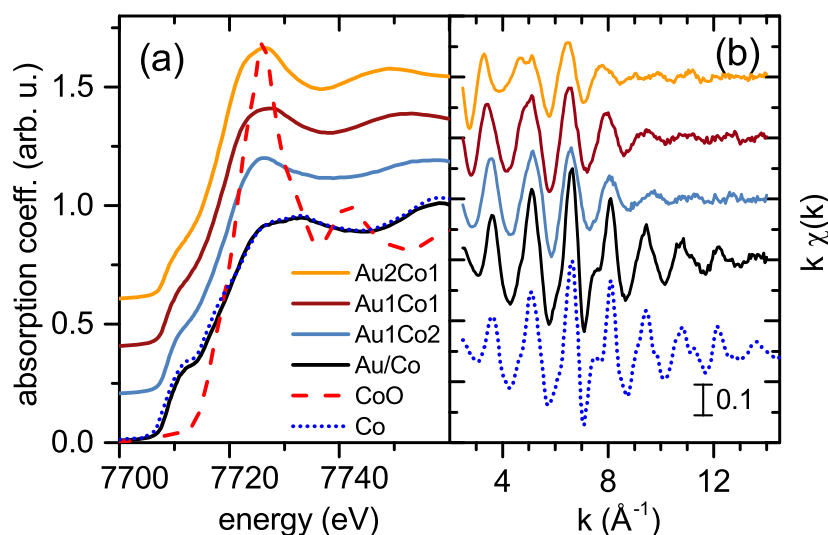
Figure 2.16: Co K-edge (a) XANES and (b) EXAFS spectra for the deposited films, compared to Co and CoO spectra.

first shell analysis did not evidence any Au-Co coordination; the resulting Au-Au and Co-Co interatomic distances turn out to be respectively 2.85 ± 0.01 Å and 2.50 ± 0.01 Å, while the coordination number is in both cases $\cong 12$. These values are slightly lower than that found in the corresponding bulk phases (2.88 Å and 2.51 Å respectively), as it is the case for nanostructured films [69, 70].

The XANES and EXAFS spectra recorded at Co K-edge for the Au:Co bimetallic films are reported in Fig. 2.16 (a) and (b). Also in this case, the Co 1s photoelectric absorption edge energies for the three films indicates that Co atoms are in the metallic state. It is clear that the absorption spectrum, both in the part close to the absorption edge (Fig.

2.16 (a)) and in the EXAFS region (Fig. 2.16 (b)), depends on the Au concentration in the nanocomposite. The combined EXAFS analysis of the Au-edge and Co-edge spectra evidenced a Au–Co first shell coordination, indicating the formation of a Au-Co alloy in all the investigated films. Fig. 2.17 reports data and fit both in R- and in k-space for one representative film (Au2Co1), as well as all the single scattering contributions to the signals.

Nevertheless, an alloy phase alone was not enough to correctly fit the experimental data, so the combined EXAFS analysis of the two Au-edge and Co-edge spectra, considered the presence of a solid solution Au_xCo_{1-x} alloy, as well as of single-metal clusters.
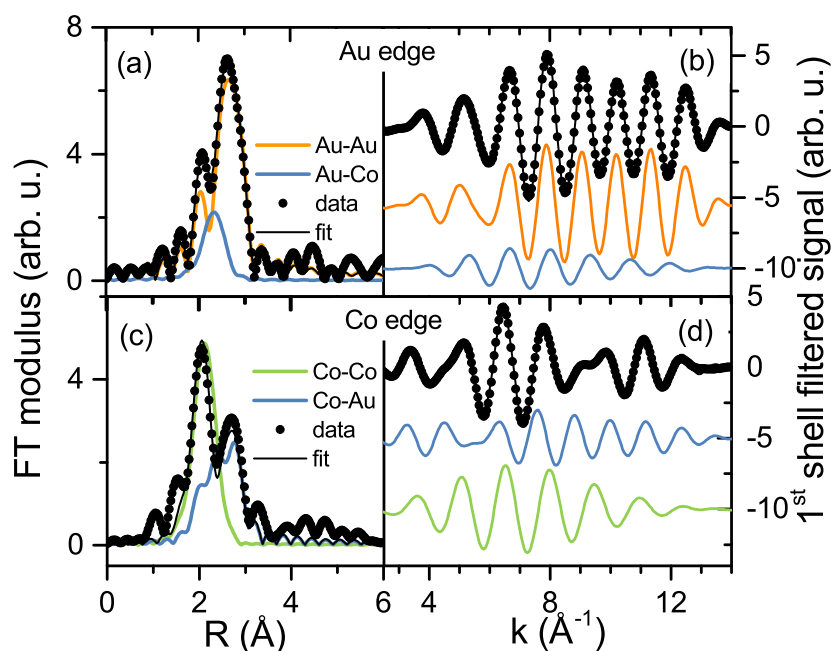
Figure 2.17: Multiparameter first shell fits (intermetallic coordination) superimposed to the EXAFS data for Au2Co1 film ((a,b): Au-edge, (c,d): Co-edge) in the R-space (a,c) and in the filtered k-space (b, d). The single scattering contributions to the fit are reported.

The results of the EXAFS analysis are collected in Table 2.5 for all the samples.

It is worth noting that in a first analysis, the formation of segregated Au nanoclusters (in addition to Co clusters and the alloy) was also considered. Anyway, our data (see Table 2.5) show a Au–Au monomodal distance distribution that depends on the film composition and that is remarkably different from the bulk one, suggesting that it is for the major part related to an alloy phase rather than to Au clusters. This is a first suggestion that what observed through XRD measurements and TEM observations (see 2.3.1), i.e., the presence

Table 2.5: Results of the EXAFS analysis: f_{alloy} is the fraction of atoms in the Au_xCo_{1-x} alloy with first shell coordination number N_{alloy}, R_{A-B} is the A-B first shell coordination distance. The coordination number of Co clusters is N_{CoNCs}. The Debye-Waller factors are $\sigma^2_{Au-Au} = 0.007$ Å^2, $\sigma^2_{Au-Co} = 0.010$ Å^2, $\sigma^2_{Co-Co} = 0.012$ Å^2 for the alloy film, $\sigma^2_{Co-Co} = 0.006$ Å^2 and σ^2_{Au-Au} $= 0.007$ Å^2 for the Au/Co bilayer (uncertainty in the last digit).

FILM	R_{Au-Au}(Å) (± 0.01)	R_{Au-Co}(Å) (± 0.01)	R_{Co-Co}(Å) (± 0.01)	f_{alloy}	alloy comp. x	N_{alloy}	N_{CoNCs}
Au2Co1	2.81	2.69	2.48	0.87±0.09	0.81±0.08	8.5±0.5	6.1±0.5
Au1Co1	2.80	2.66	2.48	0.70±0.07	0.74 ±0.07	7.9±0.5	8.5±0.6
Au1Co2	2.77	2.64	2.48*	0.59±0.06	0.56 ±0.06	5.8±0.5	8.1±0.6
Au/Co bilayer	2.85	-	2.49	-	-	N_{Au}=10.3±0.3	N_{Co}=11.0±0.3
Au bulk	2.88	-	-	-	-	N_{Au}=12	-
Co bulk	-	-	2.50	-	-	-	N_{Co}=12

*Asymmetric Co–Co distance distribution, the estimated third cumulant value is $(6\pm3)\times10^{-4}\text{Å}^3$.

of randomly oriented Au or, at least, Au-rich nanoparticles with average size of $\approx$ 2-5 nm-, actually correspond to a minor fraction of the nanocomposite (below 10 %).

Given the EXAFS results, we can assume that the Au:Co coatings are composed of an alloyed phase, which is the major fraction of the film, and segregated Co clusters, according to the scheme depicted in Fig. 2.18, where the percentages of the constituting metals in the alloy are also reported. Regarding the nanostructured alloy phase, the analysis shows that the it involves a fraction f_{alloy} which includes the majority of the atoms in the films ($0.6 \leq f_{alloy} \leq 0.9$, see Table 2.5 and Fig. 2.18). In addition and more importantly for magnetoplasmonic applications, the alloy composition is richer in Au with respect to the average film composition (see the stoichiometry reported in Fig. 2.18). The coordination number of the alloy phase is lower than the one estimated in the Au/Co bilayer and decreases from about 8 to about 6 with the decrease of the Au concentration, suggesting the formation of sub-coordinated metal sites for lower Au/Co ratio in the film.

The Au–Co intermetallic coordination distance, detected in all the films and at both Au and Co edge spectra, exhibits an intermediate value between the ones of metallic Au and metallic Co, depends on the film composition and increases as the Au concentration in the film is increased. The coordination number for this bimetallic coordination varies in the range 1.5-2.5 when measured at Au edge and in the range of 1.5-4 when the Co edge is considered. The effect of the alloy composition and of the Au–Co distance on the local magnetic properties of the films will be discussed in section 3.2.1.

For each film, the three interatomic distances (Au-Au, Co-Co and Au-Co) differ one from each other as it is usually the case when the atomic radius of the constituent metals are quite different, both in a FCC alloy [71, 72], as well as in metallic glasses [73]. The av-
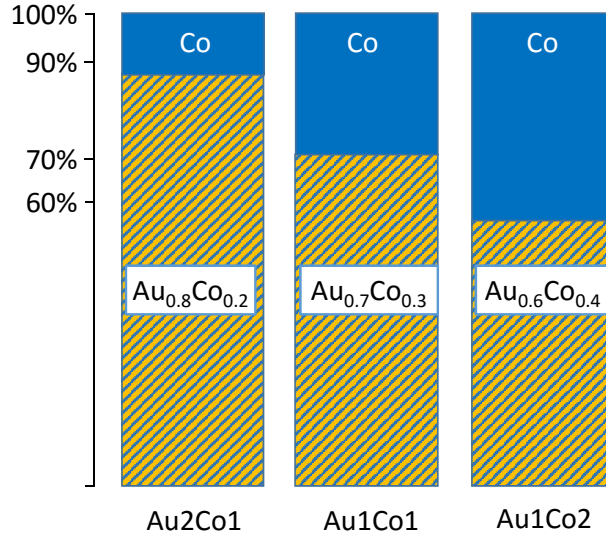
Figure 2.18: Fraction of the alloy and segregated phases for the three Au:Co films. The compositions of the alloyed phases are reported as well.

erage nearest neighbor distance for the Au_xCo_{1-x} alloy, estimated by taking into account the three distances weighted by the alloy composition, is 2.76±0.01 Å, 2.72±0.01 Å and 2.65±0.01 Å for the Au2Co1, Au1Co1 and Au1Co2 films, respectively.

Additional information on the structural disorder, can be inferred through the Debye-Waller factor σ^2 of the different coordinations; the present analysis leads to $\sigma^2_{Au-Au} < \sigma^2_{Au-Co} < \sigma^2_{Co-Co}$, i.e., the Au-Au atomic pair (with a contracted distance with respect to the single-metal phase) exhibits a lower structural disorder with respect to the Co-Co pair. It is interesting to compare the present results for the Au1Co1 film with the ones for the Au/Co multilayer (stack of 30 groups of 0.9 nm thick Au and 2.6 nm thick Co bilayers) reported in literature [74]. In that case the Au-Co mixing was strictly limited to one atomic layer, and the interplanar distance was increased (decreased) for Co (Au) at the interface, with respect to the pure metal phase. Moreover, the interplanar distance of the Au layer at the interface corresponded to a nearest neighbor distance of 2.77 Å, while the interplanar distance of the Co layer at the interface corresponded to a nearest neighbor distance of 2.62 Å [74]. These values are pretty similar to the Au–Au and Au–Co nearest neighbor distances in our Au1Co2 film, in agreement with the picture that the interface mixing, limited to one atomic layer in the multilayer case is extended here to the whole film thickness.

As already discussed, the structural results show a partial Co segregation, involving a mi-

nor fraction of atoms in the films (see also Fig. 2.18). To measure the degree of alloying, the Cowley short range order parameter α, is often used [75]. For a A:B binary system with atomic ratio A/B=y/(1-y), $\alpha_A = 1\text{-}N_{AB}/(N_A(1-y))$, where N_A is the total coordination number of the A site and N_{AB} is the coordination number of the hetero-metallic coordination of the A site. For a completely random mixing α=0, while for complete phase separation α=1. In the present case α_{Co}, i.e., measured for Co-edge, is positive and is the highest for the Au1Co2 film (α_{Co}=0.36, 0.64 and 0.68 for the Au2Co1, Au1Co1 and Au1Co2 films, respectively). This suggests that the elemental mixing is favored for higher Au/Co ratio in the film.

Regarding the fraction of segregated Co clusters, the effective coordination number is on the average lower than that for Co in the bilayer, indicating a stronger nanostructuring of this phase in the bimetallic films. As noted above, the Co–Co coordination takes contribution from both the Au_xCo_{1-x} alloy and from Co clusters. It is worth noting that for the Co-rich film, where a considerable fraction of segregated Co is present, the use of an asymmetric Co–Co distance distribution, skewed towards longer Co-Co distances (positive third cumulant), improved the fit quality. The obtained third cumulant value (see Table 2.5) is in agreement with the results found for ion irradiated Co nanoparticles and suggests a highly defective Co phase [76].

2.4 Discussion

As elucidated in section 2.3.1, the XRD measurements performed on 30 nm-thick films detected elongated crytallites, whose FCC (111) planes lie preferentially parallel to the substrate. These grains are the predominant portion of the crystalline phases detected by X Ray Diffraction. The corresponding lattice parameters are in the range of 3.99 Å – 3.75 Å as the Co content increases: from these values the nearest neighbor distance results to be respectively 2.83 ± 0.01 Å for the Au-rich sample, 2.75 ± 0.01 Å in the case of Au1Co1 sample and 2.66 ± 0.01 Å for the Co-rich sample. These nanoparticles are mixed with a fine-grained minority phase (also highlighted by HR-TEM and the electron diffraction) whose lattice parameter increases from the above values to that of 'pure sputtered' gold (lattice constant ≈ 4.06 Å).

On the other hand, the average nearest neighbor distance for the Au_xCo_{1-x} alloy estimated by EXAFS analysis, tacking into account the alloy stoichiometry, (see 2.3.3) are 2.76 ±

0.01 Å, 2.72 ± 0.01 Å and 2.65 ± 0.01 Å respectively for the Au2Co1, Au1Co1 and Au2Co1 films.

In Fig. 2.19 the comparison between the nearest neighbor distances (R_{M-M}) inferred separately from XRD and EXAFS data is reported.
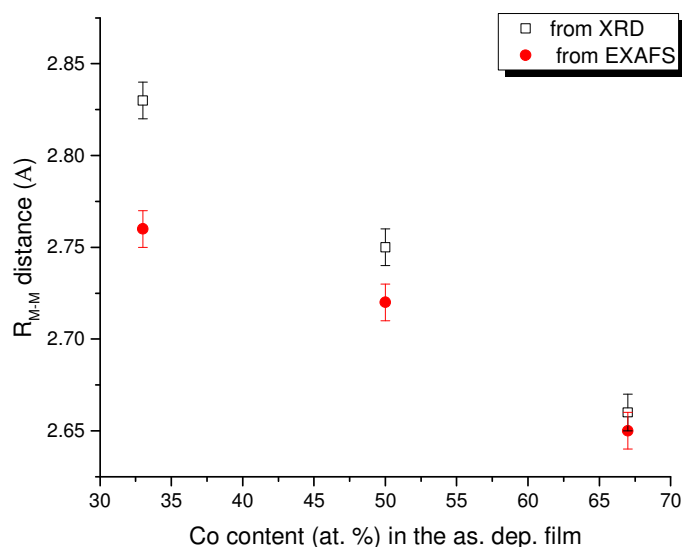
Figure 2.19: Comparison between the nearest neighbor distance - R_{M-M} (Å) inferred from XRD and EXAFS analysis, as a function of the initial Co content.

In the case of Au2Co1 film, the interplay between a structural 'long range' analysis and 'short range' characterization suggests that the alloy phase is largely amorphous, as the value of R_{M-M} distance resulting from XRD measurements is far from that estimated by EXAFS analysis. On the contrary, the alloyed phase in the Au1Co2 sample seems to be more ordered, as the two R_{M-M} values are compatible within errors. An intermediate situation is shown by the Au1Co1 coating, where the alloy is most likely partially crystalline. It is worth underlying that the 'long range' order expires, in any case, in a length scale of some nanometers. This is evidenced by the short 'lateral' dimensions of the grains in the balanced and Co-rich samples (see Fig. 2.10). Moreover, the estimation of the coordination number (from EXAFS, see Table 2.5) is in agreement with this picture as the obtained values -decreasing from 8 to 6 as the Au concentration decreases-, are lower than the one estimated in the Au/Co bilayer. This suggests that the phase is highly fragmented, and, especially for Co-rich nanocomposites, the particles are small and the metal sites are sub-coordinated.

As seen in section 1.3, literature studies show the occurrence of an amorphous alloy between gold and cobalt [4, 5, 47], as well as a crystalline Au-Co phase [3], depending on the process condition.

As a matter of fact, a crystalline metastable alloy would be favored, from a thermodynamic point of view, with respect to an amorphous structure, also in the case of 'immiscible' (in the bulk) materials. Nevertheless, a disordered phase is expected when the size difference between the constituent atoms is large (as for Au-Co system where the size factor is 12-15%) and the speed of the process is high or the energy of the particles arriving at the substrates is low, allowing to reach far-from -equilibrium conditions. This is the case of vapor quenching [5, 56, 57] and splat-cooling [4] where the arriving atoms 'freeze' in place close to their points of landing and this could be also the case of the sputtering process proposed by Yang [47] as well as that adopted in this work. According to our process condition (see section 2.2), the typical deposition rates are in the range of 1-2 Å/s: the impinging particles, carrying typically an energy of about ten eV, do not have enough time to accommodate in a 'more thermodynamic' configuration.

The structural analysis on our samples, prepared by a co-focusing magnetron sputtering deposition, shows a scenario which depends on the initial Co content. In the case of Co-rich and balanced coatings, the presence of alloyed crystalline seeds, elongated along the growth direction, is suggested by symmetric X-Ray Diffraction scans. The phase appears at the same time highly fragmented and is mixed with segregated Co clusters, which most probably are extremely nano-structured and/ or amorphous. The fine grains of the other phases, detected by XRD and characterized by a longer lattice parameter (up to the value of sputtered Au), constitutes a minor part of the nanocomposites, i.e., under 10 %, as no evidence of these phase comes from EXAFS analysis.

It is worthwhile to note, that the X-Ray Diffraction can detect crystalline grains also when they are present in small percentage, if the scattering factor is high enough (and this is the case for gold atoms). This technique can, indeed, gives 'partial' information on the structure of the coating, restricted to the crystalline phase. On the contrary, EXAFS analysis gives an overview on the 'whole' material constituting the sample, besides on an 'atomic' scale, irrespective of the crystalline order.

In addition, the values of the coordination distance obtained by EXAFS analysis, shed new light on the results from XRD measurements, especially for what concerns the Au-rich sample. As the Au-Co average distance does not correspond to any of the lattice

parameter of the crystalline phases revealed by GI-XRD patterns and $\omega - 2\theta$ scans, these latter phases are most likely related to Au or Au-rich 'stressed' phases, with shrinked inter-planar distance depending on the crystal axis and a (111) preferential texturing along the film growth direction. Again, these crystallites are a minor fraction of the entire nanocomposite. The alloyed phases, certainly highlighted by the Au-Co coordination in the 'short range' analysis, is supposed to be amorphous.

To conclude, Fig. 2.20 reports a scheme summarizing the main results of the structural characterization, on Au2Co1, Au1Co1 and Au1Co2 samples.
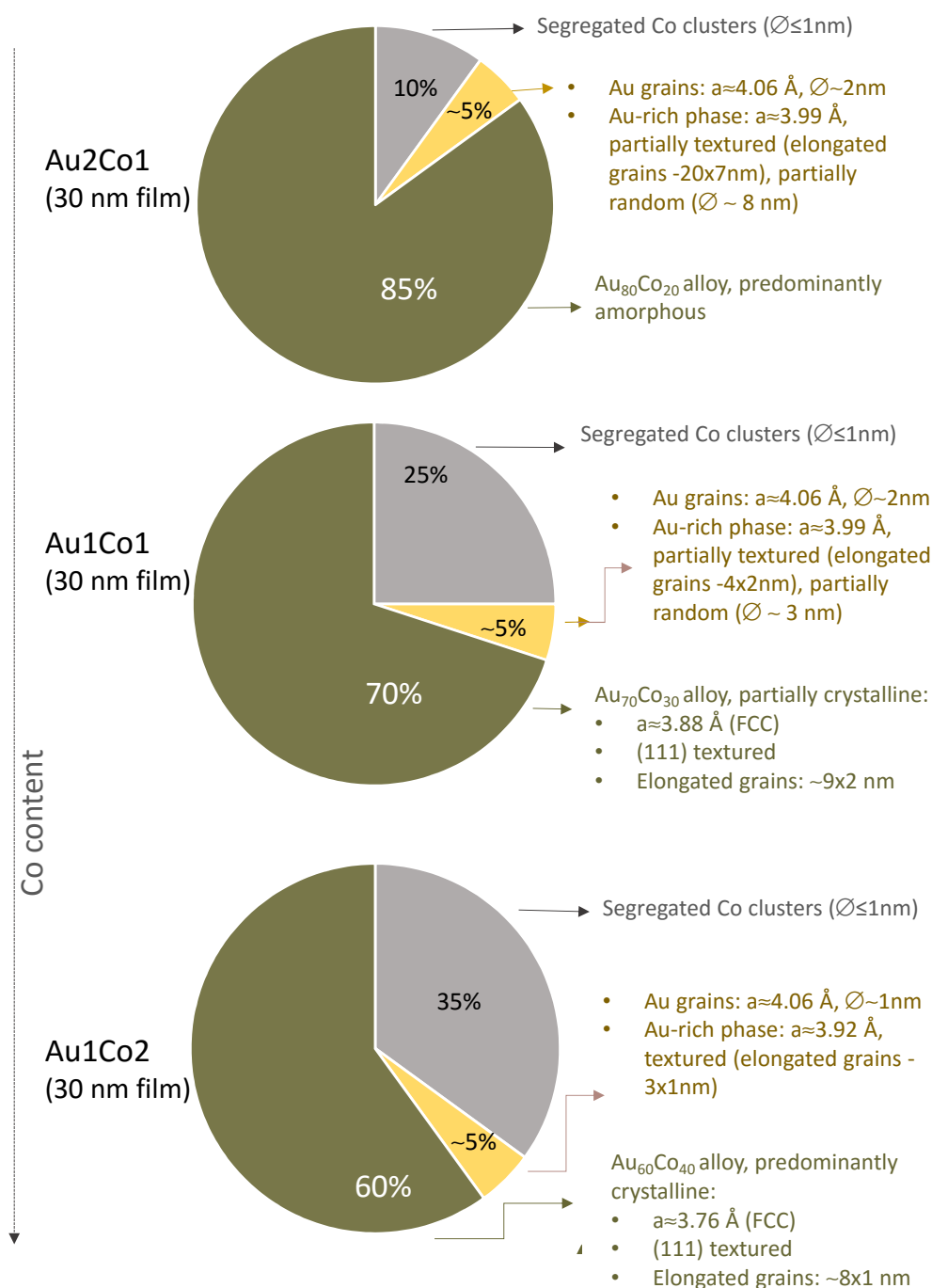
Figure 2.20: A scheme summarizing the main results of the full structural investigation on 30 nm-thick films: Au2Co1 (top), Au1Co1 (center) and Au1Co2 (bottom). The stoichiometry of the alloy and the segregation of Co (nanometric) clusters are highlighted as well as the features of crystalline phases (a is the lattice parameter).

2.5 Structural features vs. film thickness

It has been already pointed out (section 2.3.2) that the phases detected by GI-XRD in the thinnest films, i.e., the 15 nm-thick samples, are comparable within error with those detected in the set characterized by a thickness of 30 nm.

A similar scenario occurs also in the case of the 100 nm-thick films; furthermore, here, due to the higher intensity of the XRD signals, the presence and the role of textured phases, characterized by a shorter lattice parameter, are particularly evident.

Fig. 2.21 a) reports the grazing-incidence XRD scans as a function of the composition, while the corresponding symmetric scans are shown in Fig. 2.21 b).
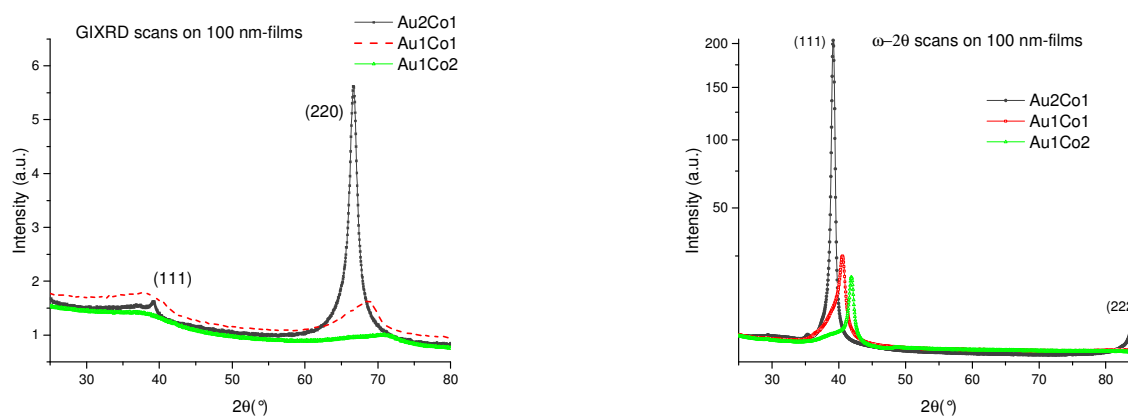
Figure 2.21: On the left, the XRD pattern (grazing incidence geometry) for the 100-nm thick films of different stoichiometry. The corresponding symmetric scans (i.e., $\omega - 2\theta$) are reported on the right.

Similarly to the thinner samples, a FCC phase of lattice constant shorter than that of magnetron sputtered gold is present in all the nanocomposites. This phase is, as usual, highly textured along the growth direction, so that, to detect the (200) reflection (absent in the GI-XRD measurements) it is necessary to properly tilt the samples along the ψ direction of the diffractometer (as seen in Fig. 2.6) and perform the $\omega - 2\theta$ scans around that reflection; the collected patterns are reported in Fig. 2.22.

Fig. 2.23 displays the data of the lattice parameters inferred separately from the (220) reflection (of grazing incidence scan), the (111) peak (in the symmetric scan) and the (200) reflection (measured by a 'tilted' $\omega - 2\theta$ scan). The results confirm, on one hand, that the lattice parameter of the predominant crystalline phase shortens as the Co content increases and, on the other hand, demonstrates that this phase is quite 'isotropic' along the three crystallographic directions.
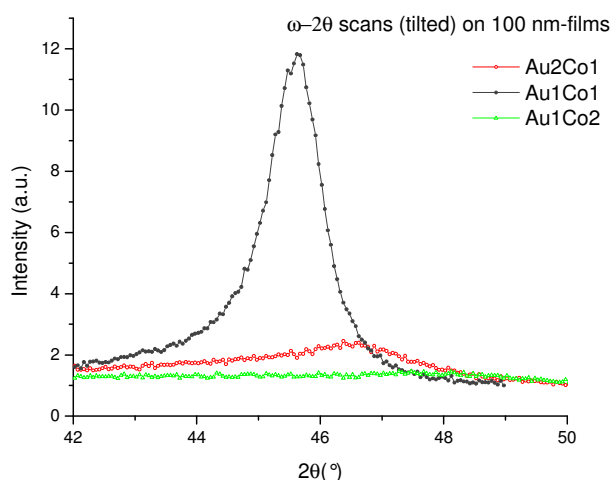
Figure 2.22: XRD data collected by means of a symmetric scans performed around the (200) reflection (i.e., tilting the axis normal to the sample surface in order to set the ψ angle at a value $\approx$ 54.7°).
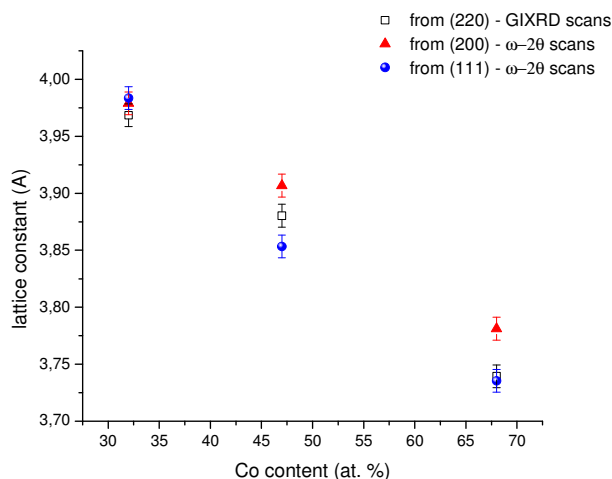
Figure 2.23: Data of the lattice parameters for the crystalline phases detected in the Au:Co 100-nm thick samples, as a function of the Co content (%). The experimental value have been inferred from the principal reflections: the (220) peak in the Grazing-incidence patterns, the (111) peak of the symmetric scans and the (200) reflection in the $\omega - 2\theta$ patterns collected tilting the samples.

In the case of the Au-rich sample, this ′isotropic′ FCC phase has a lattice parameter of 3.97 ± 0.01 Å; the size of the grains, as inferred from GI-XRD scan is about 8-9 nm, while that along the growth direction (as inferred from (111) reflection in $\omega - 2\theta$ scan) is $\approx$ 30 nm. Moreover, the corresponding (111) reflection is well detected also in the GI-XRD scan, revealing that this phase, or at least part of this phase, is randomly distributed in the coating, i.e., some grains have lost the strong preferential texturing.

Concerning the balanced and Co-rich sample, a detailed analysis of the peaks, through the superposition of two pseudo-Voigt functions, is needed. Two examples of this kind of analysis are reported in the following pictures. Fig. 2.24-left- regards the (220) reflection in the grazing incidence scan of Au1Co1 nanocomposite while Fig. 2.24-right- reports on the analysis of the (111) peaks in the $\omega - 2\theta$ scan of sample Au1Co2. According to this
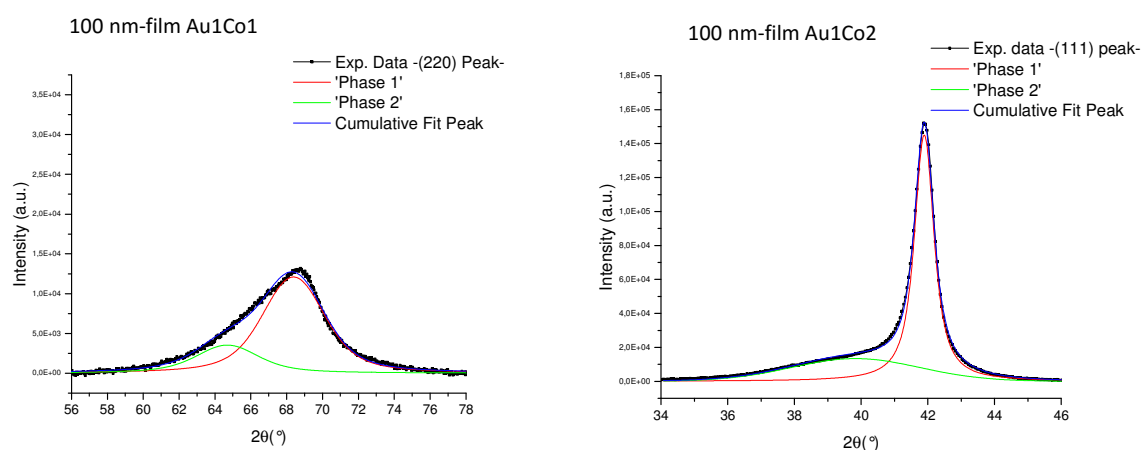
Figure 2.24: Examples of fitting with a double Pseudo-Voigt function: on the left, the case of the (200) peak in the GIXRD pattern of a balanced sample; on the right the contribution to the (111) peak in the symmetric scan of Co-rich sample.

analysis, the highly textured phase in the balanced coating has a lattice constant in the range of 3.84-3.88 Å and it is characterized by elongated nanoparticles whose dimension along the growth direction is about 13-15 nm. Moreover, beside a fine grained (2-3-nm) phase of gold (lattice constant of about 4.07 Å) randomly oriented, there are small particles of an 'intermediate' phase whose lattice parameter is 3.94 ± 0.02 Å and whose (111) planes are preferentially parallel to the substrate. A similar scenario characterizes the Co-rich sample, except that the shrinked phase has a shorter lattice parameter in the range of 3.73-3.76 Å.

It is worth noting that, similarly to the 30 nm-films analysis, the fitting with two functions could be an approximation: the peak tail towards lower angle can be ascribed to a mixture of phases whose features gradually changes from that of the principal phase.

Summarizing, the phases detected with XRD analysis, on 100 nm-thick films, are (where a is the lattice constant):

- Au2Co1: a 'predominant' phase with a of about 3.97 Å, highly (111) texturized with the main size along the growth direction $\approx$ 40 nm and a 'lateral' dimension of about 10

nm; a phase with similar lattice constant, isotropic with average size of about 20 nm and randomly oriented; a fine grained phase (contributing to the XRD intensity to a lesser extent), with a approaching the value 4.06 Å (i.e., 'Au bulk-like phase'), a size along the growth direction $\approx$8 nm and lateral size $\approx$2 nm ;

- Au1Co1: a 'predominant' phase with a=3.85-3.88 Å, highly (111) texturized, main size along the growth direction $\approx$ 15 nm, other dimensions of about 2 nm; some fine-grained phases (average size of about 2-3 nm), with longer lattice constant $\approx$3.94-4.07 Å, partially (111) texturized

- Au1Co2: a phase with a of the order of 3.74 Å, highly (111) texturized, main size along the growth direction $\approx$ 20 nm, other dimensions of about 2 nm; a fine-grained phase (average size of about 1-2 nm) with longer lattice constant $\approx$3.88-3.92 Å, textured, and a fine-grained Au bulk-like phase.

Some interesting features emerge looking carefully at the results from the symmetric scans, which detect the crystalline planes parallel to the sample surface.

It is worth remembering that the predominant contribution to the crystalline portion of the films arises from a highly textured FCC phase, whose (111) planes are parallel to the sample surface.

Fig. 2.25 reports all the collected $\omega - 2\theta$ scans where only the (111) peak of the FCC phase is detected. Fig. 2.25 shows clearly again that in the 30 nm- and 100 nm- thick films this phase is characterized by a shorter lattice parameter with respect to that of gold, which, furthermore, decreases as the Co content increases.

On the contrary, in the case of the thinnest samples, this textured phase has in all the investigated cases a lattice constant of 4.01 $\pm$ 0.01 Å and is quite independent from the stoichiometry of the as deposited sample. Although further investigations are required, this suggests that in the first stages of the film growth an Au-rich phase is formed. Then, as the growth goes on, more cobalt is incorporated in the developing crystalline phase proportionally to the Co content. A steady state is reached, as, when the thickness increases from a value of 30 nm to 100 nm, the phases are the same, i.e., characterized by a similar lattice constant. These phases are composed of columnar grains which, as the film thickness increases, acquire a more isotropic shape.

Furthermore, as suggested by EXAFS analysis, the crystalline phases richer in cobalt induce a higher degree of crystallinity also in the alloyed matrix, which constitute the predominant portion of the films.
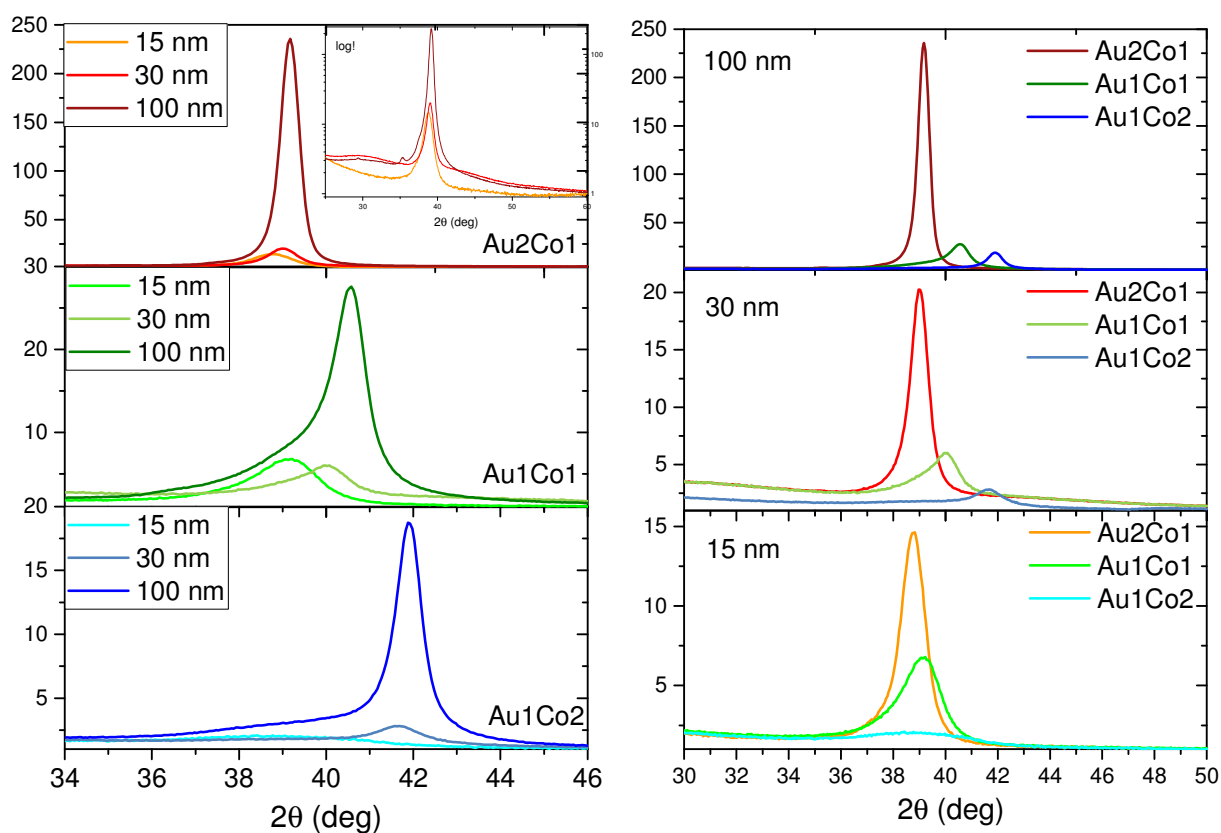
Figure 2.25: A summary of the $\omega - 2\theta$ scans on all the Au:Co films. On the left: given a sample composition, a comparison of the results for films characterized by different thickness. On the left: for each value of thickness, a comparison between the patterns related to different compositions.

3 The Properties of Au:Co films

This Chapter summarizes the functional properties of the Au:Co films with the estimation of the UV-Vis optical constants and the characterization of the magnetic behaviour. X-Ray Magnetic Circular Dichroism measurements demonstrate that Au atoms acquire a magnetic moment, further confirming the alloying with Co.
Finally the results concerning the thermal stability of the Au:Co alloy and films will be presented.

3.1 Optical Properties

The optical properties of the prepared Au-Co materials were firstly characterized by means of ellipsometric measurements performed on 30 nm-nanocomposites (on silica substrates), in the range of 30-1000 nm.

A commercial V-Vase (Woolam) ellipsometer was employed, in reflectance mode (for incidence angles between incoming light and the normal to the surface of 60°-65°-70°) as well as in transmittance mode.

Ellipsometry essentially measures a change in polarization as light reflects from a material structure. The polarization change is represented as an amplitude ratio, Ψ, and the phase difference, Δ. Since the measured response depends on the optical properties and thickness of individual layers, these spectroscopic scans enable, on one hand, the estimation of the material optical constants, i.e., the real part of the refractive index n and the extinction coefficient k, while, on the other hand, allow an indirect evaluation of the structural features through a comparison between experimental and modelled optical data.

The physical quantities Ψ and Δ, experimentally measured by the ellipsometer, are related to the ratio of Fresnel reflection coefficients r_p and r_s for p and s polarized light through the:

$$\rho = \frac{r_p}{r_s} = \tan(\Psi)e^{i\Delta}. \tag{3.1}$$

while r_p and r_s are related to the polarized incident, reflected and transmitted electromagnetic waves according to the Jones′ formalism [77]. Their values, experimentally measured as a function of the wavelength and for the three incidence angles previously mentioned, have been fitted assuming the sample composed by a metallic film on a silica substrate. The fitting parameter are, beside the composition and the thickness of the layers, the optical constants of the constituting material. It is worth noting that a bare silica slide has been measured as well, in order to estimate its actual optical constants and to build a more reliable model. An example of ellipsometric experimental data with the corresponding fitting is depicted in Fig. 3.1
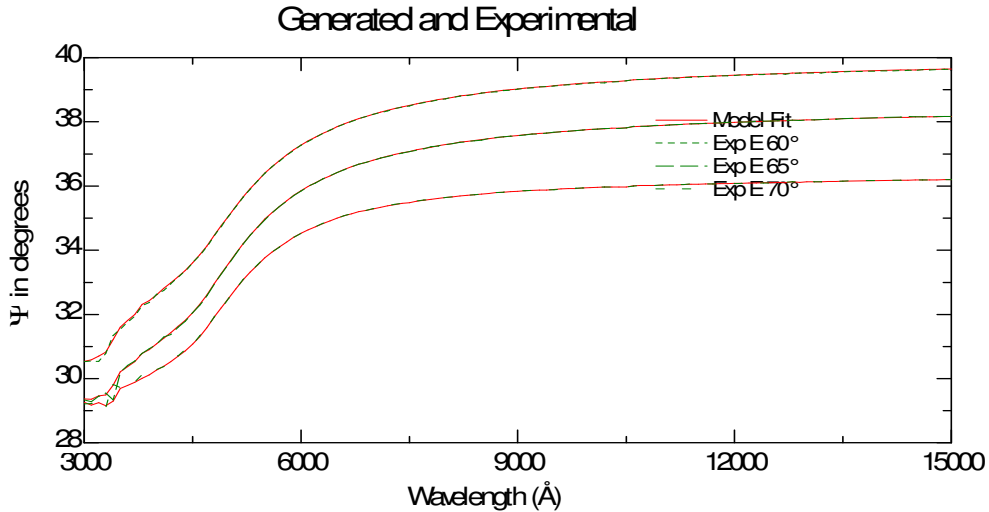
Figure 3.1: A representative set of ellipsometric experimental data (in green) with the corresponding ′generated′ data, i.e., the results of the fitting procedure (in red).

On one hand, the optical constants, n and k, of the Au:Co nanocomposites were in this way inferred for all the stoichiometries. These values were employed to estimate real -ε_1- and imaginary -ε_2- part of the complex dielectric function $\varepsilon = \varepsilon_1 + i\varepsilon_2$, through equations 1.5 and 1.6.

On the other hand, the optical constants have been calculated in the framework of the Effective Medium Approximation (EMA). The EMA models are among the most used in literature for the calculation of the effective optical properties of a mixture of materials [78]. One of them is the Bruggeman model, which is usually adopted to simulate nanocomposites where clusters of the components do not form any compounds but are closely mixed. The 30 nm-films have been modeled with a silica substrate coated with a mixture of cobalt and gold. The atomic percentages of the two metals have been constrained to

the values inferred from RBS measurements, so the 'host' material was alternatively Au or Co depending on the actual film stoichiometry. Moreover, the experimental dielectric functions of the starting metals (ε_{Au} and ε_{Co}), estimated from the fitting of spectroscopic scans performed on pure sputtered Au or Co layers (with thickness in the range of 30-40 nm), was adopted in the calculation of the nanocomposites' optical constants (i.e. ε) through the numerical equation:

$$f_{Au}\frac{\varepsilon_{Au} - \varepsilon}{\varepsilon_{Au} + 2\varepsilon} + f_{Co}\frac{\varepsilon_{Co} - \varepsilon}{\varepsilon_{Co} + 2\varepsilon} = 0 \tag{3.2}$$

where f_{Au} and f_{Co} (=1-f_{Au}) are the fraction of the two constituent metals, ε_{Au} and ε_{Co} are the corresponding dielectric function and ε is the final effective dielectric function of the composite material.

The comparison between the experimental optical constants and those generated from the Bruggeman model, are shown in Fig.3.2, respectively for the Au2Co1 (Fig.3.2 a)-b)), Au1Co1 (Fig.3.2 c)-d)) and Au1Co2 (Fig.3.2 e)-f)) compositions. In all the cases, the experimental values, especially those related to the refractive index, are not in agreement with the corresponding simulations; this indicates that a complete segregation of the constituting metals, as assumed in the model, does not take place in anyone of the analyzed nanocomposites, while it is consistent with a, at least partial, alloying between gold and cobalt.

The real (ε_1) and imaginary (ε_2) part of the complex dielectric constants, estimated form the n and k values, through the equations 1.5 and 1.6, are reported in Fig. 3.3 for all the Au:Co films; the data concerning a 30-nm film of pure sputtered gold are reported as well for comparison.

A reliable evaluation of the complex dielectric constants of the as prepared nanocomposites is, indeed, of paramount importance for the comprehension and the modeling of their plasmonic behavior. As seen in section 1.2.1, the dielectric constant is a key element in the dispersion relation of traveling electromagnetic waves which, in the case of a metal coupled to a dielectric medium, determines the existence and the behavior of the Surface Plasmon Polaritons (or 'extended Plasmons', i.e., as seen in 1.2.1, excitations propagating at the interface and evanescently confined in the perpendicular direction). Moreover, in the case of metal nanoparticles embedded in a dielectric medium (or, conversely, of nanovoids in a metallic matrix), the dielectric constants of both materials tune the resonance conditions
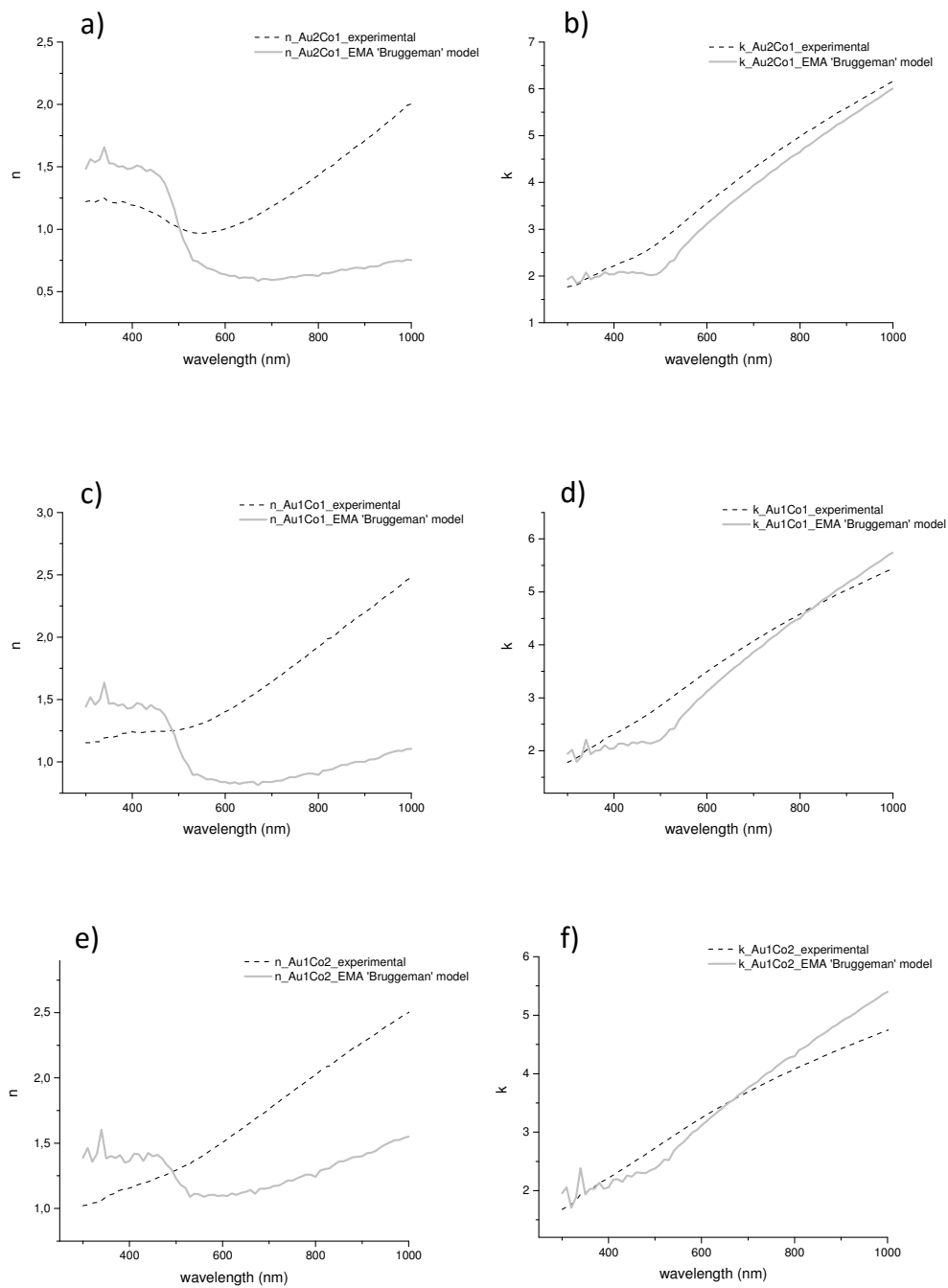
Figure 3.2: The optical constants inferred from the experimental data (black dashed line) are superimposed to that calculated through a EMA-Bruggeman model (gray line). a)-c)-e) refers to n values respectively for the composition Au2Co1, Au1Co1 and Au1Co2. b)-d)-f) refers to k values respectively for the composition Au2Co1, Au1Co1 and Au1Co2

and the dipole surface plasmon modes (i.e., the localized plasmons).

The macroscopic optical behavior of the metallic coatings are controlled by their dielec-
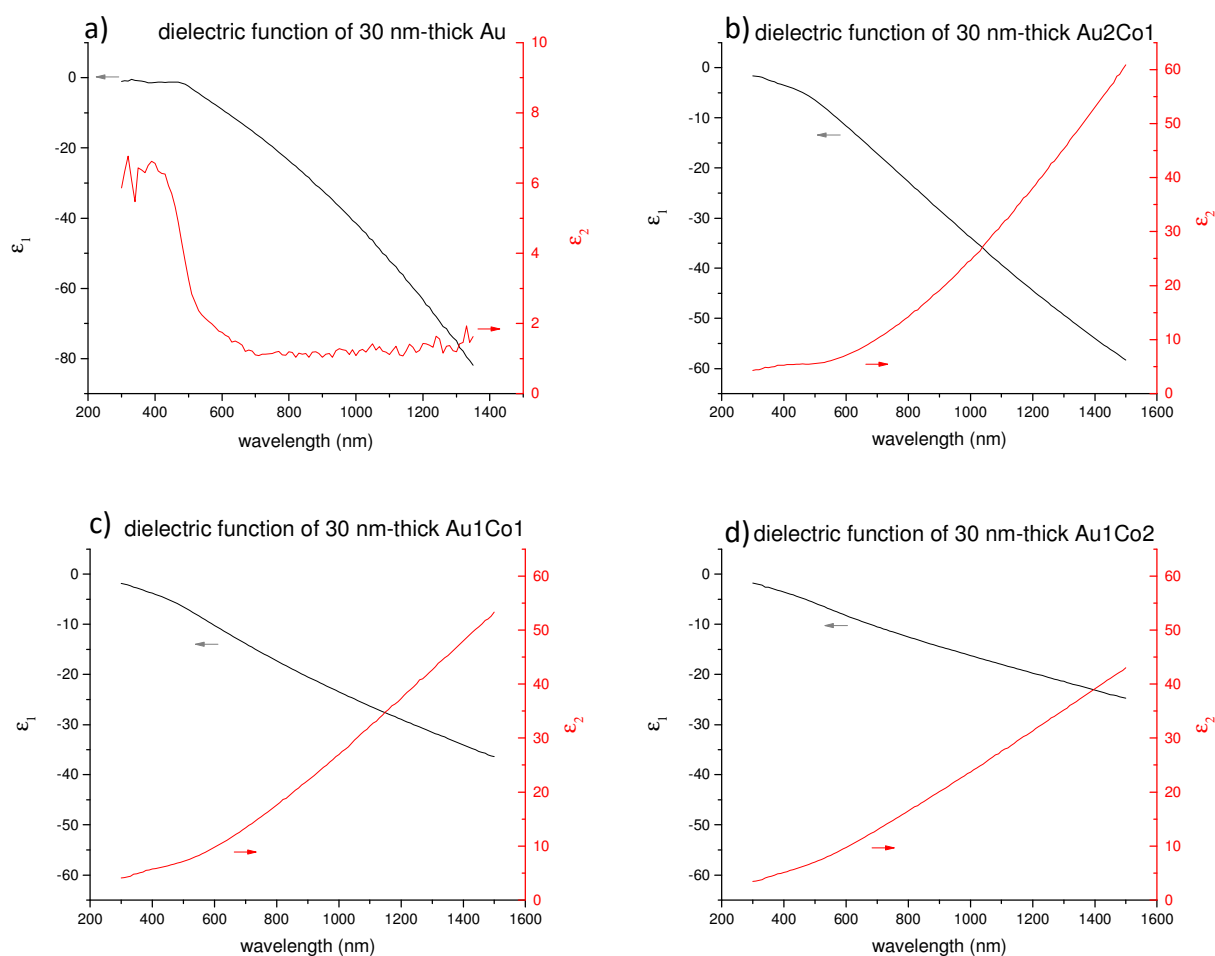
Figure 3.3: Experimental real (ε_1) and imaginary part (ε_2) of the complex dielectric function for 30 nm thick layers: a) Au, b) Au2Co1, c) Au1Co1, d) Au1Co2.

tric constants. The UV-Vis Transmittance data have been acquired with a Jasco V-670 double-beam spectrophotometer, in the 190-1700 nm wavelength range and are reported in Fig. 3.4. The spectrum of a 30-nm film of pure (sputtered) Au is reported in Fig. 3.4 as well for comparison -box on the right-.

A pure noble metal film reflects the electromagnetic radiation for frequencies up to the visible part of the spectrum. At lower wavelengths, the field penetration increases until the UV range, where the dielectric character, generally acquired by the metallic materials, is strongly attenuated by the transitions between electronic bands (inter-band transitions). This leads to the typical transmittance drop for wavelengths below 400 nm. The transmittance of Au:Co films follows the same trend. In this case, for wavelengths in the near IR range, the penetration of the electromagnetic field becomes deeper as the Co content in-
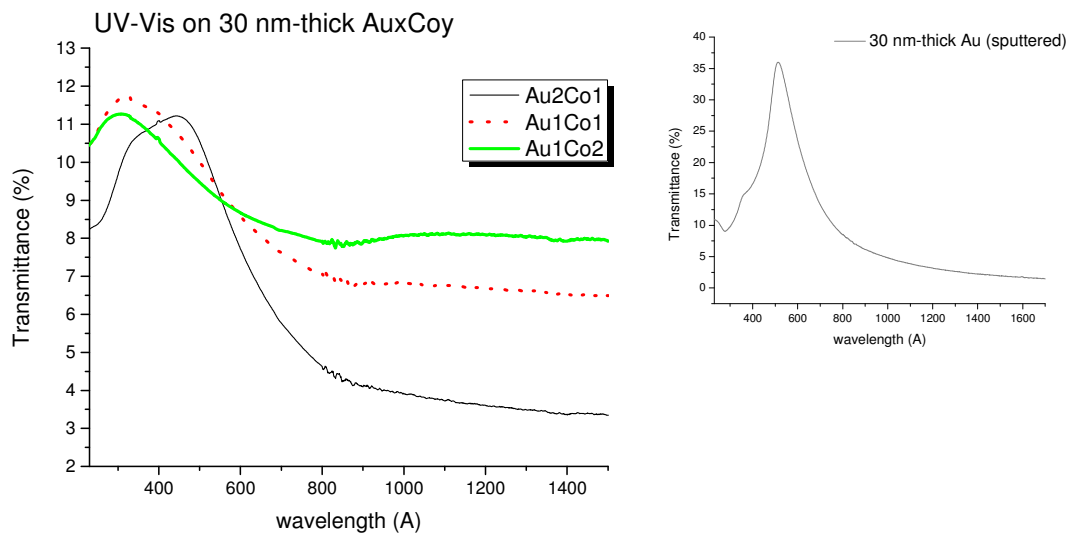
Figure 3.4: Transmittance spectra of Au2Co1, Au1Co1 and Au1Co2 30nm-thick films. On the right, the data for a pure gold film (a 30 nm-thick film, prepared by magnetron sputtering) are reported for reference.

creases, leading to a lower reflectance and to a slightly higher percentage of transmittance.

3.2 Magnetic Properties

3.2.1 X-Ray Magnetic Circular Dichroism

In order to detect the local magnetic moment of the bimetallic components in the alloy, a X-ray Magnetic Circular Dichroism (XMCD) analysis was performed both at ESRF (Grenoble, France) and ELETTRA (Trieste,Italy) Synchrotron. This technique allows decomposing the total magnetic moment of a multicomponent, heteromagnetic system into the orbital and spin contributions of each element; other peculiar features are its element specificity, the orbital selectivity and the high sensitivity.

Basically, the dichroic signal with X-ray wavelengths relies on the different absorption coefficient for different polarization of the radiation: it is induced by magnetism and is significant near the photoelectron absorption edge from a core state.

The physical mechanism underlying the technique is phenomenologically outlined in Fig. 3.5 where the two step-model of Stöhr [8] is depicted.

The angular moment carried by a circularly-polarized X-ray photon (i.e. $+\hbar$ and $-\hbar$ respectively for right and left circularly polarized radiation) is entirely transferred to the electron photo-excited from a core level (through the conservation law of the angular momentum in the absorption process). If the photo-electron originates from a spin-orbit split level, corresponding for example to the L_3 edge depicted in Fig. 3.5(b), part of the angular momentum carried by the photon will be converted into spin via the spin-orbit coupling. Right circularly polarized photons transfer the opposite momentum to the electron than left circular polarized photons, and hence photo-electrons with opposite spin are created in the two cases. Moreover, the spin polarization will be opposite at the two edges, due to the opposite spin-orbit coupling.

The magnetic properties enter in the 'second' step, as the spin splitting of the valence shell acts as a sort of detector for the spin of the excited photo-electron. The dichroic signal is proportional to $\mathbf{k}\cdot\mathbf{M}$, $\mathbf{k}$ being the X-ray wavevector and $\mathbf{M}$ the vector of magnetization which acts as the quantization axis.

A powerful set of sum rules [79] links the spin and orbital momentum separately and quantitatively to the measured intensity A and B, i.e., to the difference of the white line intensities -the XMCD intensities- recorded with right and left circular polarization. In particular the spin moment can be inferred from $A - 2B$ measured intensity, while the $A + B$ dichroic signal allows to determine the orbital contribution to the moment.
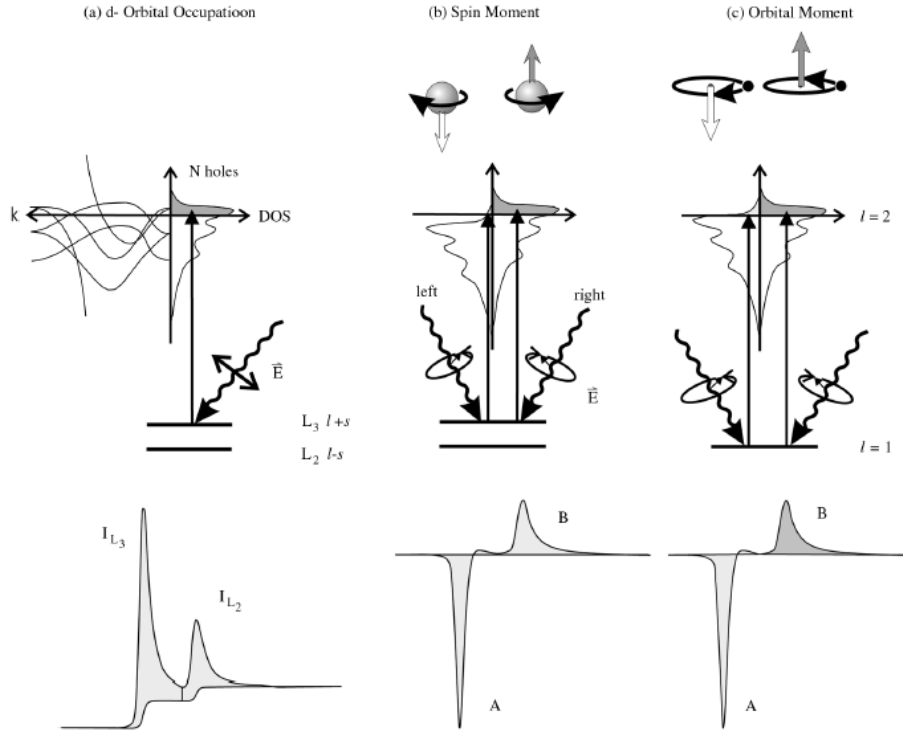
Figure 3.5: A sketch of the one-electron (step) model proposed by Stöhr [8]. In (a) the electronic transitions in conventional L-edge X-ray absorption occur from spin-orbit split $2p$ core shell to the empty conduction band states above the Fermi level. The transition intensity, measured as the white line intensity $I_{L3} + I_{L2}$ is proportional to the number of holes. In (b) and (c) the quantities A and B are the integral of the dichroic signal respectively at the I_{L3} and I_{L2} egdes (see text for details)

.

The experimental XMCD data are generally analyzed according to the formalism of Chen and co. [9]: the relevant quantity p, q and r adopted in the calculation are outlined in Fig. 3.6. The cited work is the first experimental confirmation of the XMCD sum rules for Fe and Co. Starting from the transmission spectra of Fe and Co thin films (on parylene) taken with the projection of the spin of the incident photons parallel (I_+) and antiparallel (I_-) to the spin of the majority electron, the authors employed the corresponding absorption spectra, μ_+ and μ_- (calculated respectively from I_+ and I_- through the equation $\mu_\pm \propto -ln[I_\pm/I_s]$, where I_s is the transmission spectra for the substrate alone), to calculate the relevant integrals. In particular, q is the integrated $\mu_+ - \mu_-$ spectrum in the whole $L_3 + L_2$ range, while p refers to the L_3 edge integral. With only these two calculated quantities, it is possible to infer the orbital-to-spin magnetic moment ratio, $\mu_L/\mu_S = 2q/(9p - 6q)$. Moreover the spin and orbital contribution to the magnetic moment can be quantified separately. The
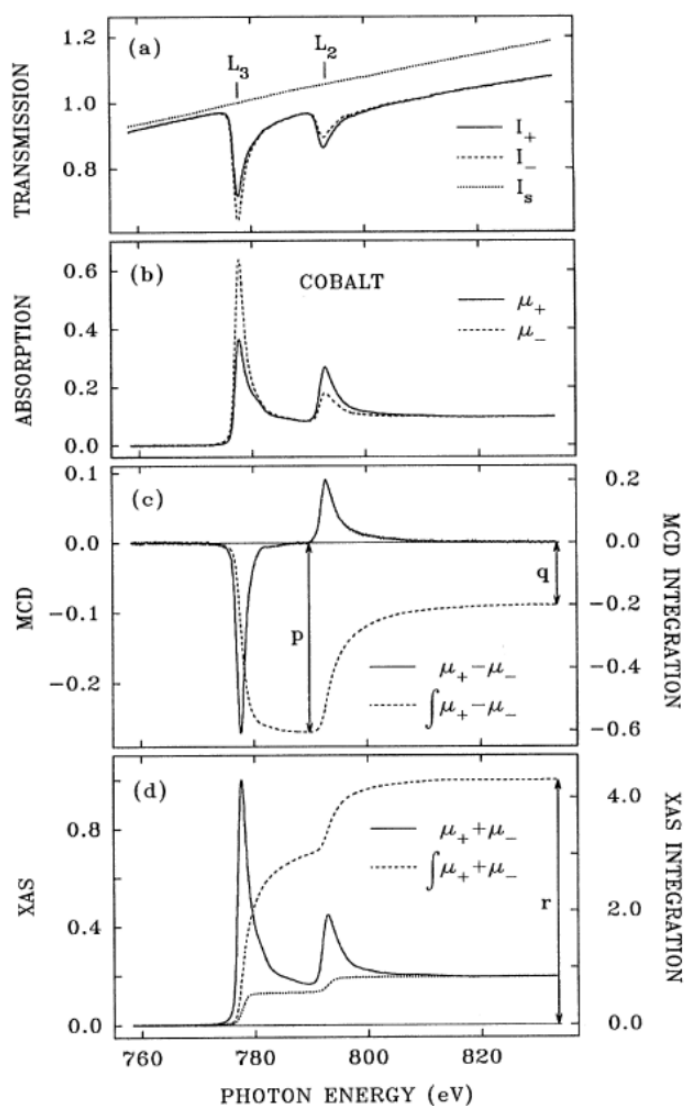
Figure 3.6: X-ray Absorption Spectra and Magnetic Circular dichroism at $L_{2,3}$-edges of cobalt (from [9]). The absorption data in (b) are calculated from the experimental transmission data reported in (a); $+$ and $-$ refers to the incident photon helicity, s refers to the substrate (parylene in this case). (c) and (d) are the MCD (i.e. XMCD) and summed Absorption spectra and their integration. The p and q shown in (c) and the r shown in (d) are the three integrals needed in the sum-rule analysis. The dotted line in (d) is the two-step-like function for edge-jump removal before the integration.

integrated $\mu_+ + \mu_-$ spectrum, calculated in the whole range after a background removal with a twp-steps function, is the third integral need in the calculation, i.e., r. Then, given the estimation of the number of holes in the d orbitals, n_h, the orbital contribution μ_L and

the spin contribution μ_S are calculated through the expression:

$$\mu_L = \frac{-4qn_h}{3r} \tag{3.3}$$

$$\mu_S = \frac{-(6p - 4q)n_h}{r} \tag{3.4}$$

Our XMCD experiment was carried out at Au $L_{2,3}$-edges on balanced and Au-rich samples,
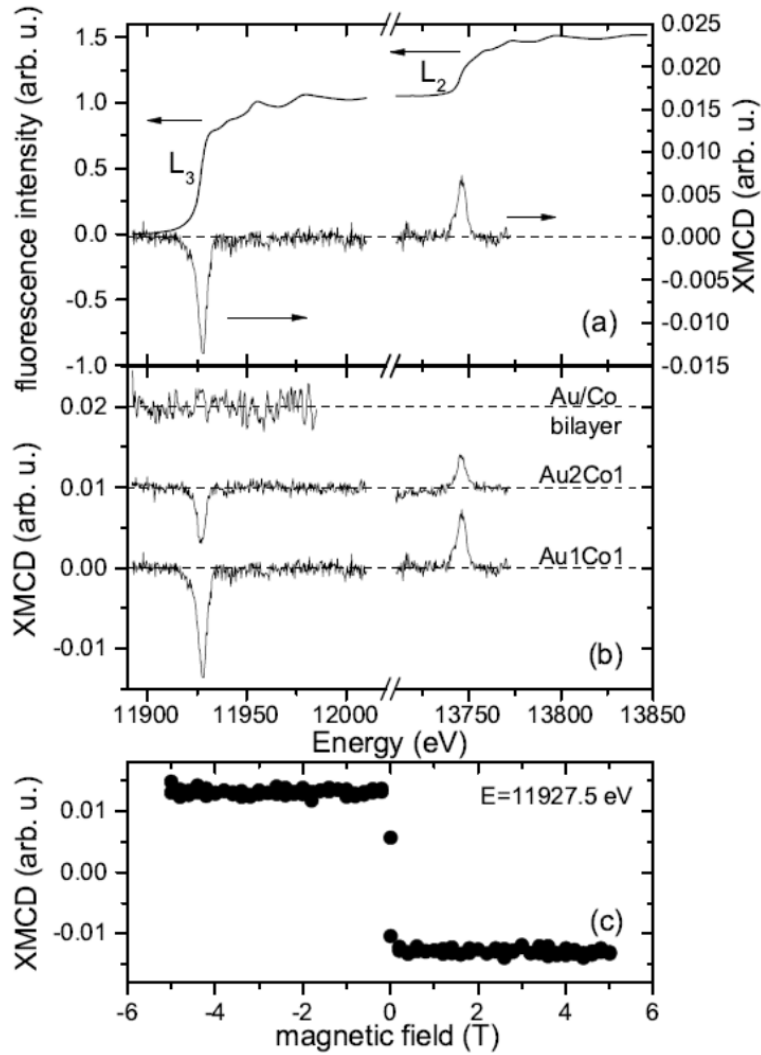
Figure 3.7: (a) X-ray absorption and XMCD spectra recorded at the Au $L_{2,3}$ edges for the Au1Co1 film. (b) Comparison of the XMCD signals for the measured films. (c) XMCD signal measured at E=11927.5 eV (corresponding to the energy where the intensity of the dichroic signal is maximum) for the Au1Co1 film, measured as a function of the applied magnetic field.

at the ID12 beamline of ESRF (Grenoble, France). The Au1Co1 and Au2Co1 samples were

cooled at 2 K and immersed in a magnetic field parallel/antiparallel to the photon beam. The incidence angle with respect to the sample surface was 85 deg. XMCD spectra were recorded in fluorescence mode by a photodiode (backscattering condition) by reversing either the circular polarization helicity or the magnetic field. The hysteresis loops, based on the XMCD signal, were measured by varying the applied magnetic field intensity in the range ± 5 T.

The X-ray absorption and XMCD spectra the Au1Co1 film are reported in Fig. 3.7(a), while in Fig. 3.7(b) the XMCD signal recorded for different films are compared. The XMCD signal is evident for Au1Co1 and Au2Co1 samples, showing that Au atoms in the films have acquired a net magnetic moment due to the Au-co alloying. The sign of the dichroic signal (negative at the L_3-edge and positive at the L_2-edge) indicates that the magnetic moment of Au atoms is aligned along the applied magnetic field. Moreover, a full magnetization of Au is reached for applied magnetic field $|B| \leq 0.2$ T, as shown in the plot reporting the XMCD intensity (at the L_3 edge) as a function of the applied magnetic field (Fig.3.7(c)).

The Au/Co bilayer, measured as well for comparison, does not exhibit any detectable dichroic signal (Fig. 3.7(b)), in agreement with the negligible fraction of Au atoms (with respect to the total number in the film) at the Au/Co interface, as discussed in section 2.3.3. The XMCD signal (i.e., the Au magnetic moment) is higher in the Au1Co1 film with respect to the Au2Co1 one. The reason is likely related to a stronger Au-Co interaction (Co-richer alloy and shorter Au–Co interatomic distance) in the Au1Co1 film (see Table 2.5 and Fig. 2.18). The XMCD signal of the Au1Co1 film (about 1.4% of the edge jump, Fig. 3.7(b)) is comparable to that of Au/Co multilayer [74], despite in our case the Co/Au atomic ratio is significantly lower (about 1:1 with respect to 4:1 in ref. [74]). This indicates a relatively efficient coupling in the alloy film, induced by the high degree of mixing, which is promising for magneto-optical applications. Moreover, the Au XMCD signal in the Au1Co1 film is significantly higher than the one for films of Au-capped Co nanoparticles [80], in agreement with the higher degree of mixing in the present case.

The sum rules, see equations 3.3 and 3.4, were applied to quantitatively estimate the magnetic moment of Au atoms, as well as the spin and orbital contributions to the magnetic moment [74]. The number of holes was assumed to be 0.054 as found in [81] for the compound Au_4Mn. This approximation is widely adopted by the XMCD community. Given the element Au, indeed, n_h depends only on the specific electronic state of well defined

symmetry to be considered.

For the Au1Co1 film the average magnetic moment per Au atom is 0.059 μ_B/atom, μ_B being the *Bohr magneton* ($= 927.401 \times 10^{-26} J/T$). This result is comparable to the one obtained for the Au/Co multilayer; again, since our Co/Au atomic ratio is significantly lower with respect to the multilayer, this is in agreement with an effective alloying between the two metals [74]. Moreover, it is found that the orbital-to-spin magnetic moment ratio is μ_L/μ_S=0.17±0.01 for the Au1Co1 film and μ_L/μ_S=0.14±0.01 for the Au2Co1 one. A higher orbital component is known to arise by decreasing the magnetic domain size, due to the higher fraction of atoms at the domain surface [80, 82]. In this case, the coordination number of the alloy phase (slightly lower for the Au1Co1 film than for the Au2Co1 one) suggests a sub-coordinated site for the Au1Co1 film, that could explain the small difference. For comparison, in the well ordered Au/Co multilayers previously cited μ_L/μ_S=0.12 [74]. To complement the study on the metallic magnetic moment, another XMCD experiment was carried out at the Co $L_{3,2}$ absorption edges at the beamline CiPo of the ELETTRA synchrotron (Trieste, Italy) in transmission mode. The samples were immersed in a magnetic field (maximum intensity = 0.3 T) parallel/antiparallel to the photon direction. A cooling system assured an homogeneous temperature of the sample, which could be varied in the range 20-300 K. The XMCD signal was collected by reversing either the photon helicity or the direction of the magnetic field. The same sum rules discussed before were used to estimate the orbital versus spin contribution to the total magnetic moment as well as the total magnetic moment per Co atom. The experiment was mainly focused on the Au:Co 30 nm thick films deposited onto C-coated Cu grids (grid spacing = 30 μm).

In Fig. 3.8(a) one example of X-ray absorption spectra recorded with opposite values of the magnetic field (B=0.3 T, T=10 K) is shown for the Au1Co1 as-deposited film. The XMCD signals retrieved from the spectra for all the as-deposited layers (T= 10 K) are reported in Figure 3.8 (b). The spectra are normalized to the L_2 dichroic signal.

It is evident that the intensity of the L_3 dichroic signal depends on the film composition indicating a different contribution of the orbital magnetic moment to the total magnetic moment of Co atoms.

In Fig. 3.9 the orbital versus spin magnetic moment ratio is reported for the different films, measured at 10 K and at room temperature. At low temperature, the orbital component of the Co magnetic moment is significantly higher for low Co concentration in the film. For comparison, the μ_L/μ_S values measured for a pure Co film is 0.1 [9] while for Co clusters
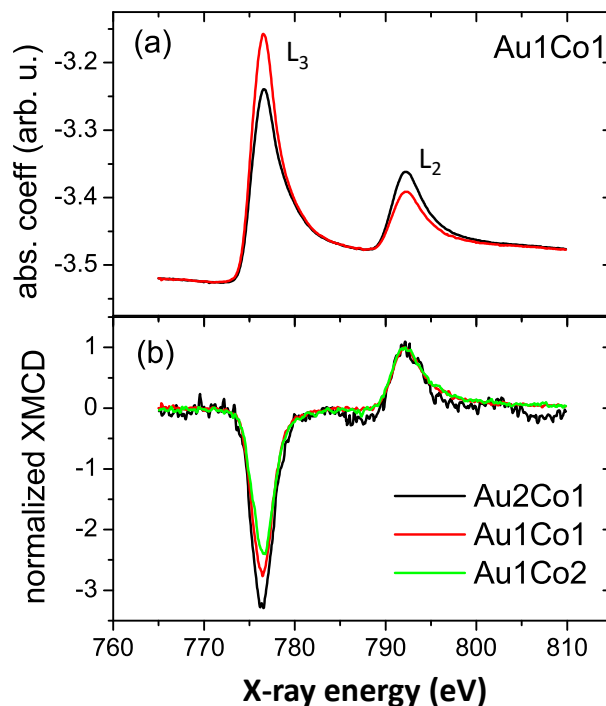
Figure 3.8: (a) Co $L_{2,3}$ edge X-ray absorption spectra for the Au1Co1 film, measured at T=10 K with the magnetic field parallel and antiparallel to the photon helicity.(b) Normalized XMCD signals for the three films of different composition, measured at 10 K.

immersed in a Au layer (i.e., complete phase separation) is about 0.2 [80]. For Au-Co alloy films the results are intermediate between these two values. Nevertheless, it is observed that the experiment at room temperature shows a more modest dependence of μ_L/μ_S on the film composition. Work is in progress to clarify this point. The results on μ_L vs. μ_S and on the measured magnetic moment per Co atom for the different films are reported in Fig. 3.9. The results indicates that the total magnetic moment of Co does not depend appreciably on the film composition.

It is worth noting that the maximum value of the magnetic field use was 3000 Gauss and that it was applied perpendicular to the sample. In these conditions the Au:Co films could not reach the saturation magnetization, as demonstrated by a representative hysteresis loop reported in Fig. 3.10. For this reason, the estimated values of the magnetic moment are underestimated with respect to the actual values, obtained by the SQUID magnetometry, which will be described in the next section.
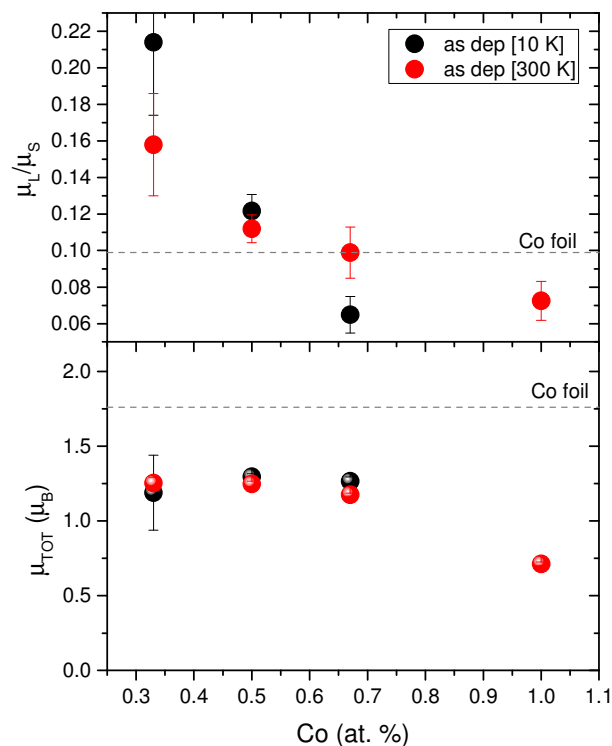
Figure 3.9: Top: Co $L_{2,3}$ edge X-ray absorption spectra for the Au1Co1 film, measured at T=10 K with the magnetic field parallel and antiparallel to the photon helicity. Bottom: Normalized XMCD signals for the three films of different composition, measured at 10 K.
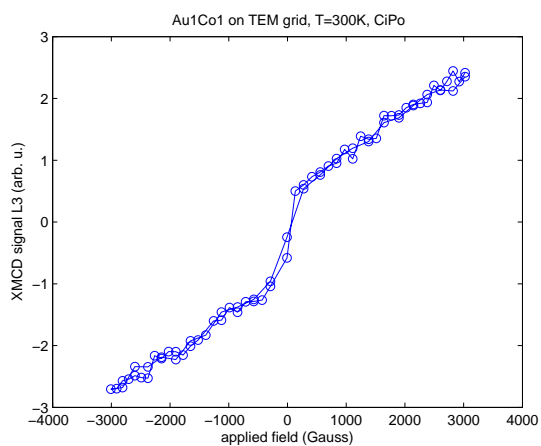
Figure 3.10: Hysteresis loop for the Au1Co1 film (on grid) acquired at 300 K.

3.2.2 SQUID measurements

The magnetic properties of the Au:Co films have been studied by measuring hysteresis loops in the 6-300 K range with a Superconducting Quantum Interference Device (SQUID) magnetometer. The thickness of the films is 30 ± 2 nm. A Co film, with thickness 22 ± 1 nm, was also investigated as reference sample.

SQUID is the main component of the quantum design Magnetic Property Measurement System (MPMS) that is recognized to be one of the most sensitive instrument for measuring magnetic properties; the intensity of the applied magnetic field, that is produced by a superconducting magnet made of wires wound in a solenoidal configuration, varies in the $0 - 5$ T range, and the sample temperature can be varied in the 2 K $- 400$ K temperature range. The employed SQUID magnetometer is equipped with the reciprocating sample oscillation (RSO) option, that allows to directly determine the overall magnetic moment of a sample with a sensitivity of the order of 10^{-8} emu. The SQUID sensor is based on the physical phenomena of flux quantization through a circuit including a Josephson tunneling junction, where two superconducting electrodes are separated by a thin ($\approx$ nm) insulating barrier. The sensor is connected to the detection coils in a closed superconducting loop. The magnetic moment of the sample, which moves through the superconducting detection coils, induces a change in the magnetic flux; this change is proportional to the persistent current in the detection circuit, which is linearly converted in output voltage by the SQUID sensor. This voltage is, indeed, proportional to the magnetic moment of the sample. A refrigeration by cold helium gas guarantees that the sample, the magnet and the SQUID electronic are in the superconducting state.

The measured loops have been corrected for the diamagnetic contribution of the substrate (Silicon).

The values of M_S at T = 6 K are reported in Table 3.1. In the reference Co film, M_S is

Sample	M_S at T=6K (emu/cm^3)	M_S at T=300K (emu/cm^3)
Au2Co1	325±20	232±17
Au1Co1	490±30	450±30
Au1Co2	710±50	680±50
Co	1250±70	1270±70

Table 3.1: Values of M_S concerning the 30 nm-thick Au:Co films, estimated at T=6K and T=300K (the main source of error on the values is the uncertainty on the sample volume).

lower than the value expected for bulk HCP Co (1422 emu/cm^3). This magnetization reduction may be ascribed to the nanocrystalline structure of the film, implying the presence of a large fraction of atoms located at the grain boundaries and hence a reduced atomic density [83–85]. In the case of the Au:Co films, M_S increases almost linearly with the Co content, as shown in Fig. 3.11.

In Fig. 3.12 the values of M_S for the Au1Co2, Au1Co1, Au2Co1 has been plotted as a
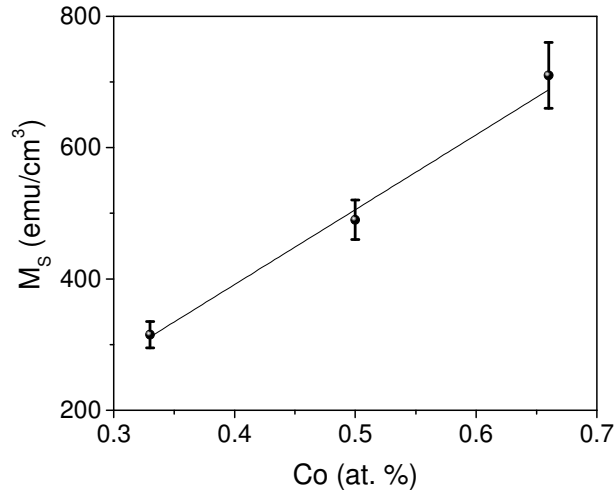
Figure 3.11: Values of M_S at T=6K for the Au:Co films as a function of the Co content in the as deposited samples.

function of temperature T (the curves are normalized to the value of M_S at T = 20 K). The dependence of the magnetization on temperature becomes more pronounced with decreasing the Co content and in particular, in the Au2Co1 film the reduction of M_S is larger than 25%. This decrease can be attributed to the reduction of the crystallinity degree of the samples [86]. As seen in section 2.4, the Au-Co alloy in the Au-rich film is predominantly amorphous. It is worth noting that M_S does not change significantly in the Co film in this temperature range; see Table 3.1 for the values of M_S at T = 300 K.

From the above values of M_S, taking into account the Co integrated concentrations (at/cm^2) measured by RBS analysis and the thickness of Au:Co layers, the values of the magnetic moment (μ) per atom of cobalt have been estimated. The results demonstrate that μ in the different films is quite independent from the composition of the films with a typical value of 1.50 ± 0.02 μ_B/atom. It is worth noting that the values of Co magnetic moment estimated from XMCD analysis (see section 3.2.1 and Fig. 3.9) are lower, around 1.25 ± 0.05. Although further investigation is needed to clarify this point, it is worth remembering that
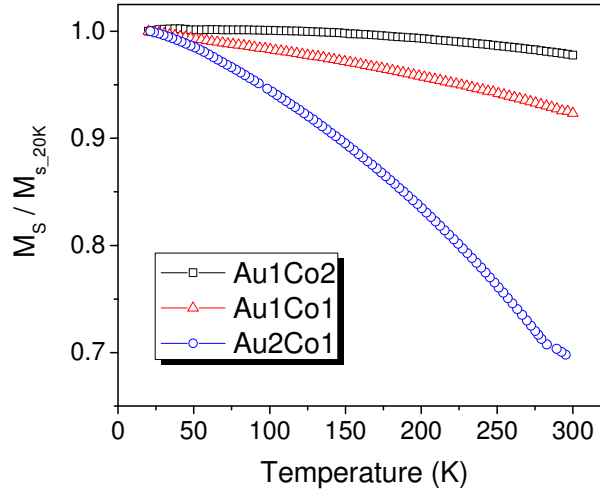
Figure 3.12: Values of M_S (normalized to the value of M_S at T=20K) for the three compositions as a function of temperature.

the Au:Co samples could not reach the saturation magnetization at the maximum allowed magnetic field applied during XMCD experiment. Moreover, the easy magnetization axis of thin films typically lies in the plane parallel to the surface (due to the shape anisotropy) while the applied field was in the XMCD case perpendicular to the sample.

The structural analysis has also pointed out that besides an Au-Co alloy, which is the major constituent of the films showing a composition depending on the initial stoichiometry, there are nanostructured clusters of segregated cobalt. The composition of the alloy and the estimated fraction of each component were schematized in Fig. **??**. Based on this picture, i.e., assuming that the alloy and the segregated cobalt are the only magnetic phases, and considering the values of M_S at 6 K, consistent values of magnetization for the Au-Co alloys have been derived. To the latter phase, we have attributed the M_S measured in the reference Co film. The calculated values of M_S for the Au-Co alloys are reported as a function of the Co atomic content in Fig. 3.13.

A closer inspection of the hysteresis loops provides information about the magnetic structure of the samples.

At T = 6 K, the reference magnetic sample, i.e, the film of pure cobalt, is isotropic in the plane, as observed by measuring hysteresis loops along two orthogonal directions (0° and 90°) in the plane of the film. The loops are reported in Fig. 3.14 which actually shows the ratio between Magnetization (M) and M_S as a function of the applied field (H). In Fig. 3.14 the Coercitivity (H_c) and the Remanent Magnetization (M_r) are shown as functions
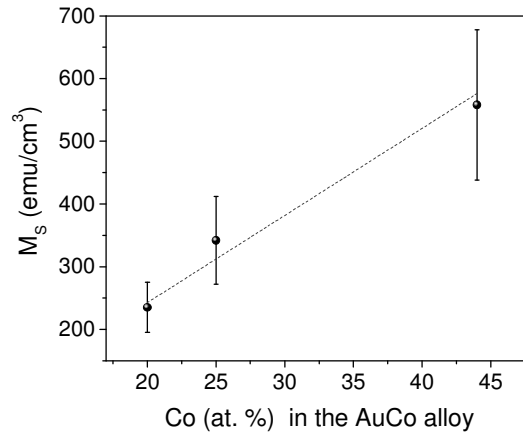
Figure 3.13: Estimated values of M_S for the Au-Co alloy as a function of the Co content in the alloy. Two magnetic phases have been considered i.e., the alloyed compound and the segregated cobalt, according to the scheme sketched in Fig. 2.18 and to Fig. **??**. The line is a linear fit.
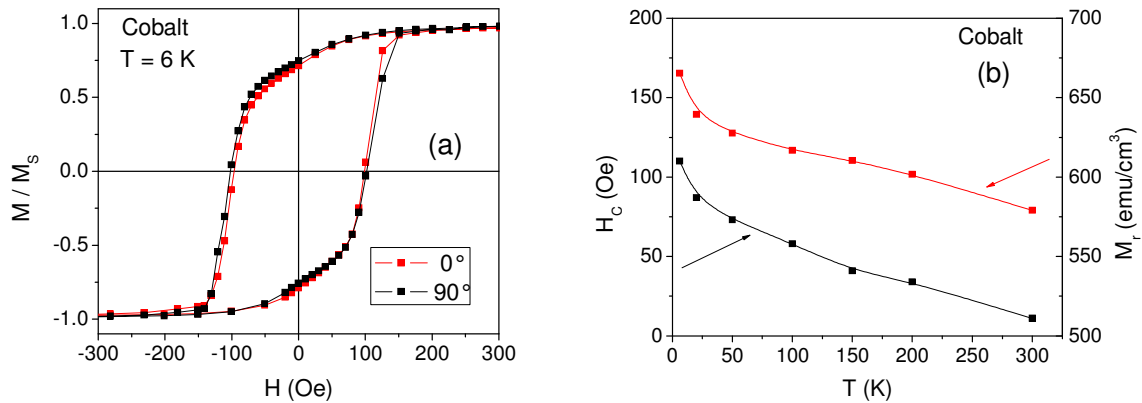
Figure 3.14: Hysteresis loops (in plane, along the two orthogonal directions 0° and 90°) of the reference Co sample, at T=6K. In (a), M/M_S as a function of the applied field (H). In (b), H_c (in black) and M_r (in red) as functions of the temperature (T).

of temperature.

Concerning the alloyed samples, let's consider first the Au2Co1 sample. The loops measured at 0° and 90° at T = 6 K are shown in Fig. 3.15-(a). Also in this case, the sample appears isotropic in the plane. However, a full view of the loops reveals a clear non-saturation tendency. For instance, this effect is well visible in Fig. 3.15-(b) where the first quadrant of the M vs H loop at T = 300 K is plotted.

H_c and M_r for this sample are shown as functions of temperature in Fig. 3.16-(a). At the lowest temperature, H_c is substantially higher than in Co film, but it strongly decreases with increasing temperature especially up to about 100 K; M_r exhibits a similar trend.
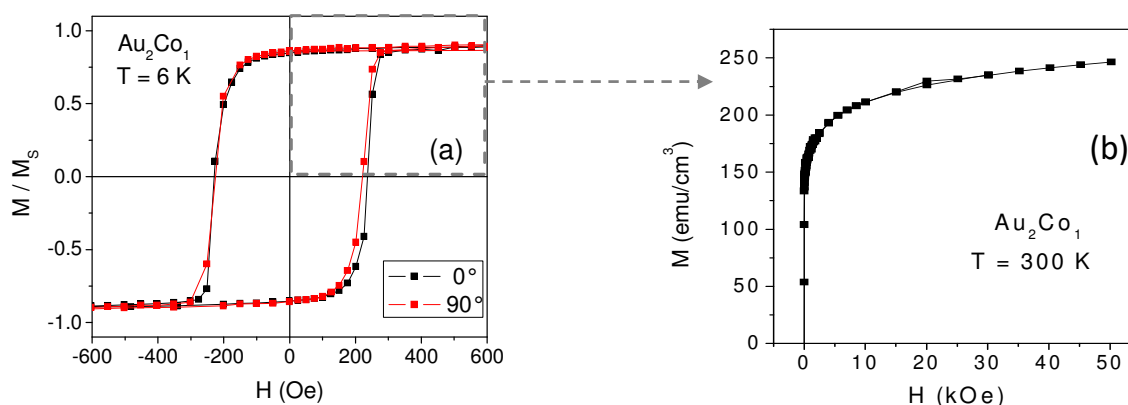
Figure 3.15: In (a), hysteresis loops (in plane, along the two orthogonal directions 0° and 90°) of the Au2Co1 film, at T=6K. The data of M/M_S as a function of the applied field (H) are reported. In (b), first quadrant of the M vs H loop at T = 300 K is highlighted.
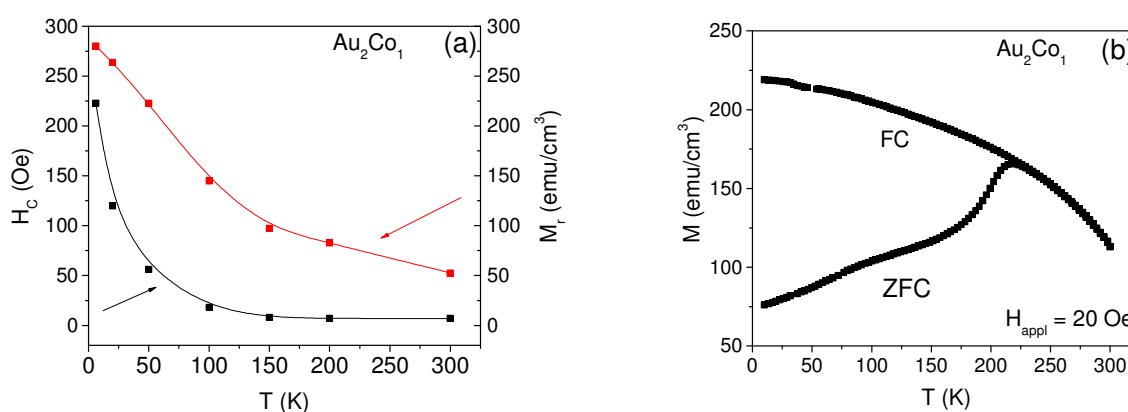
Figure 3.16: In (a), H_c and M for the Au2Co1 film as functions of temperature (T). In (b), the ZFC-FC curve for the Au1Co2 sample. The field applied for the measurements was H_{appl}=20 Oe.

This behavior suggests that small cobalt or cobalt-rich clusters are embedded within the $Au_{80}Co_{20}$ amorphous alloy. The latter constitutes the largest portion of the sample and possesses a weaker ferromagnetism compared to Co. It is expected that the small Co clusters may undergo a magnetic relaxation process similar to superparamagnetism [87,88]. To support this description, the magnetization has been measured for increasing temperature in the 6-300 K range in an applied field H_{appl} = 20 Oe, after cooling the sample from room temperature down to 6 K both without external field (Zero-Field-Cooling (ZFC)) and in H_{appl} (Field-Cooling (FC)). The resulting ZFC-FC curve is shown in Fig.3.16-(a). Magnetic irreversibility, i.e., the difference between FC and ZFC magnetization, is clearly observed from T = 10 K up to T ≈ 215 K, where the ZFC branch displays a peak. This behavior is perfectly consistent with the hypothesis above, namely with the existence of

Co, or Co-rich, clusters embedded in the $Au_{80}Co_{20}$ matrix. The clusters are magnetically blocked at the lowest temperature, thus determining the high H_C value; with increasing T, thermal effects induce magnetic relaxation processes and at $T \approx 215$ K all the clusters have entered the superparamagnetic regime. However, it is worth noting important features of the curve in Fig.3.16-(b): i) the value of M_{ZFC} at T = 6 K is quite high, corresponding to more than 20% of the total M_S measured in this sample (≈ 325 emu/cm^3, see Table 3.1); ii) the value of M_{FC} at T = 6 K corresponds to $\approx 70\%$ of the total M_S; iii) in the whole temperature range, the FC branch exhibits a downward concavity, consistent with the existence of a monotonically decreasing ferromagnetic background.

Furthermore, it should be noted that the Au-Co alloy is magnetically very soft. The contribution of the Co clusters to the H_c, indeed, reduces with increasing temperature as they become superparamagnetic and above T = 100 K values of coercitivity smaller than 10 Oe are measured (see Fig.3.16-(a)). Thus, we conclude that H_{appl} applied at the beginning of the ZFC measurement is sufficient to magnetize the soft Au-Co alloy to a large extent and, after FC, to block along its direction the magnetic moments of the largest fraction of cobalt atoms in the sample.

Considering now the sample with the highest Co content, i.e, the Au1Co2 film, the magnetic behavior is clearly anisotropic. Fig. 3.17-(a) reports the loops measured at T = 10 K along two perpendicular axis in the film plane: the first one parallel to an edge of the sample taken as reference and named as '0°' and the second one perpendicular to the former, labeled '90°'. The anisotropy is evident, being the 0° direction the easy magnetization axis. Indeed, the loop measured at 0° is highly squared (the squareness ratio parameter $M_r/M_S \approx 0.97$) and an abrupt reversal of the magnetization is observed. Accordingly, the 90° direction is expected to be the hard magnetization axis, resulting in the absence of magnetic hysteresis, according to the well-known Stoner-Wohlfarth model for magnetization reversal [89]. On the contrary, we do observe a hysteresis loop with low squareness ratio ($M_r/M_S \approx 0.43$) and slightly shifted along the horizontal axis. In general, a loop shift is the manifestation of the occurence of exchange anisotropy caused by the magnetic exchange interaction at the interface between two phases with different magnetic anisotropy [90–92]. In our opinion, also in the present case, the loop shift, together with the overall irregular shape of the loop, reveals the existence of two different and interacting magnetic phases. With increasing temperature, the shape of the loops evolves as displayed in Figs. 3.17-(b) and 3.17-(c), relative to T = 20 K and T = 100 K respectively. Fig. 3.18 shows the

curves of H_c and M_r/M_S as a function of the temperature, measured along the 0° and 90° directions. At all temperatures, the 0° direction remains the easy magnetization axis. The shape of the 90° loops exhibits a peculiar evolution: at T = 20 K the loop is symmetric with respect to the vertical axis and no shift is observed. However, an odd feature appears, namely a crossing of the two branches. The effect, well visible in Fig. 3.17-(c), affects all the 90° loops measured at T $\geq$20 K and it is highly reproducible.
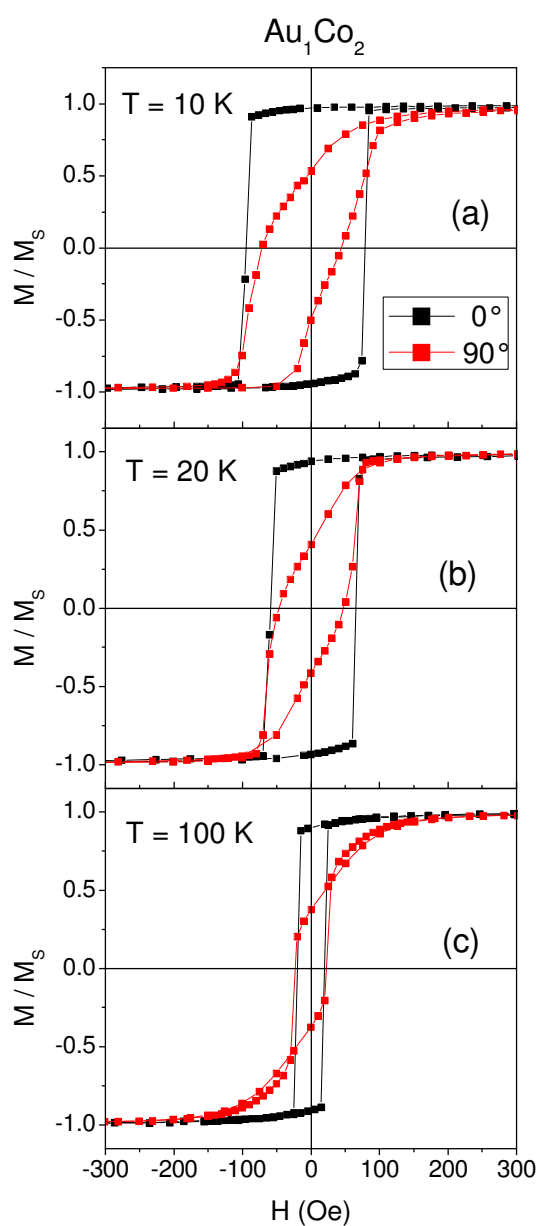
Figure 3.17: The hysteresis loops for the Au1Co2 film, collected respectively at (a) 10K, (b) 20 K and (c) 100 K.
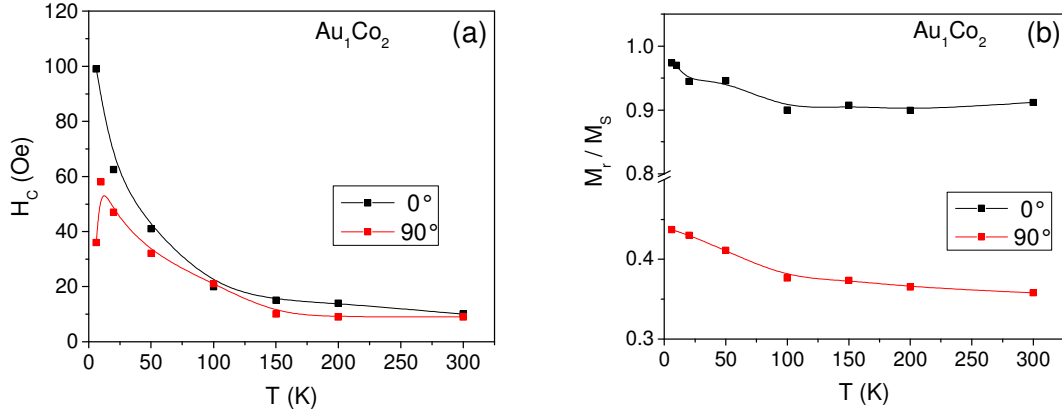
Figure 3.18: Values of H_c (a) and M_r/M_S (b) for the Au1Co2 film as functions of temperature (T). The measurements were acquired along the '0°' and '90°' axis in the plane of the sample.

The Au1Co1 film shows a very similar behavior, as demonstrated by Fig. 3.19 - which displays the loops at 0° and 90° measured at T = 6 K (Fig. 3.19-(a)) and 100 K (see 3.19-(a)) – and by Fig. 3.20, showing H_c and M_r/M_S as functions of the temperature. In this case too, the 0 direction is the easy magnetization axis, even if the squareness ratio is slightly lower than in Au1Co2 at all temperatures, and the 90° loops measured at T < 20 K appear shifted, whereas for T > 20 K they feature crossed branches.

Our hypothesis is that both the loop shift and the branch crossing are hints of the co-existence of two different magnetic phases, even if the second effect is very peculiar and certainly deserves further investigation. Assuming that the two phases are intimately mixed and coupled by exchange interaction, the reversal of their magnetization vectors is determined by the subtle interplay between the strength of the exchange coupling, the strength and direction of the magnetic anisotropy and the direction of the external applied field. These two different magnetic phases may be consistently identified with the Au-Co alloy and with the clusters of cobalt: it is observed that their magnetization vectors switch almost coherently when the external field is applied along the 0° direction, whereas in the loops measured along the 90° direction, a more complicated reversal mechanism occurs, which is still under investigation.

Certainly the Au1Co2 and Au1Co1 films show an anisotropic magnetic behavior. Considering that cobalt is a magnetostrictive material and that the Au-Co alloy may exhibit similar properties, this result is explained assuming a dominant magnetoelastic contribution to the anisotropy energy of the two phases. This requires that the two phases are
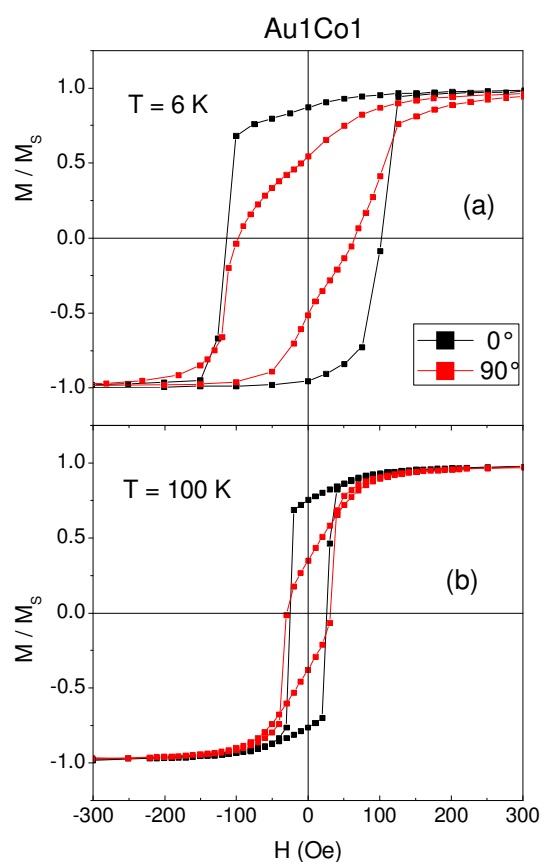
Figure 3.19: The hysteresis loops for the Au1Co1 film, collected respectively at (a) 6K and (b) 100 K.
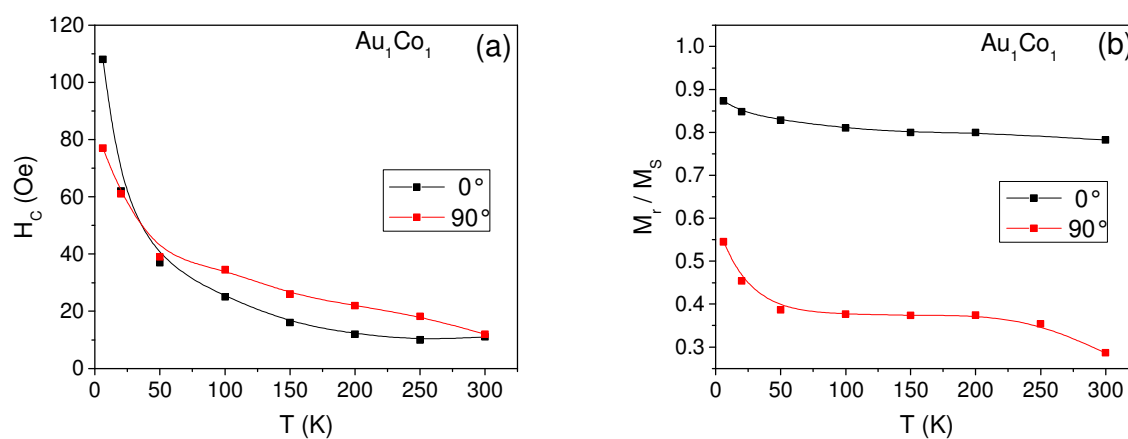
Figure 3.20: Values of H_c (a) and M_r/M_S (b) for the Au1Co1 film as functions of temperature (T). The measurements were acquired along the '0°' and '90°' axis in the plane of the sample.

subjected to a mechanical stress whose origin may be intrinsic to the growth process, as sputtering deposition takes place in out-of-equilibrium conditions, or caused by a lattice mismatch between the two phases themselves. This latter mechanism is in agreement with

the results from the full structural investigation (see section 2.4), as the crystalline properties of the alloy become higher as the Co content (in the as deposited film) increases. On the contrary, it has been demonstrated that the alloy in the Au2Co1 film is mostly amorphous, in agreement with the observed isotropic magnetic behavior.

3.3 Thermal stability of Au:Co films and alloy

To study the stability of the alloy and the evolution of our compounds as a function of the temperature, the Au2Co1 coating was characterized throughout a thermal annealing up to 800°C, performed *in-situ* at the diffractometer. The sample was mounted on a DHS Anton Paar hot stage, connected to a TCU 150 Temperature Control Unit with a nominal heating rate of 60 °C/min. It is composed of a dedicated sample-holder (aluminum nitride material), indicated by the number '2' in Fig. 3.21-left, connected to a heater and isolated from the environment by means of a plastic cover (i.e., the X-Ray window dome indicated by the number '3' in Fig. 3.21) inside which nitrogen gas was fluxed. In order to prevent all possible mechanisms of oxidation, the film was coated with a cap layer of 200 nm of silica.

The heating ramp adopted in this experiment is sketched in Fig. 3.21-right. The heating power furnished to the sample-holder allowed reaching the desired temperature in maximum 10'; an interval of further 10' was dedicated to the thermalisation of the coating.
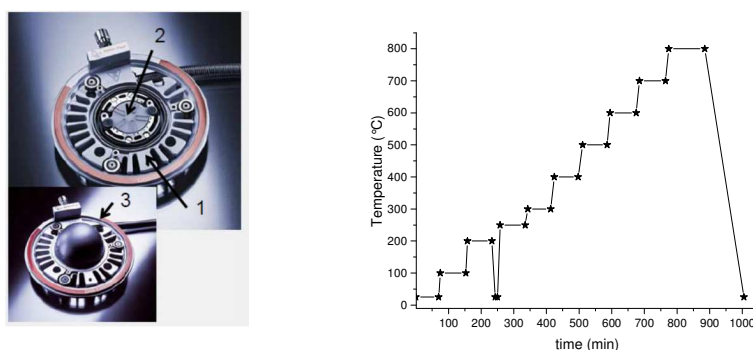
Figure 3.21: Left: the heating stage adopted to perform *in situ* XRD measurements, where '1' is the air-cooled housing, '2' is the heated sample holder, '3' is the X-Ray window dome. Right: the heating ramp applied to the sample-holder during *in situ* XRD experiment.

XRD measurements in GI-XRD geometry have been collected together with symmetric scans, as detailed in 2.3.1. The GI-XRD patterns corresponding to each annealing step are reported in Fig. 3.22.

The reflections are almost unvaried until 200°C, then a transformation starts to occur leading to the shift of the peaks towards lower angles. Moreover the (220) peak experiences a broadening until 300 °C, then a progressive decrease of the signal takes place, indicating that initial strong texture, characterizing the as deposited film, is gradually lost. The final pattern, indeed, reveals a mixture of pure FCC gold and of pure FCC cobalt. This is partic-
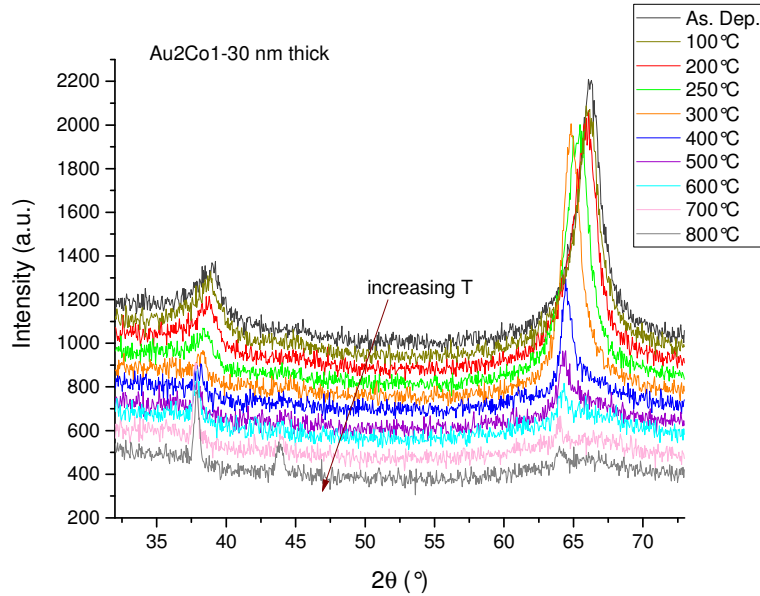
Figure 3.22: GI-XRD patterns collected during the *in situ* thermal treatment, as a function of the temperature.

ularly clear analyzing the data collected on the sample cooled down to Room Temperature, after the complete thermal treatment. Here, differently to the scans acquired during the annealing steps, the reflections do not experience the shift related to the thermal expansion of the lattice. The pattern is reported in Fig. 3.23, compared with the reflections of pure FCC Au and Co.

It is worth noting, that the texture is slightly different from that of bulk gold [64], and resembles that of sputtered Au whose experimental pattern is reported in Fig. 2.4. Furthermore, the appearance of a FCC phase of cobalt is already known in the literature and typically occurs when Co grows in presence of, also small, quantity of Au [3].

Concurrently, the (111) reflection in the symmetric scans strongly increases as demonstrated by the $\omega - 2\theta$ scans reported in Fig. 3.24 as a function of the temperature.

In the low temperature steps, the intensity of the peaks arises from two contributing phases, similarly to what seen in section 2.3.1: a 'secondary' contribution from a Au-like phase (see 'Peak 2' in Fig. 3.25-left) is mixed with a 'predominant' contribution from a phase (see 'Peak 1' in Fig. 3.25-left) characterized by a shorter lattice parameter. The lattice constants of these crystalline phases moves towards higher values as the temperature increases. The data are reported in Fig. 3.24-right and indicate that the two phases merge around 500°C leading to a single phase of bulk Au. The corresponding lattice parameter
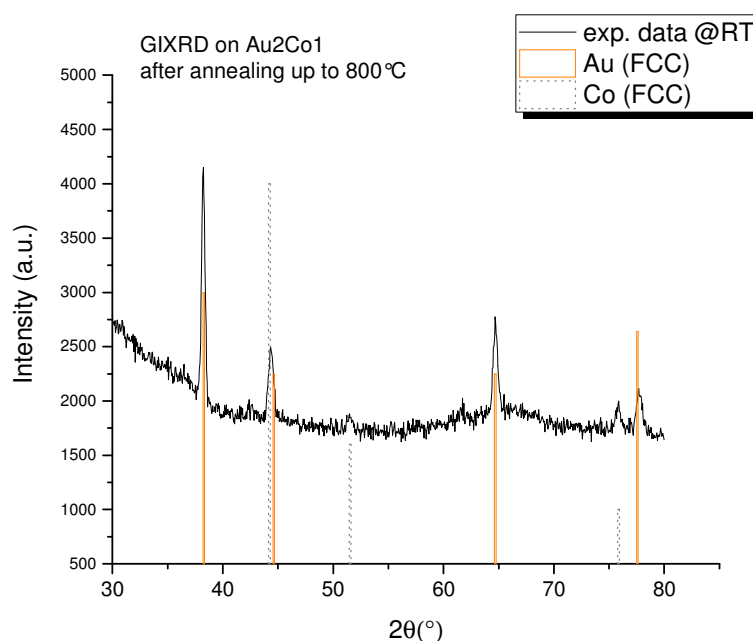
Figure 3.23: GI-XRD data collected on the Au2Co1 cooled sample, after the complete annealing up to 800°C. The pattern is a mixture of pure FCC Au and pure FCC Co, whose reflections are also depicted.
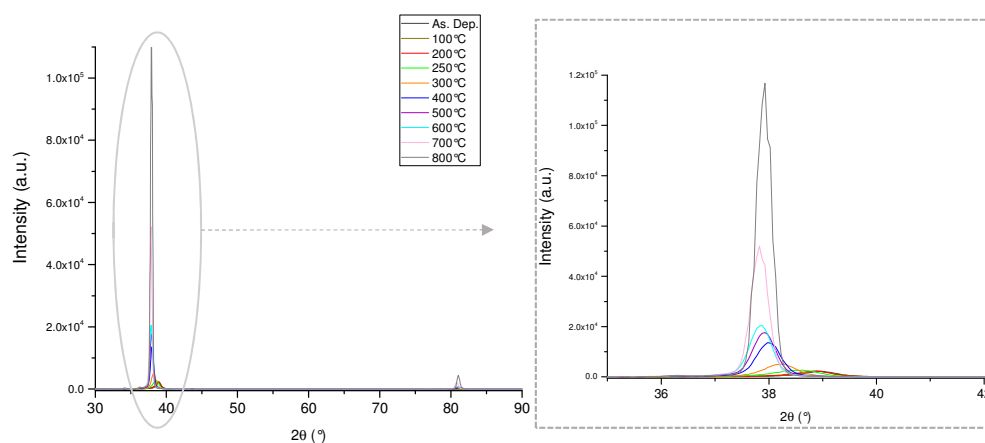
Figure 3.24: On the left, the collected $\omega - 2\theta$ patterns as a function of the temperature steps. The (111) and (311) reflection of a FCC lattice appear. On the right, a magnification of the (111) peak, highlighting the shift of the maximum and the increase of the intensity.

is subjected to a thermal expansion; indeed, the value inferred from a Room Temperature (RT) measurement after the complete thermal treatment is compatible with that of pure gold [64].

The grazing incidence measurements, together with the symmetric scans, suggest that in this sample the segregation of the two constituting metals is accompanied by a strong
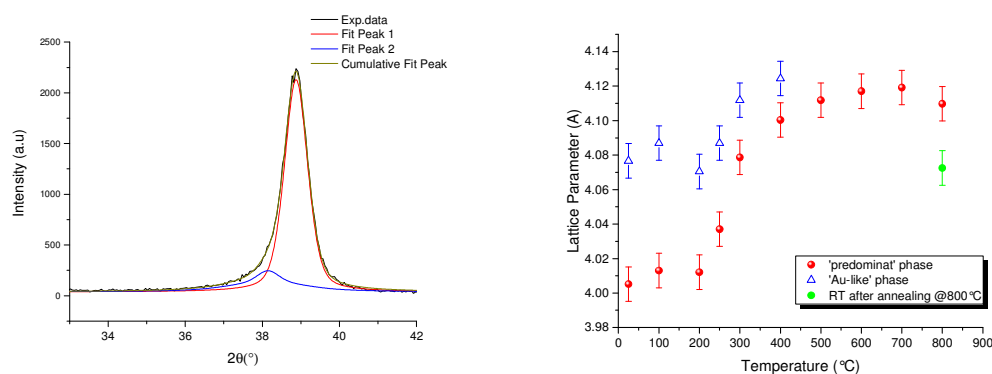
Figure 3.25: On the left, a representative example of (111) peak fitting -in symmetric scan- with two pseudo-Voigt functions. On the right, data of the corresponding lattice parameters (in Å): red circles are related to the 'predominant' phase, see 'Fit Peak 1' on the left, blue triangles are related to the 'secondary' phase, highlighted by the 'Fit Peak 2'; The green circle is related to the sample cooled at RT after the complete annealing.

texturing of the FCC gold phase with the alignment of the (111) planes parallel to the substrate.

The separation of cobalt from gold is also highlighted by Scanning Electron Microscopy (SEM) imaging and Energy Dispersive Spectroscopy (EDS) microanalysis performed with a Zeiss Sigma HD field-emission scanning electron microscope (FE-SEM). The SEM was operated at 5kV for imaging using the In-Lens detector. A compositional map of EDS was carried out with a scanning step of about 20 nm; the apparatus was operated at 20kV and employed a SDD detector with a resolution of 129 eV for fluorescence X-Ray analysis. To detect the spatial distribution of the two metals, the signal was collected respectively at the $L_{\alpha 1}$ line for Au and at the $K_{\alpha 1}$ for Co. The EDS map is reported in Fig. 3.26-a), with the corresponding SEM image in b).

The segregation of Au and Co as a function of the temperature is also confirmed in the balanced and Co-rich films. The 30 nm-coatings set was measured by XRD, after an annealing performed *ex-situ* at 500° C. Reducing gas (mixture of Argon and 2 % Hydrogen) was fluxed inside the furnace during the one hour-treatment. The GI-XRD spectra for the Au2Co1 film as well as the Au1Co1 and Au1Co2 films, collected after the annealing, are reported in Fig. 3.27. For comparison the reflections corresponding to the pure Au and Co bulk phases (FCC) and to the Oxidized Co (Co_3O_4) are also reported. It is confirmed that the phase separation is complete: a FCC phase of pure gold coexists with a FCC phase of Co_3O_4. The oxidation of cobalt is probably due to a small partial pressure of Oxygen, in any case present inside the furnace, despite the reducing gas employed.
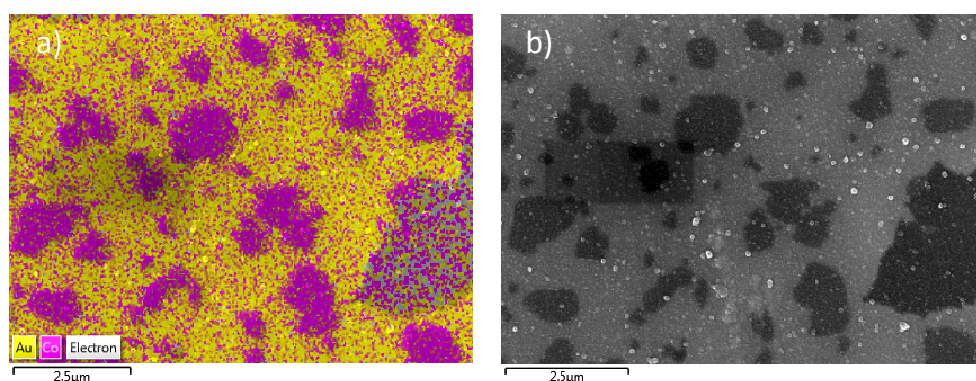
Figure 3.26: In a), the EDS map performed on the sample annealed at the diffractometer according to the ramp in 3.21-right. Yellow spots correspond to gold, Pink spots are related to cobalt. In b), the corresponding SEM image of the area in a). The scale bar measures 2.5 μm.

Moreover, in these samples, thermally treated without a capping layer of silica, the coat-
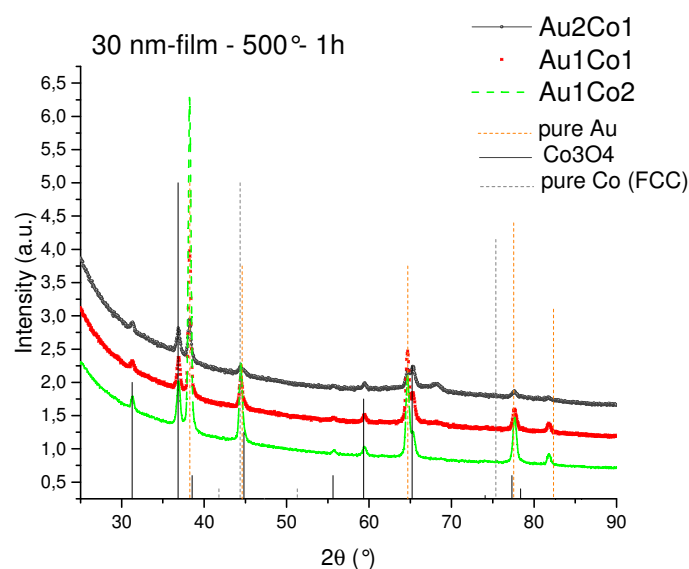
Figure 3.27: The GIXRD spectra related to the 30 nm-thick set after an annealing at $500°C$, 1 hour long, performed *ex situ* in a tubular furnace (reducing atmosphere).

ings undergo a dewetting process. This is demonstrated by the appearance of a surface signal, belonging to the silica substrate, in the corresponding RBS spectra and by a morphological characterization through SEM imaging. Islands of pure gold are mixed with particles of cobalt as demonstrated by the mapping of Au and Co signals in EDS analysis. The elemental maps are reported in Fig. 3.28 at two magnifications with the corresponding SEM morphological images.

Even if far from the scope of this work, the formation of a network of interconnected par-
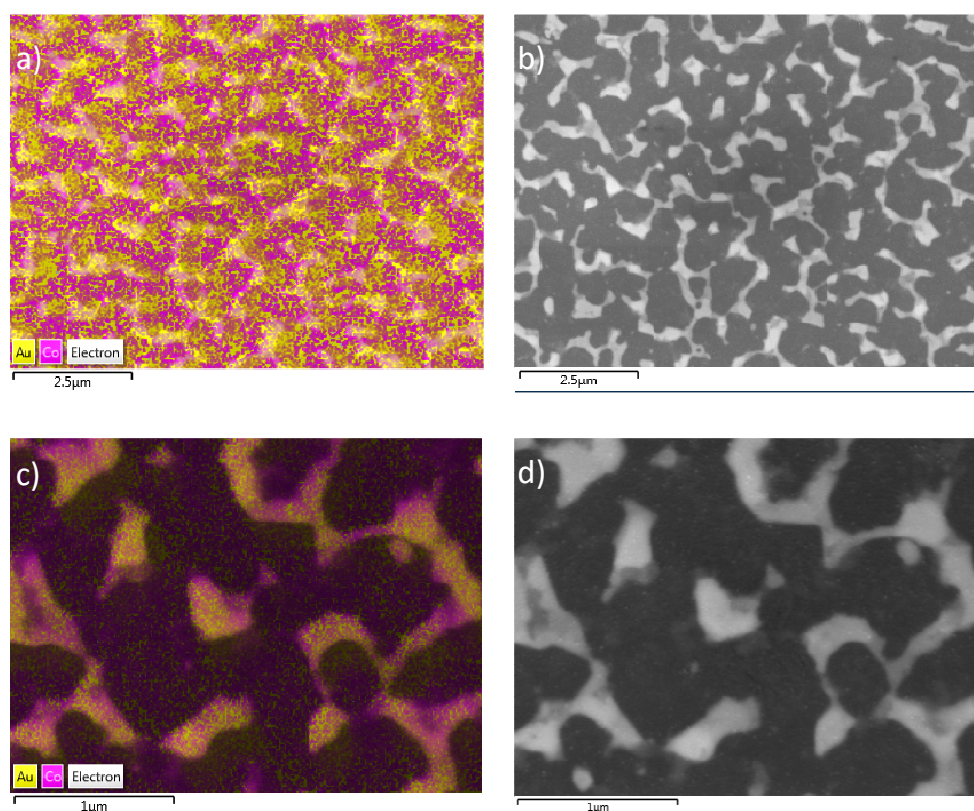
Figure 3.28: Images a)-c) report the EDS maps performed at two magnification on the sample Au2Co1 annealed in furnace at 500° for 1 hour. Yellow spots correspond to gold detected through the $L_{\alpha1}$, Pink spots are related to cobalt, detected through the $K_{\alpha1}$. In b), the corresponding SEM image of the area in a). The scale bar measures 2.5 μm. d): the corresponding SEM image of the area in c). The scale bar measures 1 μm. The SEM was operated at 20kV for X-Ray analysis and at about 5kV for imaging.

ticles of gold mixed with nano-particles of cobalt could be taken into account in the design of nanostructured arrangement where the properties of this noble metal need to be coupled to the magnetic behavior through nearby but at the same time segregated features. Furthermore, the system can be embedded in a desired matrix, as dielectric or transparent material, for instance.

Also X-Ray absorption analysis confirms that the Au:Co films are stable up to 200° C; then a transformation starts, leading to a de-alloying process since 250° C. The measurements, on the 30 nm-Au2Co1 film thermally treated (*ex-situ*) at 250° C and up to at 800° C, have been performed at the BM08 Italian Beamline of the European Synchrotron –ESRF (Grenoble) at the Co K- edges similarly to the experiment detailed in section 2.3.3. The equipment included a 13-element HP Ge detector, a (311) Si double crystal monochroma-

tor working in dynamical focusing mode and a couple of Pd-coated mirrors for harmonics rejection. During the measurements, the samples were cooled at 80 K to reduce thermal vibrations. A Au/Co bilayer i.e., a 8 nm-thick pure cobalt layer coated with a 12 nm-thick layer of pure gold, deposited on silica substrate, was measured as a reference film.

The EXAFS signal in k-space corresponding to Au2Co1 coating thermally treated at 250° C and 800° C are compared to that of as deposited sample and to that of the Au-Co bi-layered system, in Fig 3.29.

The data revel that the interatomic distance in the annealed samples move towards the
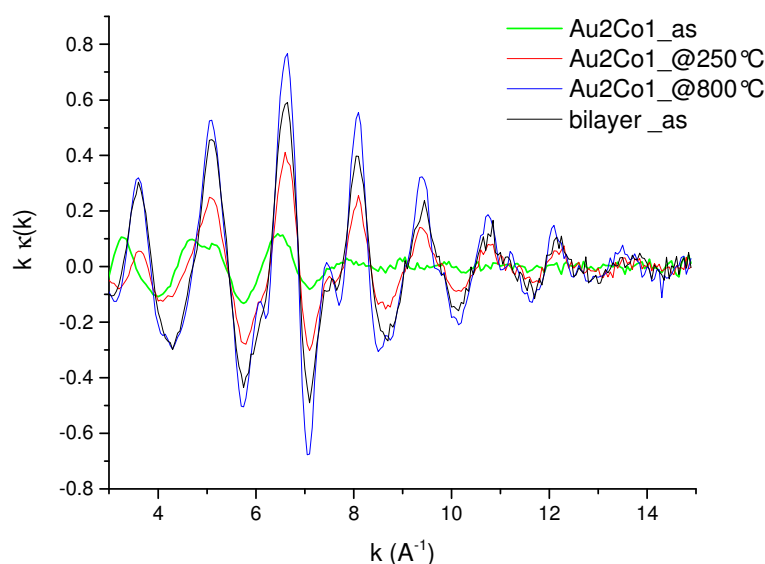
Figure 3.29: EXAFS data, at the Co k- edge, for the Au2Co1 film in the k-space: comparison between the signal for the film annealed at 250° C and the one thermally treated up to 800° C (embedded in silica), with the as deposited coating and the Au-on-Co bi-layers

value characterizing the bi-layers where Co is completely separated from Au and only poly-cristalline phases are present. Moreover, the features of the alloy are lost and the structure resembles that of a completely segregated system, approaching that of a long-range ordered system in the case of the sample annealed up to 800° C.

4 3D Nanostructures

This Chapter describes periodic arrangements of nanostructures whose composition is the same as the Au:Co compounds detailed before. The two kinds of bi-dimensional arrangements considered here are the Semi Nano Shell Array and the Nano Hole Array.
Results on their morphological characterization as well as on their far field optical response will be presented.

4.1 Introduction

After the investigation on the alloying behaviour of gold and cobalt at a nano-scale level in thin films, the research moved toward the study on the feasibility of replicate the alloy features in confined nanostructures. As seen in Chapter 1, the capability to realize nanostructured bimetallic compounds allows to couple the plasmonic features of noble metal -Au- to the magnetic properties of the transition metal counterpart -Co- in innovative magnetoplasmonic platforms suitable for further magneto-optical characterizations.

Two classes of nanostructures have been mainly investigated: the NHA (Nano Hole array), i.e., a periodic array of nanometric holes drilled in a thin metallic film, which can sustain extended plasmons and the Semi-NanoShell Array (SNSA), which can be modeled as a periodic array of spherical cups where localized plasmons occur.

The synthesis procedure is based in both cases on Nanosphere Lithography (NSL) [93], a fast, simple and not expensive technique to produce bi-dimensional patterns at the nanoscale on a large area (typically of order of cm^2). The first step, common to the synthesis procedure for both kinds of arrays is, indeed, the preparation of a nanoparticles' mask by the self-assembling of monodisperse Polystyrene (PS) nanospheres on a substrate in a hexagonal close packed single mono-layer.

In particular, a modified version of a dip coated method has been adopted [94], where the self-assembly of the nanoparticles takes place at the interface between two liquid phases.

The starting PS nanoparticles solution (wt. 10%) was purchased from Microparticles GmbH (Germany); the nominal diameter was 522 ± 12 nm. The monolayer formation is based on the following steps:

1. 20 μL of a solution PS suspension:isopropyl alcohol (50:50 % in volume) is spread on a Soda Lime Glass (SLG) substrate 2 x 2 cm^2 previously cleaned with an acid piranha solution;

2. this substrate, inclined with a certain angle, is immersed into a glass vessel filled with Milli-Q water (18.2MΩ\cm resistivity) using a motorized system which assures an uniform velocity during the immersion;

3. PS nanoparticles form a monolayer on the water surface thanks to the capillary forces at the meniscus between the alcoholic suspension and the water;

4. the first substrate is automatically moved up outside the vessel and another cleaned substrate (slices of HSQ 300 silica or mono-crystalline silicon) is manually immersed into the vessel to collect the resulting compact monolayer which floats on the water surface;

5. the masked substrates are dried at room temperature.

The monolayers quality was investigated by morphological measurements, carried out by Atomic Force Microscopy (AFM) measurements. The characterization was performed with a NT-MDT Solver PRO-M microscope equipped with a 100 x 100 μm scanner. An example of AFM image is reported in Fig. 4.1-a) with the corresponding FFT (4.1-b)) exploited to estimate the actual diameter of the nanospheres. Measuring the distance between ten spots, in the FFT image, a value of 514 ± 10 nm has been inferred, in good agreement with the nominal value. Before the synthesis of the monolayer, the substrate was cleaned in a piranha solution (3:1 by volume of 30% H_2O_2 and 98% H_2SO_4) for 1 hour at 90 °C and then washed with ultra-pure milli-Q water. This step is mandatory to make the surface extremely hydrophilic. Sulfuric Acid and Hydrogen Peroxide were purchased from Sigma-Aldrich as the Isopropyl alcohol with purity ≥ 99.7 % employed for the dilution of the PS suspension.

The first step of the array preparation was followed by a Reactive Ion Etching (RIE) process (to reduce the PS nanosphere diameter without atering the particle-to-oarticle distance) and a sputtering deposition of the two metals, whose parameters depend on the particular system to be considered. The corresponding details will be presented in section 4.4 respec-
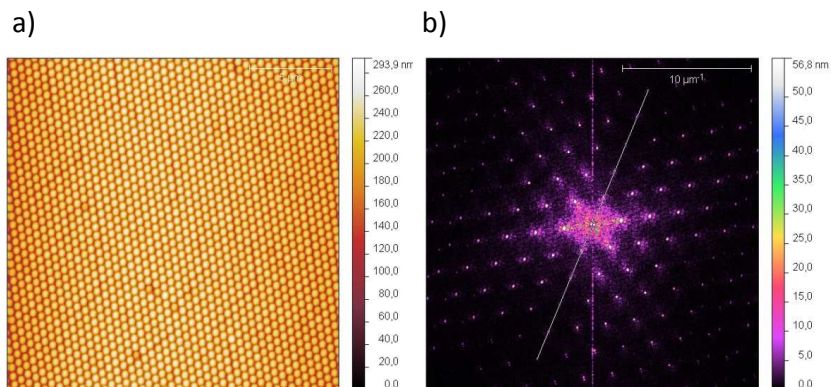
Figure 4.1: a) AFM image 20 x 20 μm^2 of a PS monolayer with nominal Diameter (D) 522 $\pm$ 12 nm. b) Fast Fourier Transform (FFT) of the AFM image in a), the white line was used to measure the distance between 10 spots and to extract the actual diameter of the nanospheres.

tively for the Nano Hole Array (NHA) and in section 4.3 for the SNSA.

4.2 Nano-Holes Array

A Nano Holes Array (NHA) is a periodic array of tiny holes in an opaque metal film, with size smaller than the wavelength of incident light. This arrangement exhibits peculiar optical properties as strongly enhanced transmission of light through holes [95] and wavelength filtering. These effects arise from the interaction of the impinging radiation with electronic resonances in the surface of the metal film. The periodic features characterizing these systems, provide, indeed, the momentum conservation necessary for the coupling process between the incident wavelength and the free surface charges (see equations 1.15 and Fig. 1.2). The metallic component can then sustain SPPs modes, which play a crucial role in the transmission of light through the sub-wavelength holes array, leading to the so called *Extraordinary Optical Transmission (EOT)*. This phenomenon occurs when the *transmission efficiency*, η, is larger than 1, i.e., the flux of photons per unit area emerging from the holes is larger than the incident flux per unit area.

The process can be basically divided into three steps [96]:

1. the coupling of the light to SPs on the incident surface;

2. the transmission through the holes to the second surface;

3. the re-emission from the second surface;

The intensity of the enhanced plasmonic field above each hole compensates for the ineffi-cient transmission (when the propagation regime is substituted by the evanescent regime) through each individual sub-wavelength hole. The EOT can be in principle observed in the case of a single aperture, due to the excitations of Localized Plasmons [97], or due to the presence of periodic corrugations surrounding the holes [98]. Nevertheless, a sizeable effect can be addressed by the periodic array, which can also act as a filter. Peculiar trans-mission peaks appear when the momentum-matching conditions are verified and depend on the geometrical parameters of the array and on the optical features of the metal and of the sourronding dielectric medium. At the peak transmissions, standing Surface Plasmons waves are formed on the surface, associated with high field enhancement.

The NHA have been gathering increasing attention for their potential applications in many fields of science and technology. In the field of opto-electronics, for instance, studies are being carried out to extract more light from light emitting diode [99]. The EOT can be employed in SPs-activated mask for new generation lithography, in order to obtain sub-wavelength features in the near-field and high throughput [100]. Another promising area of application is their integration in biochips as sensing elements, where the high optical contrast, the small size, the strengthen of the input and output optical fields and, addi-tionally, the focusing capability, can all be exploited [101]. The combination of molecules and holes can find application in the spectroscopic area [102], and for catalytic transfor-mations. Finally, sub-wavelength holes might find use in quantum and atom optics, where the manipulation of the atoms and the control of their direction, is needed [103].

NHAs, particularly made up of ferromagnetic materials, have been tested in magnetoplas-monic system, as seen in sections 1.2.2 and 1.2.3. In principle, indeed, all the metals can support Surface Plasmon modes, however a minimization of losses should be expected by coupling cobalt with gold. The choice of the metal is, indeed, a crucial parameter in the design of NHA, beside the geometrical factors as the symmetry of the structure, the aspect ratio and shape of the holes, the aperture area and so on.

In our case, the initial diameter of the PS nanospheres determines the period of the ar-ray. The size of the hole is instead tuned through an *ad hoc* RIE process, an etching process typically used to remove matter from a substrate in micro- and nano-fabrication area. Our Reactive Ion etching is, in particular, an ion-assisted dry etching based on a combination of chemical and physical mechanisms. The masked substrates were positioned on a copper platter inside a cylindrical vacuum chamber and electrically connected to a

radio-frequency source. A gas mixture of Argon and Oxigen was fluxed inside the chamber and ignited to generate a plasma: due to the voltage difference, the positive ions were attracted to the platter, colliding with the sample to be etched. The chemical etching of PS is due to oxygen ions, while Ar^+ ions remove the polymer transferring part of their kinetic energy, as in a sputtering process. The gas mixture, the total pressure inside the chamber and the etching time have been properly optimized to get a maximum reduction of the diameter of the nanosphere, while preserving their stability. The strong reduction of the PS spheres diameter correspond to a minimization of the holes in the final array, essential, as previously seen, to enhance the evanescent regime characteristic of the Surface Plasmon modes. It was indeed, observed that a much aggressive etching can damage the nanospheres shape deteriorating, also, their stability. The quality of the etched mask can be monitored by electron microscopy analysis. In particular, Field Emission Scanning Electron Microscopy (FE-SEM) measurements have been performed with a Zeiss SIGMA HD operating in the $0.2 \div 30$ kV range, with a spatial resolution of about 1.2 nm at 30 kV.

In Fig. 4.2-a) the morphology of the PS nanospheres etched with an optimized RIE process is reported. The etching parameters were: a total gas pressure of $\approx 370 \times 10^{-3}$ mbar, a percentage of Oxygen in the mixture of 70%, a power of 12 W provided to the source and a treatment time of 7'. The RIE process need to be, indeed, optimized to achieve the maximum reduction of the PS spheres diameter while maintaining the stability of the nanoparticles. An example of optimized RIE is reported in Fig. 4.2-b), which shows a SEM images acquired in cross-section. It is worth noting that the intrinsic anisotropy of the RIE process slightly changes the shape of the nanoparticles from spheres to lens-like nanoparticles; this does not compromise the whole synthesis procedure. Nevertheless, a too aggressive etching process can induce a collapse of the PS spheres into the substrate; an example of this unusable mask is reported in the cross-view SEM of Fig. 4.2-c).

From the measurements of nanospheres' diameter, an average value of 280 ± 9 nm was obtained.

The steps needed to complete the preparation of the NHAs are summarized in Fig. 4.3.

The etching step is followed by a magnetron deposition carried out in co-focusing geometry. In particular, NHAs have been deposited in the same batch of the corresponding continuous films (according to the process parameters detailed in section 2.2), so that, also in the case of these nanostructures, three compositions will be considered: a 'balanced'
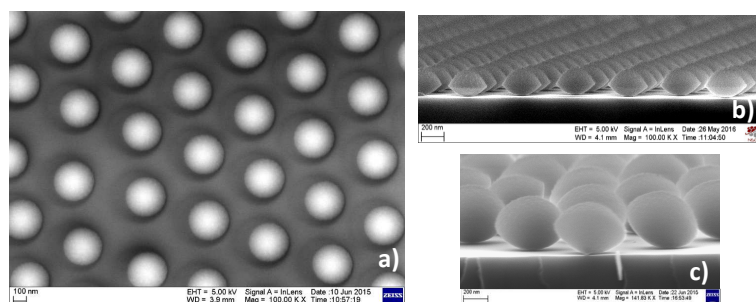
Figure 4.2: SEM images of etched Polystyrene monolayers deposited on silicon substrate. a) top-view at 100 kX of the PS spheres subjected to a RIE process properly tuned for the NHA preparation (see text for geometrical details). b) cross-view at 100 kX highlighting the anisotropy typical of the etching process. c) SEM cross-view image showing the results of a not optimized i.e., too aggressive etching process.
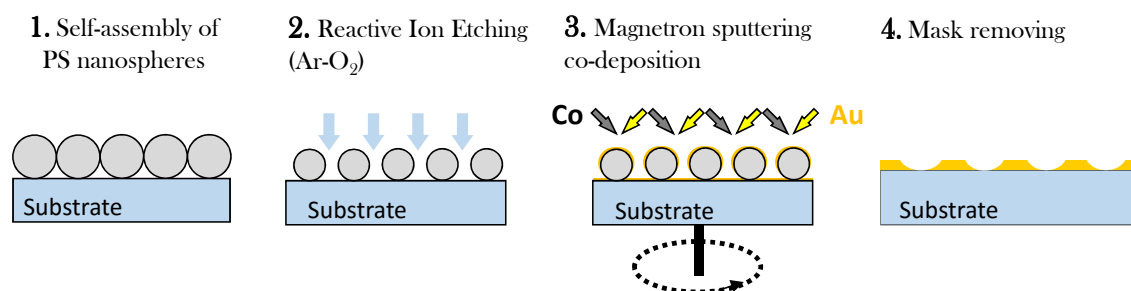
Figure 4.3: Schematic diagram of the synthesis process of NHA: 1) self-assembly of a PS nanospheres mask on a substrate, typically silica (HSQ300) or Si; 2) reactive ion etching to reduce the PS diameter; 3) cosputtering deposition of Au and Co (see 2.2); 4) removal of the PS mask by an adhesive tape.

Au1Co1 NHA, two un-balanced ones, i.e., Au2Co1 NHA (rich in Au) and Au1Co2 NHA (rich in Co). Moreover, it is reasonable to assume that, given the gap between the etched nanospheres, the mechanisms of the growth of the metallic coating are the same as for the solid films.

The thickness of the material surrounding the holes, is, indeed, an important parameter in the design of the array [96], as it should be several times the skin-depth (see section 1.2.1) of the metal to assure a strong opacity compared to the apertures. A final thickness of 85-95 nm was selected, since typical values of skin depth for noble metal are of the order of 20 nm.

After the Au:Co film deposition, the PS were removed by an adhesive tape. The final results is a hexagonal array of holes in the thin metal on the substrate.

The morphology of the NHAs has been characterized through FE-SEM. Fig. 4.4 reports, as an example, the images for the Au2Co1 NHA, acquired at different magnifications.
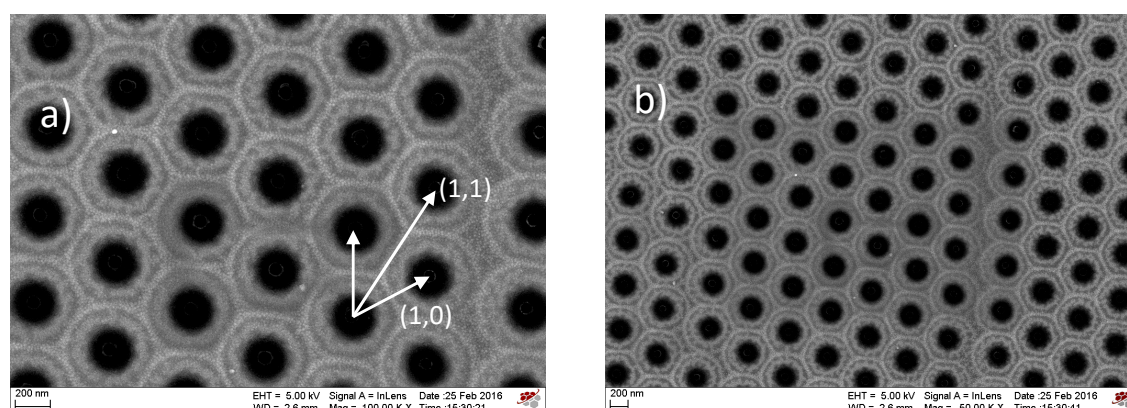
Figure 4.4: a) SEM image 100 kX of a representative NHA; the arrows represent the vector needed to describe the periodic arrangement of holes, the the i,j index are also indicated. b) SEM image at 50 kX of the same NHA.

Fig. 4.4 describes also the geometry of the periodic pattern: the vector (i,j) identifying the holes' position can be indexed with (1,0) and (1,1). From the analysis of the SEM image, it is possible to infer the geometrical parameters. The period is confirmed to be 514 ± 9 nm, corresponding to the diameter of the untreated nanoparticles. From Fig. 4.4-a) the average diameter of the holes is 274 ± 6 nm, in agreement with the diameter of the etched PS nanospheres just after the RIE process. It is worth noting, that this value correspond to the measurements of the 'projection' of the holes, assuming a cylindrical shape of the apertures.

Looking instead at the FE-SEM image acquired with the detection of the secondary electron, see Fig. 4.5, it is clear that the morphology of the holes is more complex. Due to the co-focusing geometry of the deposition process, part of the Au and Co atoms can be deposited also in an annular region underlying the PS spheres. The uncovered area results, actually, lower than seen before, its diameter being 249 ± 10 nm. Then there is a thickness gradient going from this area to a 'cuspid' zone, which corresponds to the highest ring surrounding the hole.

The optical properties of the as prepared NHAs have been characterized by means of UV-Vis measurements performed in transmission mode with a JASCO V670 spectrophotometer in the 200-1500 nm wavelength range. The data are summarized in Fig. 4.6-a), -b) and -c) (orange line) for the array of composition Au2Co1, Au1Co1 and Au1Co2, respectively. Furthermore the transmission spectra of a pure-Co NHA, which shows a geometry similar to that of the previous ones, has been measured as reference as well: the data are reported
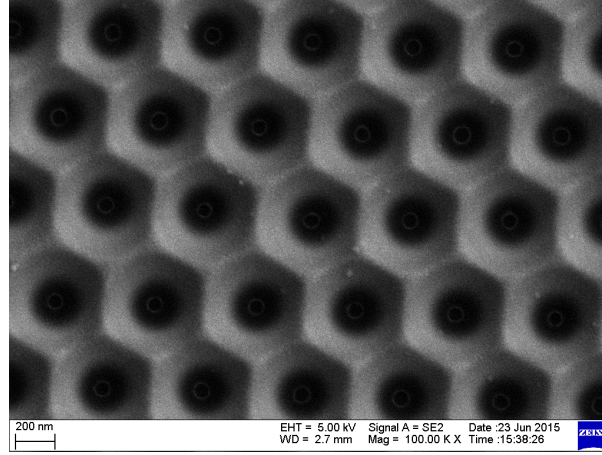
Figure 4.5: FE-SEM image of a representative NHA acquired at 100 kX by detection of secondary electron to enhance the morphology features; the maximum thickness in the annular region around the holes decreases towards the voids according to a spherical profile.

in Fig. 4.6-d). All the NHAs have been measured before (black line) and after (orange line) removing the PS spheres.

After pulling out the PS mask, the NHAs typically show three features in the transmission spectra: a peak between 400 and 500 nm and and two broadbands locate respectively around 300 and 1000 nm. From a theoretical point of view, applying the momentum-matching conditions -equations 1.15- and assuming a virtually vanishing hole size, it is possible to calculate the wavelength of the maximum transmittance, at normal incidence, for the hexagonal 2D lattice, with the expression:

$$\lambda_{max} = \frac{a}{\sqrt{\frac{4}{3}(i^2 + ij + j^2)}} \sqrt{\frac{\varepsilon_m \varepsilon_d}{\varepsilon_m + \varepsilon_d}} \qquad (4.1)$$

where a is the period of the array (in our case 514 nm,) i, j are the index of the vector lattice as depicted in Fig. 4.4-a), ε_m and ε_d are the dielectric constant - see equation 1.3- of the metal constituting the NHA and of the dielectric material in contact with the metal, respectively. Fig. 4.6 showss the results of the calculation concerning the composition, as a function of the $(1,0)$ or $(1,1)$ lattice vector and the dielectric material, i.e., silica and air (It is worth noting that the NHAs are deposited on silica while their surface is directly exposed to ambient air). The ε_d of the silica was set at 2.15, i.e., the experimental value measured on a bare substrate by means of Ellipsometry. The positions of the calculated λ_{max} are indicated by the arrows where the name of the corresponding dielectric material
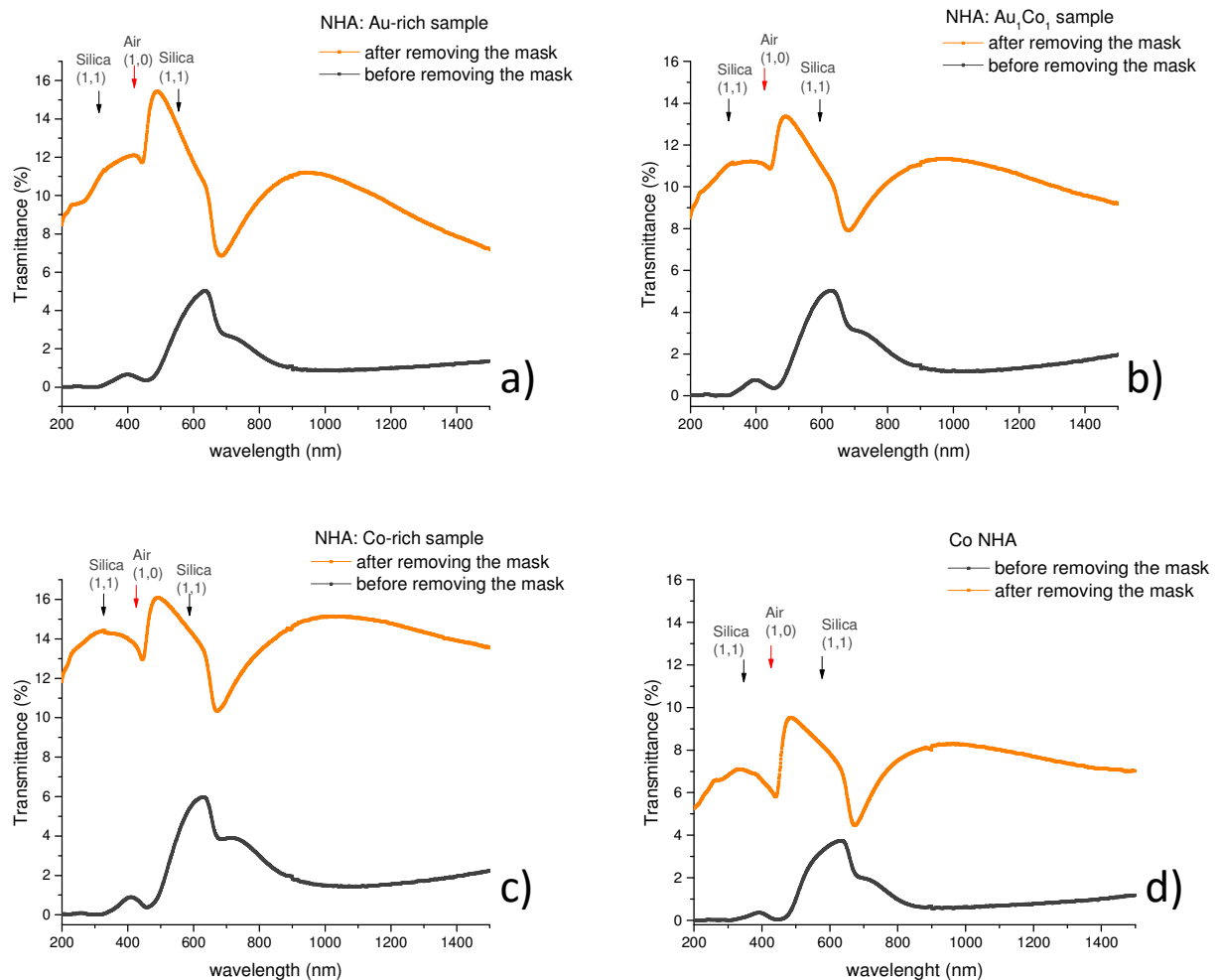
Figure 4.6: UV-Vis transmission data of NHAs of stoichiometry a) Au2Co1, b) Au1Co1, c) Au1Co2, respectively. In d) the transmission spectra of a NHA of pure cobalt. The arrows indicate the wavlenegth at whic the maximum transmission should occurs according to equation 4.1.

and of the (i, j) index are reported as well.

In all the cases the experimental transmission features experience a red-shift respect to the calculated positions. This is generally observed in literature as the simple model adopted does not take into account the finite diameter of the holes and the possible correlated interference phenomena [104]. From quantum-mechanics studies [105], red shift is explained taking into account two interfering contributions to the transmission; to the resonant mode of transmission mediated by the surface plasmon polaritons excitations at the two interfaces (described before), it should be added a non-resonant contribution arising from the direct light transmission through the holes. Their interference causes a red-shift of the peak and induces also an asymmetry on the spectral shape, typical of Fano-like resonance.

Furthermore the thickness of the metal should be considered as well [106]: it is certainly not semi-infinite as expected in the ideal model and, in our case, as seen before, it is not constant but follows a complex profile and vanishes in proximity of the holes. This weakens the strong constrain of opacity intrinsic to an ideal NHA and, moreover, can lead to a coupling of the modes occurring on either sides of the array or the interference with the non-resonant contribution of light transmitted directly through the array.

For what concerns the material composition, the addition of gold to cobalt, on average enhance the optical performance of pure-Co NHA. The increase of the transmission is not proportional to the Au content as an important parameter to be considered is the regularity of the holes and of the array. The uniformity, indeed, depends on the specific batch of synthesis and in particular on the step of the mono-layer self-assembly which rules the following steps (see Fig. 4.3) of the process and the final geometry. Certainly these steps are eligible for further optimization.

4.3   Semi nano-Shell Array

The array of Semi Nano-Shells (SNSA) is the other 3D-nanostructured system, prepared and characterized in this work.

The first three steps of the synthesis procedure are similar to that of the NHA a part the removing of the PS: the final structure is an hexagonal array of Semi Nano-Shell units coated with a thin Au:Co film. The process scheme is sketched in Fig. 4.7.
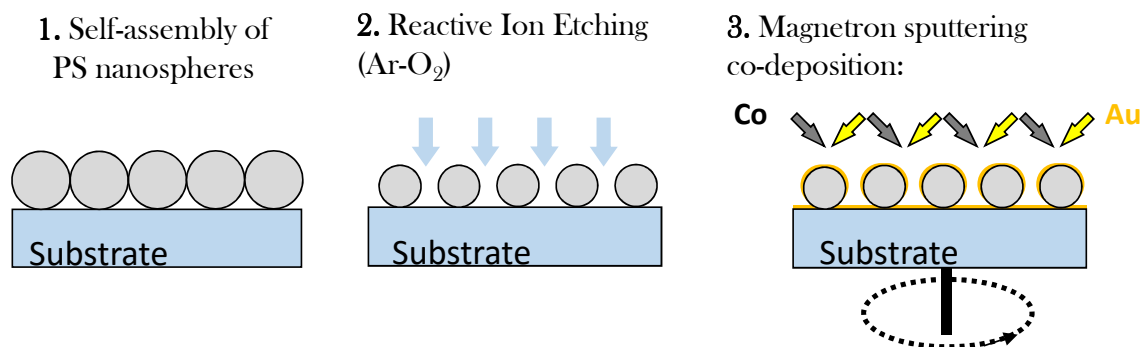
Figure 4.7: Schematic diagram of the synthesis process of NHA: 1) self-assembly of a PS nanospheres mask on a substrate, typically silica (HSQ300) or Si; 2) a 'soft' reactive ion etching to slightly reduce the PS diameter; 3) cosputtering deposition of Au and Co (see section 2.2).

In this case, a soft etching step has been employed, to slightly reduce the initial diameter of

the PS nanosphere. In particular, the total working pressure was fixed at $\approx 9 \times 10^{-3}$mbar, i.e., lower than in the case of NHA treatment. The other parameters were: a percentage of Oxygen in the mixture of 70%, a power of 10 W provided to the source and a treatment time of 6'. After the etching step, the PS nanoparticles have been coated with a thin Au:Co film; the magnetron sputtering deposition process was carried out with the same parameters adopted for the deposition of 30 nm-thick continuous films (see section 2.2). Two representative FE-SEM images are reported in Fig. 4.8, before (left) and after (right) the coating deposition. From the analysis of the images, the diameter of the PS nanospheres is 412 ± 7 nm just after the RIE process and 438 ± 11 nm after the magnetron sputtering deposition.
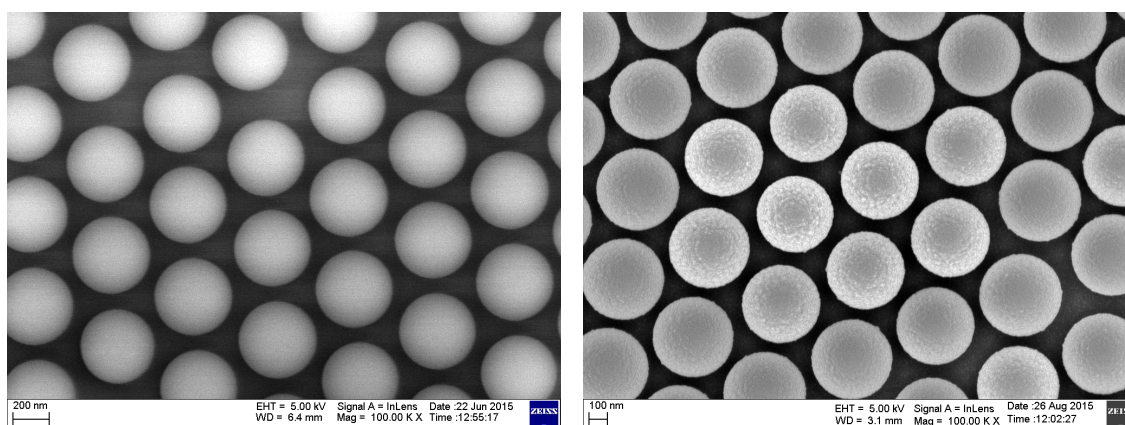
Figure 4.8: On the left, FE-SEM image at 100 kX of a representative SNSA. On the right, the same SNSA covered with a 30 nm-thick Au:Co coating.

Finally, the SNSAs have been coated with silica layers, still deposited by means of magnetron sputtering process, to prevent possible oxidation of the cobalt. Due to the particular geometry of these arrangement the surface/volume is by far higher with respect to the solid films increasing the risk of oxidation phenomena. The thickness of the silica top layers was about 200 nm.

As seen, the Semi Nano-Shells are essentially PS nanospheres partially coated on top with a Au:Co film, with a thickness of $\approx$30 nm. The full structural characterization performed on the solid films, confirmed the Au-Co alloy formation and provided a description of the obtained solid solution in terms of composition and local order (see section 2.4). It is reasonable to assume that alloying takes place also in the coating of the Semi Nano-Shells, as the process parameters of the magnetron sputtering deposition were similar to those of the corresponding films. Nevertheless, SNSAs have been characterized by means of X-ray

Absorption analysis to verify this hypothesis. The measurements were performed at the BM08 Italian Beamline at ESRF (Grenoble, France) in the experimental conditions described in section 2.3.3.

The analysis indicates that Co atoms are in the metallic state. The combined EXAFS
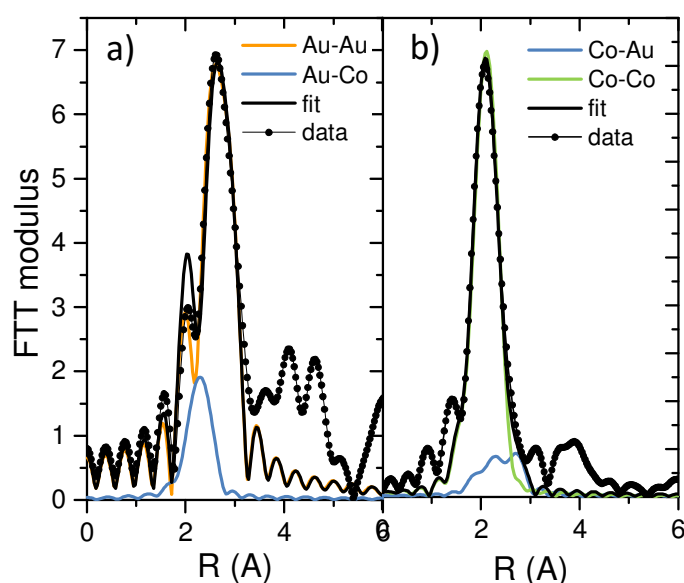
Figure 4.9: Multiparameter first shell fits (intermetallic coordination) superimposed to the EXAFS data for Au1Co1 SNSA: a) Au edge, b) Co edge in R-space. the single scattering contributions to the fit are reported.

analysis of the Au-edge and Co-edge spectra highlighted a Au-Co first shell coordination, confirming the formation of a Au-Co alloy in all the SNSAs. A representative example of the results is reported in Fig. 4.9 which shows the EXAFS data of the Au1Co1 sample in R-space.

The resulting first shell coordination distances are about 2.81 Å for the Au-Au distance, 2.65 Å for the Au-Co distance and 2.47 Å for the Co-Co distance. These data are similar to those obtained in the corresponding solid film (see Table 2.5); the alloy fraction is $\approx 60\%$ and, also in this case, is richer in gold.

The far-field response of SNSAs have been characterized through UV-Vis measurements performed with a JASCO V670 dual beam spectrophotometer. The collected data are reported in Fig. 4.10, in the wavelength range of 450 - 1800 nm. As a reference, the absorbance of SNSAs of pure gold and pure cobalt, prepared in similar conditions and showing similar geometrical parameters, are reported as well.

The modulation of the signal is due to the occurrence of localized plasmonic modes typical
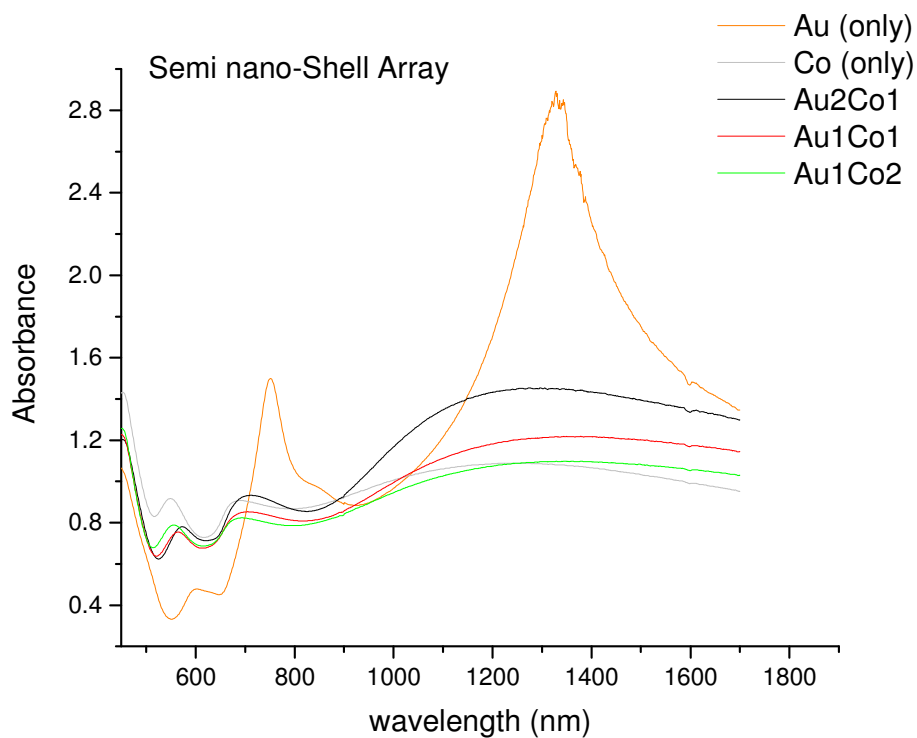
Figure 4.10: The Uv-Vis absorbance of arrays of Semi nano-Shells covered with a thin layer of pure-Au, pure-Co, and Au-rich, Au1Co1 and Co-rich alloy, respectively.

of the nano-shells, which can be modeled as (partial) core-shell nanoparticles (see section 1.2.1) with a metallic skin and a dielectric core (i.e., Polystyrene). Moreover, as the gap between adjacent shells in the final array is on the average less than 50 nm, a lateral coupling between LSPs can take place leading to a red-shift of the optical features.

It is demonstrated the alloy enhances the optical response of a pure cobalt SNSA, due to the reduction of the imaginary part of the effective dielectric function and therefore of the optical losses, enabling these systems as suitable for future magneto-plasmonic activity.

Conclusions and Perspectives

In this thesis, thin films of Au-Co alloy have been deposited by means of co-focusing magnetron sputtering technique, and characterized in terms of structural, optical as well as magnetic properties. Three compositions have been considered (Au2Co1, Au1Co1 and Au1Co2) together with three values of film thickness ($\approx$ 15 nm, $\approx$ 30 nm and $\approx$ 100 nm). The alloy formation has been demonstrated and studied by a combination of structural techniques, i.e., X-Ray Diffraction, X-Ray Absorption Spectroscopy and Transmission Electron Microscopy, which, furthermore, allowed the characterization of the alloy in terms of stoichiometry and local order.

In particular, in the Au-rich coating, the alloy constitutes the $\approx$ 85% of the film, has a stoichiometry of $Au_{80}Co_{20}$ and is amorphous. In the Au1Co1 and Au1Co2 films, the fraction of the alloy is respectively $\approx$ 70% and $\approx$ 60%, with a stoichiometry of $Au_{70}Co_{30}$ and $Au_{60}Co_{40}$, respectively.

In the case of Au2Co1 sample, the alloy is amorphous, while in the case of alloy richer in cobalt, there are some FCC crystalline seeds, elongated along the direction of the film growth. These grains are highly textured, with the (111) planes parallel to the substrate, and show a lattice constant that shortens as the Co content increases arriving to a value of 3.76 $\pm$ 0.01 Å in the Au1Co2 film.

Besides the alloy, the samples exhibit a phase of segregated cobalt clusters, characterized by a low atomic order, whereas no evidence of Co-oxide has been found.

The presence of two separated magnetic phases in the Co-rich samples is also suggested by SQUID measurements. Some peculiar features in the corresponding hysteresis loops are highlighted, which are probably related to the interplay between the strength of the exchange coupling, the strength and direction of the magnetic anisotropy and the direction of the external applied field and need further investigations.

On the contrary, the alloy in the Au2Co1 sample behaves as a soft ferromagnetic matrix: the embedded Co clusters probably experience a magnetic relaxation process leading to

the observed superparamagnetic behaviour.

Au atoms in the alloy acquire a net magnetic moment as extimated by XMCD measurements at the Au $L_{2,3}$-edges; for instance, in the case of Au1Co1 film, its value is about 0.059 μ_B/atom.

Upon thermal annealing, the alloy is stable up to 200° C; then, as the temperature increases, a transformation occurs leading to the separation of gold and cobalt phases. If the Co oxidation is prevented during the annealing, Co atoms separate into a FCC metallic phase.

The addition of gold to cobalt brings the optical features typical of this noble metal into the compound: the optical constants of Au:Co films have been measured by Ellipsometry for the three compositions.

The alloyed Au-Co compounds have been successfully nanostructured into three dimensional periodic arrangements. Arrays of Semi Nano-Shells and Nano Hole Arrays have been prepared coupling the magnetron sputtering deposition technique with Nano Sphere Lithography steps and a Reactive Ion Etching process. The morphological as well as the optical characterizations of the arrays demonstrate that these systems are promising platforms for future magneto-plasmonic studies and applications.

Bibliography

[1] Maier SA, *Plasmonics: fundamentals and applications* (Springer Science & Business Media, 2007). (Cited on pages xiii, 1, 6, and 11).

[2] Armelles G, Cebollada A, García-Martín A *et al.* (2013) *Magnetoplasmonics: combining magnetic and plasmonic functionalities*. Advanced Optical Materials, **vol. 1, no. 1**:pp. 10–35. (Cited on pages xiii, 1, 6, 16, 17, 21, 22, and 23).

[3] Okamoto H, Massalski T, Nishizawa T *et al.* (1985) *The Au-Co (gold-cobalt) system*. Bulletin of Alloy Phase Diagrams, **vol. 6, no. 5**:pp. 449–454. (Cited on pages xiii, xiv, 24, 26, 27, 38, 56, and 90).

[4] Klement WJ (1963) *Solid Solution in Gold-Cobalt and Copper-Cobalt Alloys*. Trans. Metall. Soc. AIME, **vol. 227, no. 8**:pp. 965–970. (Cited on pages xiii, 25, 26, and 56).

[5] Mader S, Nowick A and Widmer H (1967) *Metastable Co–Au alloys: example of an amorphous ferromagnet*. Acta Metall., **vol. 15**:p. 203. (Cited on pages xiii, 26, 40, and 56).

[6] Tsaur BY, Lau SS and Mayer JW (1981) *Ion-Beam-Induced metastable phases in the Au-Co system*. Philosophical Magazine B, **vol. 44, no. 1**:pp. 95–108. (Cited on pages xiii, 25, 26, 39, and 40).

[7] Inden G (1981) *The role of magnetism in the calculation of phase diagrams*. Physica B+ C, **vol. 103, no. 1**:pp. 82–100. (Cited on pages xiii and 26).

[8] Stöhr J (1999) *Exploring the microscopic origin of magnetic anisotropies with X-ray magnetic circular dichroism (XMCD) spectroscopy*. Journal of Magnetism and Magnetic Materials, **vol. 200, no. 1**:pp. 470–497. (Cited on pages xvi, 71, and 72).

[9] Chen C, Idzerda Y, Lin HJ *et al.* (1995) *Experimental confirmation of the X-ray magnetic circular dichroism sum rules for iron and cobalt*. Physical review letters, **vol. 75, no. 1**:p. 152. (Cited on pages xvi, 72, 73, and 76).

[10] Ozbay E (2006) *Plasmonics: merging photonics and electronics at nanoscale dimensions*. science, **vol. 311, no. 5758**:pp. 189–193. (Cited on page 1).

[11] Zheludev NI and Plum E (2016) *Reconfigurable nanomechanical photonic metamaterials*. Nature nanotechnology, **vol. 11, no. 1**:pp. 16–22. (Cited on page 1).

[12] Liu F, Hou Y and Gao S (2014) *Exchange-coupled nanocomposites: chemical synthesis, characterization and applications*. Chemical Society Reviews, **vol. 43, no. 23**:pp. 8098–8113. (Cited on page 2).

[13] Johnson PB and Christy RW (1972) *Optical constants of the noble metals*. Physical review B, **vol. 6, no. 12**:p. 4370. (Cited on page 2).

[14] Johnson P and Christy R (1974) *Optical constants of transition metals: Ti, v, cr, mn, fe, co, ni, and pd*. Physical Review B, **vol. 9, no. 12**:p. 5056. (Cited on page 2).

[15] Drude P, *The theory of optics* (Courier Corporation, 1925). (Cited on page 8).

[16] Johnson PB and Christy RW (1972) *Optical constants of the noble metals*. Physical review B, **vol. 6, no. 12**:p. 4370. (Cited on page 9).

[17] Mie G (1908) *Beiträge zur Optik trüber Medien, speziell kolloidaler Metallösungen*. Annalen der physik, **vol. 330, no. 3**:pp. 377–445. (Cited on page 12).

[18] Bohren CF and Huffman DR (1983) *Absorption and scattering by a sphere*. Absorption and Scattering of Light by Small Particles, (pp. 82–129). (Cited on pages 13 and 14).

[19] Anker JN, Hall WP, Lyandres O *et al.* (2008) *Biosensing with plasmonic nanosensors*. Nature materials, **vol. 7, no. 6**:pp. 442–453. (Cited on page 14).

[20] Homola J (2008) *Surface plasmon resonance sensors for detection of chemical and biological species*. Chemical reviews, **vol. 108, no. 2**:pp. 462–493. (Cited on page 14).

[21] Kimel A, Kirilyuk A, Usachev P *et al.* (2005) *Ultrafast non-thermal control of magnetization by instantaneous photomagnetic pulses*. Nature, **vol. 435, no. 7042**:pp. 655–657. (Cited on page 14).

[22] Zvezdin A, *Modern magnetooptics and magnetooptical materials*. (Cited on page 15).

[23] Faraday M (1846) *Experimental researches in electricity. Nineteenth series*. Philosophical Transactions of the Royal Society of London, **vol. 136**:pp. 1–20. (Cited on page 15).

[24] Kerr J (1877) *XLIII. On rotation of the plane of polarization by reflection from the pole of a magnet*. The London, Edinburgh, and Dublin Philosophical Magazine and Journal of Science, **vol. 3, no. 19**:pp. 321–343. (Cited on page 15).

[25] Kerr J (1878) *XXIV. On reflection of polarized light from the equatorial surface of a magnet*. The London, Edinburgh, and Dublin Philosophical Magazine and Journal of Science, **vol. 5, no. 30**:pp. 161–177. (Cited on page 15).

[26] Haefner P, Luck E and Mohler E (1994) *Magnetooptical properties of surface plasma waves on copper, silver, gold, and aluminum.* physica status solidi (b), **vol. 185, no. 1**:pp. 289–299. (Cited on page 18).

[27] Pellegrini G and Mattei G (2014) *High-performance magneto-optic surface plasmon resonance sensor design: an optimization approach.* Plasmonics, **vol. 9, no. 6**:pp. 1457–1462. (Cited on page 19).

[28] Hermann C, Kosobukin V, Lampel G *et al.* (2001) *Surface-enhanced magneto-optics in metallic multilayer films.* Physical Review B, **vol. 64, no. 23**:p. 235422. (Cited on page 19).

[29] Ctistis G, Papaioannou E, Patoka P *et al.* (2008) *Optical and magnetic properties of hexagonal arrays of subwavelength holes in optically thin cobalt films.* Nano letters, **vol. 9, no. 1**:pp. 1–6. (Cited on page 19).

[30] Caballero B, García-Martín A and Cuevas J (2012) *Generalized scattering-matrix approach for magneto-optics in periodically patterned multilayer systems.* Physical Review B, **vol. 85, no. 24**:p. 245103. (Cited on page 19).

[31] Papaioannou ET, Kapaklis V, Melander E *et al.* (2011) *Surface plasmons and magneto-optic activity in hexagonal Ni anti-dot arrays.* Optics express, **vol. 19, no. 24**:pp. 23867–23877. (Cited on page 19).

[32] Papaioannou ET, Kapaklis V, Patoka P *et al.* (2010) *Magneto-optic enhancement and magnetic properties in Fe antidot films with hexagonal symmetry.* Physical Review B, **vol. 81, no. 5**:p. 054424. (Cited on page 19).

[33] Belotelov V, Doskolovich L and Zvezdin A (2007) *Extraordinary magneto-optical effects and transmission through metal-dielectric plasmonic systems.* Physical review letters, **vol. 98, no. 7**:p. 077401. (Cited on page 19).

[34] Belotelov V, Akimov I, Pohl M *et al.* (2011) *Enhanced magneto-optical effects in magnetoplasmonic crystals.* Nature Nanotechnology, **vol. 6, no. 6**:pp. 370–376. (Cited on page 19).

[35] Wurtz G, Hendren W, Pollard R *et al.* (2008) *Controlling optical transmission through magneto-plasmonic crystals with an external magnetic field.* New Journal of Physics, **vol. 10, no. 10**:p. 105012. (Cited on page 19).

[36] Hui P and Stroud D (1987) *Theory of Faraday rotation by dilute suspensions of small particles.* Applied physics letters, **vol. 50, no. 15**:pp. 950–952. (Cited on page 19).

[37] González-Díaz JB, García-Martín A, Armelles G *et al.* (2007) *Enhanced Magneto-Optics and Size Effects in Ferromagnetic Nanowire Arrays.* Advanced Materials, **vol. 19, no. 18**:pp. 2643–2647. (Cited on page 19).

[38] Bonanni V, Bonetti S, Pakizeh T *et al.* (2011) *Designer magnetoplasmonics with nickel nanoferromagnets*. Nano letters, **vol. 11, no. 12**:pp. 5333–5338. (Cited on page 20).

[39] Banthí JC, Meneses-Rodríguez D, García F *et al.* (2012) *High Magneto-Optical Activity and Low Optical Losses in Metal-Dielectric Au/Co/Au–SiO2 Magnetoplasmonic Nanodisks*. Advanced Materials, **vol. 24, no. 10**. (Cited on page 20).

[40] Temnov VV, Armelles G, Woggon U *et al.* (2010) *Active magneto-plasmonics in hybrid metal–ferromagnet structures*. Nature Photonics, **vol. 4, no. 2**:pp. 107–111. (Cited on page 20).

[41] Martín-Becerra D, González-Díaz JB, Temnov VV *et al.* (2010) *Enhancement of the magnetic modulation of surface plasmon polaritons in Au/Co/Au films*. Applied Physics Letters, **vol. 97, no. 18**:p. 183114. (Cited on page 20).

[42] Belotelov V, Kreilkamp L, Akimov I *et al.* (2013) *Plasmon-mediated magneto-optical transparency*. Nature communications, **vol. 4**. (Cited on page 20).

[43] Pineider F, Campo G, Bonanni V *et al.* (2013) *Circular magnetoplasmonic modes in gold nanoparticles*. Nano letters, **vol. 13, no. 10**:pp. 4785–4789. (Cited on page 21).

[44] Maccaferri N, Berger A, Bonetti S *et al.* (2013) *Tuning the magneto-optical response of nanosize ferromagnetic Ni disks using the phase of localized plasmons*. Physical review letters, **vol. 111, no. 16**:p. 167401. (Cited on page 21).

[45] Cortie MB and McDonagh AM (2011) *Synthesis and optical properties of hybrid and alloy plasmonic nanoparticles*. Chemical reviews, **vol. 111, no. 6**:pp. 3713–3735. (Cited on page 22).

[46] Martín-Becerra D, García-Martín J, Huttel Y *et al.* (2015) *Optical and magneto-optical properties of Au: Conanoparticles and Co: Aunanoparticles doped magneto-plasmonic systems*. Journal of Applied Physics, **vol. 117, no. 5**:p. 053101. (Cited on page 22).

[47] Yang K, Clavero C, Skuza J *et al.* (2010) *Surface plasmon resonance and magneto-optical enhancement on Au–Co nanocomposite thin films*. Journal of Applied Physics, **vol. 107, no. 10**:p. 103924. (Cited on pages 22, 27, and 56).

[48] Sepúlveda B, Calle A, Lechuga LM *et al.* (2006) *Highly sensitive detection of biomolecules with the magneto-optic surface-plasmon-resonance sensor*. Optics letters, **vol. 31, no. 8**:pp. 1085–1087. (Cited on page 22).

[49] Chou KH, Lin EP, Chen TC *et al.* (2014) *Application of strong transverse magneto-optical Kerr effect on high sensitive surface plasmon grating sensors*. Optics express, **vol. 22, no. 16**:pp. 19794–19802. (Cited on page 22).

[50] Caballero B, García-Martín A and Cuevas JC (2016) *Hybrid Magnetoplasmonic Crystals Boost the Performance of Nanohole Arrays as Plasmonic Sensors*. ACS Photonics. (Cited on page 22).

[51] Herreño-Fierro CA, Patiño EJ, Armelles G *et al.* (2016) *Surface sensitivity of optical and magneto-optical and ellipsometric properties in magnetoplasmonic nanodisks*. Applied Physics Letters, **vol. 108, no. 2**:p. 021109. (Cited on page 22).

[52] Khurgin JB (2006) *Optical isolating action in surface plasmon polaritons*. Applied physics letters, **vol. 89, no. 25**:p. 251115. (Cited on page 23).

[53] Firby C and Elezzabi A (2015) *High-speed nonreciprocal magnetoplasmonic waveguide phase shifter*. Optica, **vol. 2, no. 7**:pp. 598–606. (Cited on page 23).

[54] Zhang Y and Wang Q (2012) *Magnetic-Plasmonic Dual Modulated FePt-Au Ternary Heterostructured Nanorods as a Promising Nano-Bioprobe*. Advanced Materials, **vol. 24, no. 18**:pp. 2485–2490. (Cited on page 23).

[55] Amendola V, Saija R, Maragò OM *et al.* (2015) *Superior plasmon absorption in iron-doped gold nanoparticles*. Nanoscale, **vol. 7, no. 19**:pp. 8782–8792. (Cited on page 23).

[56] Mader S (1966) *Alloy Phenomena in Thin Films: Metastable Alloy Phases*. in Use of Thin Film in Physical Investigation, (pp. 433–445). (Cited on pages 24 and 56).

[57] Mader S and Nowick A (1965) *Metastable Co–Au alloys: example of an amorphous ferromagnet*. Applied Physics Letters, **vol. 7, no. 3**:pp. 57–59. (Cited on pages 25 and 56).

[58] Vegard L (1921) *Die konstitution der mischkristalle und die raumfüllung der atome*. Zeitschrift für Physik A Hadrons and Nuclei, **vol. 5, no. 1**:pp. 17–26. (Cited on page 25).

[59] Bosco E, Rizzi P and Baricco M (2003) *Rapid Solidification of immiscible alloys*. Journal of Magnetism and Magnetic Materials, **vol. 262**:pp. 64–68. (Cited on page 25).

[60] Lu Dl, Domen K and Tanaka K (2002) *Electrodeposited Au-Fe, Au-Ni, and Au-Co alloy nanoparticles from aqueous electrolytes*. Langmuir, **vol. 18, no. 8**:pp. 3226–3232. (Cited on page 27).

[61] Swiatkowska-Warkocka Z, Koga K, Kawaguchi K *et al.* (2013) *Pulsed laser irradiation of colloidal nanoparticles: a new synthesis route for the production of non-equilibrium bimetallic alloy submicrometer spheres*. RSC Advances, **vol. 3, no. 1**:pp. 79–83. (Cited on page 27).

[62] Llamosa Perez D, Espinosa A, Martinez L *et al.* (2013) *Thermal diffusion at nanoscale: from CoAu alloy nanoparticles to CoAu coreshell structures.* The Journal of Physical Chemistry C, **vol. 117, no. 6**:pp. 3101–3108. (Cited on page 27).

[63] Nabika H, Mizuhata M, Kajinami A *et al.* (2003) *Preparation and Characterization of AuCo nano-alloys.* Journal of Electranalytical Chemistry, **vol. 559**:pp. 99–102. (Cited on page 27).

[64] Davey WP (1925) *Precision measurements of the lattice constants of twelve common metals.* Physical Review, **vol. 25, no. 6**:p. 753. (Cited on pages 34, 90, and 91).

[65] Hull AW (1921) *X-ray crystal analysis of thirteen common metals.* Physical Review, **vol. 17, no. 5**:p. 571. (Cited on page 34).

[66] Cullity B (1978) *Element of X-ray diffraction, Addition–Wesley.* Reading, MA. (Cited on page 37).

[67] Biersack J and Eckstein W (1984) *Sputtering studies with the Monte Carlo program TRIM. SP.* Applied Physics A, **vol. 34, no. 2**:pp. 73–94. (Cited on page 40).

[68] Rehr JJ, Kas JJ, Prange MP *et al.* (2009) *Ab initio theory and calculations of X-ray spectra.* Comptes Rendus Physique, **vol. 10, no. 6**:pp. 548–559. (Cited on page 49).

[69] Magnan H, Chandesris D, Rossi G *et al.* (1989) *Determination of the local order in amorphous cobalt films.* Phys. Rev. B, **vol. 40**:pp. 9989–9992. (Cited on page 50).

[70] Boscherini F, De Panfilis S and Weissmüller J (1998) *Determination of local structure in nanophase palladium by x-ray-absorption spectroscopy.* Physical Review B, **vol. 57, no. 6**:p. 3365. (Cited on page 50).

[71] Frenkel A, Machavariani VS, Rubshtein A *et al.* (2000) *Local structure of disordered Au-Cu and Au-Ag alloys.* Physical Review B, **vol. 62, no. 14**:p. 9364. (Cited on page 52).

[72] Maurizio C, Mattei G, Mazzoldi P *et al.* (2003) *Deviation from the virtual crystal approximation in disordered Au–Cu alloy nanocrystals: EXAFS and GIXRD investigation.* Nuclear Instruments and Methods in Physics Research Section B: Beam Interactions with Materials and Atoms, **vol. 200**:pp. 178–184. (Cited on page 52).

[73] Antonowicz J, Pietnoczka A, Zalewski W *et al.* (2011) *Local atomic structure of Zr–Cu and Zr–Cu–Al amorphous alloys investigated by {EXAFS} method.* Journal of Alloys and Compounds, **vol. 509, Supplement 1, no. 0**:pp. S34 – S37. {XVII} International Symposium on Metastable, Amorphous and Nanostructured Materials. (Cited on page 52).

[74] Wilhelm F, Angelakeris M, Jaouen N *et al.* (2004) *Magnetic moment of Au at AuCo interfaces: A direct experimental determination.* Phys. Rev. B, **vol. 69**:p. 220404. (Cited on pages 53, 75, and 76).

[75] Frenkel AI (2012) *Applications of extended X-ray absorption fine-structure spectroscopy to studies of bimetallic nanoparticle catalysts.* Chemical Society Reviews, **vol. 41, no. 24**:pp. 8163–8178. (Cited on page 54).

[76] Sprouster D, Giulian R, Araujo L *et al.* (2010) *Ion-irradiation-induced amorphization of cobalt nanoparticles.* Physical Review B, **vol. 81, no. 15**:p. 155414. (Cited on page 54).

[77] Jones RC (1942) *A New Calculus for the Treatment of Optical Systems. IV..* Josa, **vol. 32, no. 8**:pp. 486–493. (Cited on page 66).

[78] Aspnes DE (1982) *Optical properties of thin films.* Thin solid films, **vol. 89, no. 3**:pp. 249–262. (Cited on page 66).

[79] Carra P, Thole B, Altarelli M *et al.* (1993) *X-ray circular dichroism and local magnetic fields.* Physical Review Letters, **vol. 70, no. 5**:p. 694. (Cited on page 71).

[80] Bartolomé J, García L, Bartolomé F *et al.* (2008) *Magnetic polarization of noble metals by Co nanoparticles in M-capped granular multilayers (M= Cu, Ag, and Au): An x-ray magnetic circular dichroism study.* Physical Review B, **vol. 77, no. 18**:p. 184420. (Cited on pages 75, 76, and 77).

[81] Rogalev A, Wilhelm F, Jaouen N *et al.*, *X-ray magnetic circular dichroism: Historical perspective and recent highlights.* In *Magnetism: A Synchrotron Radiation Approach*, (pp. 71–93) (Springer, 2006). (Cited on page 75).

[82] Gambardella P, Rusponi S, Veronese M *et al.* (2003) *Giant magnetic anisotropy of single cobalt atoms and nanoparticles.* Science, **vol. 300, no. 5622**:pp. 1130–1133. (Cited on page 76).

[83] Haubold T, Birringer R, Lengeler B *et al.* (1989) *EXAFS studies of nanocrystalline materials exhibiting a new solid state structure with randomly arranged atoms.* Physics Letters A, **vol. 135, no. 8-9**:pp. 461–466. (Cited on page 80).

[84] Herr U, Jing J, Birringer R *et al.* (1987) *Investigation of nanocrystalline iron materials by Mössbauer spectroscopy.* Applied physics letters, **vol. 50, no. 8**:pp. 472–474. (Cited on page 80).

[85] Wagner W, Wiedenmann A, Petry W *et al.* (1991) *Magnetic microstructure of nanostructured Fe, studied by small angle neutron scattering.* Journal of materials research, **vol. 6, no. 11**:pp. 2305–2311. (Cited on page 80).

[86] McHenry ME, Willard MA and Laughlin DE (1999) *Amorphous and nanocrystalline materials for applications as soft magnets*. Progress in Materials Science, **vol. 44, no. 4**:pp. 291–433. (Cited on page 80).

[87] TRONC E (1997) *Magnetic relaxation in fine-particle systems*. Advances in, (p. 283). (Cited on page 83).

[88] Del Bianco L, Fiorani D, Testa A *et al.* (2002) *Magnetothermal behavior of a nanoscale Fe/Fe oxide granular system*. Physical Review B, **vol. 66, no. 17**:p. 174418. (Cited on page 83).

[89] Cullity BD and Graham CD, *Introduction to magnetic materials* (John Wiley & Sons, 2011). (Cited on page 84).

[90] Nogués J, Sort J, Langlais V *et al.* (2005) *Exchange bias in nanostructures*. Physics Reports, **vol. 422, no. 3**:pp. 65–117. (Cited on page 84).

[91] Fullerton EE, Jiang J and Bader S (1999) *Hard/soft magnetic heterostructures: model exchange-spring magnets*. Journal of Magnetism and Magnetic Materials, **vol. 200, no. 1**:pp. 392–404. (Cited on page 84).

[92] Spizzo F, Bonfiglioli E, Tamisari M *et al.* (2015) *Magnetic exchange coupling in IrMn/NiFe nanostructures: From the continuous film to dot arrays*. Physical Review B, **vol. 91, no. 6**:p. 064410. (Cited on page 84).

[93] Haynes CL and Van Duyne RP (2001) *Nanosphere lithography: a versatile nanofabrication tool for studies of size-dependent nanoparticle optics*. The Journal of Physical Chemistry B, **vol. 105, no. 24**:pp. 5599–5611. (Cited on page 97).

[94] Rybczynski J, Ebels U and Giersig M (2003) *Large-scale, 2D arrays of magnetic nanoparticles*. Colloids and Surfaces A: Physicochemical and Engineering Aspects, **vol. 219, no. 1**:pp. 1–6. (Cited on page 97).

[95] Ebbesen TW, Lezec HJ, Ghaemi H *et al.* (1998) *Extraordinary optical transmission through sub-wavelength hole arrays*. Nature, **vol. 391, no. 6668**:pp. 667–669. (Cited on page 99).

[96] Genet C and Ebbesen T (2007) *Light in tiny holes*. Nature, **vol. 445, no. 7123**:pp. 39–46. (Cited on pages 99 and 102).

[97] Popov E, Bonod N, Nevière M *et al.* (2005) *Surface plasmon excitation on a single subwavelength hole in a metallic sheet*. Applied optics, **vol. 44, no. 12**:pp. 2332–2337. (Cited on page 100).

[98] Degiron A and Ebbesen T (2004) *Analysis of the transmission process through single apertures surrounded by periodic corrugations*. Optics express, **vol. 12, no. 16**:pp. 3694–3700. (Cited on page 100).

[99] Jeon S, Lee JH, Jeong JH *et al.* (2015) *Vacuum Nanohole Array Embedded Phosphorescent Organic Light Emitting Diodes*. Scientific reports, **vol. 5**. (Cited on page 100).

[100] Luo X and Ishihara T (2004) *Subwavelength photolithography based on surface-plasmon polariton resonance*. Optics Express, **vol. 12, no. 14**:pp. 3055–3065. (Cited on page 100).

[101] Escobedo C (2013) *On-chip nanohole array based sensing: a review*. Lab on a Chip, **vol. 13, no. 13**:pp. 2445–2463. (Cited on page 100).

[102] Brolo AG, Arctander E, Gordon R *et al.* (2004) *Nanohole-enhanced Raman scattering*. Nano Letters, **vol. 4, no. 10**:pp. 2015–2018. (Cited on page 100).

[103] Moreno E, Fernández-Domínguez A, Cirac JI *et al.* (2005) *Resonant transmission of cold atoms through subwavelength apertures*. Physical review letters, **vol. 95, no. 17**:p. 170406. (Cited on page 100).

[104] Thio T, Ghaemi H, Lezec H *et al.* (1999) *Surface-plasmon-enhanced transmission through hole arrays in Cr films*. JOSA B, **vol. 16, no. 10**:pp. 1743–1748. (Cited on page 105).

[105] Genet C, van Exter MP and Woerdman J (2003) *Fano-type interpretation of red shifts and red tails in hole array transmission spectra*. Optics Communications, **vol. 225, no. 4**:pp. 331–336. (Cited on page 105).

[106] Lee SH, Bantz KC, Lindquist NC *et al.* (2009) *Self-assembled plasmonic nanohole arrays*. Langmuir, **vol. 25, no. 23**:pp. 13685–13693. (Cited on page 106).

Ringraziamenti

Ringrazio, innanzitutto, il Prof. Giovanni Mattei per avermi accolta nel gruppo di ricerca ed essere sempre stato punto di riferimento competente e disponibile in questi anni di dottorato.

Grazie alla Dr. Chiara Maurizio per le preziosissime discussioni scientifiche...e non...e per l'insostituibile supporto nell'analisi EXAFS.

Vorrei ringraziare la Dr. Valentina Bello per le misure TEM e la Dr. Valentina Russo per la 'fornitura' di maschere per NSL: ma le ringrazio soprattutto per la condivisione amichevole di questi anni di attività di ricerca.

Grazie a Dr. Tiziana Cesca, Dr. Niccolò Michieli e Dr. Boris Kalinic per le consulenze nelle varie attività di laboratorio.

Ringrazio l'Ing. Carlo Scian e Luca Bacci per il supporto nelle questioni più prettamente tecniche.

Un grazie 'corale' a tutti i laurendi e dottorandi, passati e attuali, dell' *NSG group*.

Un ringraziamento speciale al Prof. Carlo Battaglin, per la disponibilità sempre dimostrata nelle misure RBS.

Grazie di cuore alla Prof.ssa Lucia Del Bianco, al Dr. Federico Spizzo e Federico Chinni perchè, con le caratterizzazioni magnetiche, hanno contribuito a raccogliere e interpretare dati prezioni per questa tesi.

Many thanks to Devaraju, for the friendship and fruitful discussions about Italian vs. Indian culture.

Infine, ma non da ultimo, un grazie speciale a Riccardo, Samuele e Sara Maria per avermi supportato e...sopportato!